UNIVERSITY OF LIÈGE
FACULTY OF SCIENCES
DEPARTMENT OF ASTROPHYSICS, GEOPHYSICS, AND OCEANOGRAPHY
(AGO)

Development and exploitation of an infrared coronagraphic test bench for vortex phase mask performance assessment

Author:
Aïssa JOLIVET

Supervisors
Dr. Olivier ABSIL
Prof. Serge HABRAKEN

A thesis submitted in fulfillment of the requirements
for the degree of Doctor of Philosophy in Space Sciences
in the
Department of Astrophysics, Geophysics, and Oceanography (AGO)

August 9, 2019

Members of the jury:

Prof. Denis GRODENT, University of Liège (President)

Dr. Olivier ABSIL, University of Liège (Advisor)
Prof. Serge HABRAKEN, University of Liège (Co-Advisor)

Prof. Mikael KARLSSON, Uppsala Universitet
Prof. Lucas LABADIE, Universität zu Köln
Prof. Dimitri MAWET, California Institute of Technology
Dr. Gilles ORBAN DE XIVRY, University of Liège
Prof. Jean SURDEJ, University of Liège

THESIS ABSTRACT

Coronagraphy is a high-contrast imaging technique aiming to reduce the blinding glare of a star in order to detect a potential companion in its close environment. Vortex phase mask coronagraphy is widely recognized as one of the most promising approaches.

This thesis is dedicated to the performance assessment of the vortex coronagraph. For this purpose, it was crucial to have our own dedicated facility at the University of Liège. In the first part of this thesis we describe how was built the Vortex Optical Demonstrator for Coronagraphic Applications (VODCA) to optically characterize infrared phase masks, in particular vortex masks. The layout and salient features of VODCA are presented, as well as its operations, and its limitations in terms of optical quality. The bench is then used to assess the performance of L- (3575-4125 nm) and M-band (4600 to 5000 nm) annular groove phase masks (AGPM) manufactured by our team. We discuss the results obtained with other facilities and put them in perspective with the new measurements on VODCA. We demonstrate the highest rejection ratio ever measured for an AGPM at L-band: 3.2×10^3 in a narrow band filter (3425-3525 nm) and 2.4×10^3 in a broad L band filter. We also describe the first results obtained at shorter wavelengths (H- and K-bands, from 1500 to 2400 nm). Vortex phase masks with higher topological charges VVC (Vector Vortex Coronagraph) are theoretically more resilient to aberrations and resolved stars, a key feature for next generation coronagraphs. We present here various designs for the SGVC4 (charge 4 Subwavelength Grating Vortex Coronagraph) and the performance of the first manufactured components. We finally investigate the influence of optical aberrations on the AGPM and SGVC4, and confirm the simulations results. The AGPM is sensitive to low order aberrations while the SGVC4 is significantly less affected by tip/tilt and defocus.

By providing measurements close to the intrinsic limit of science-grade AGPMs and accurately describing their behavior, VODCA proves to be a step forward in terms of the evaluation of vortex phase masks performance.

Keywords : Infrared test bench, high contrast imaging, subwavelength grating vortex coronagraph.

RÉSUMÉ

La coronographie est une technique d'imagerie « haut-contraste » dont le but est de réduire la lumière d'une étoile pour permettre la détection de potentiels compagnons dans son environnement proche. L'utilisation de masques de phase vortex est une des approches les plus prometteuses dans le développement de nouveaux coronographes.

Cette thèse est consacrée à l'évaluation des performances de ces coronographes. Pour cela, il s'est avéré indispensable d'avoir notre propre structure de test au sein de l'Université de Liège. Dans la première partie de ce document, nous décrivons le développement et la mise en place du Vortex Optical Demonstrator for Coronagraphic Applications (VODCA) pour la caractérisation de masques de phase dans l'infrarouge et en particulier les masques vortex. Le montage optique et les principales caractéristiques de VODCA sont présentés ici ainsi que le détail de son opération et ses limites en termes de qualité optique. Le banc est ensuite utilisé pour évaluer précisément les performances de nos « annular groove phase masks » (AGPM) en bande L (3575-4125 nm) et M (4600-5000 nm). Nous mettons ensuite en perspective ces résultats avec ceux obtenus sur d'autres bancs optiques. Nous atteignons ainsi les plus haut taux de rejection jamais mesuré pour un AGPM en bande L : 3.2×10^3 avec un filtre en bande étroite (3425-3525 nm) et 2.4×10^3 en bande large. Nous détaillons également les premiers résultats obtenus à de plus courtes longueurs d'onde (bandes H et K, de 1500 à 2400 nm). Les masques de phases vortex avec une charge topologique plus élevée sont théoriquement plus robustes aux aberrations et aux étoiles résolues par le télescope, un élément clé pour la prochaine génération de coronographes. Nous présentons ici différents designs pour un masque de phase vortex de charge 4 et les performances des premiers composants fabriqués. Finalement, nous nous intéressons à l'influence des aberrations optiques sur l'AGPM et les masques vortex de charge 4 et sommes en mesure de confirmer les simulations. L'AGPM est sensible aux aberrations de bas-ordre tandis que le masque vortex de charge 4 est lui considérablement moins affecté par le tip/tilt ainsi que le défocus.

En étant capable de délivrer des mesures proche de la limite intrinsèque de nos meilleurs AGPMs et de décrire avec précision leur comportement optique, VODCA se révèle être une importante amélioration en termes d'évaluation des performances de masques de phases vortex.

Mots-clés : Banc de test infrarouge, imagerie haut contraste, coronographe vortex.

CONTENTS

List of Figures

List of Tables

List of Abbreviations

ADI	Angular Differential Imaging
AGPM	Annular Groove Phase Mask
ALPC	Apodized Lyot Pupil Coronagraph
AO	Adaptive Optics
APCMLC	Apodized Pupil Complex Mask Lyot Coronagraph
APP	Apodized Phase Plate
ARG	Anti-Reflective Grating
BBF	Broad Band Filter
CPA	Conventional Pupil Apodization
DM	Deformable Mirror
ERIS	Enhanced Resolution Imager and Spectrograph
ESO	European Southern Observatory
FQPM	Four Quadrant Phase Mask
FWHM	Full width at Half Maximum
HWP	Half-Wave Plate
IRCT	InfraRed Coronagraphic Testbed
IWA	Inner Working Angle
JPL	Jet Propulsion Laboratory
LCP	Liquid Cristal Polymer
MIR	Mid-InfraRed
NASA	National Aeronautics and Space Administration
NBF	Narrow Band Filter
NCPA	Non Common Path Aberrations
ND	Null Depth
NIR	Near-InfraRed
OAP	Off-Axis Parabola
PCP	Photonic Cristal Polymer
PCA	Principal Component Analysis
PDMS	PolyDiMethylSiloxane
PIAAC	Phase-Induced Amplitude Apodization Coronagraph
PIAACMC	Phase Induced Amplitude Apodization Complex Mask Coronagraph
PIAALC	Phase-Induced Amplitude Apodization Lyot Coronagraph
PSF	Point Spread Function
QACITS	Quadrant Analysis of Coronagraphic Images for Tip-Tilt Sensing
QCL	Quantum Cascade Laser
RCWA	Rigorous Coupled-Waved Analysis
RMS	Root Mean Square
RR	Rejection Ratio
SC	Super-Continuum

SDI	Spectral Differential Imaging
SG	Subwavelength Grating
SGVC	Subwavelength Grating Vortex Coronagraph
SGVC2	Charge 2 Subwavelength Grating Vortex Coronagraph
SGVC4	Charge 4 Subwavelength Grating Vortex Coronagraph
SNR	Signal to Noise Ratio
Speculoos	Search for habitable Planets EClipsing ULtra-cOOl Stars
Trappist	TRAnsiting Planets and PlanetesImals Small Telescope
VIP	Vortex Image Processing
VLT	Very Large Telescope
VODCA	Vortex Optical Demonstrator for Coronagraphic Applications
VVC	Vector Vortex Coronagraph
WFS	WaveFront Sensor
ZWFS	Zernike WaveFront Sensor

LIST OF SYMBOLS

Symbol	Description	Unit
λ	Wavelength	nm
h	Grating's depth	μm
Λ	Grating's period	μm
F	Filling factor	
α	Sidewall angle	$^\circ$

Notations

Atmospheric windows

H band	from 1.44 to 1.78 μm
K band	from 1.95 to 2.35 μm
L band	from 3.5 to 4.1 μm
M band	from 4.6 to 5 μm
N band	from 11 to 13.2 μm

PART I

Introduction

1 IMAGING EXOPLANETS

1.1 The search for exoplanets

By definition, an exoplanet is a planet beyond our solar system. Their existence was hypothesized by the scientific community a long time ago but was only verified recently. The first confirmed detection occurred in 1992 when a planetary system was discovered around a pulsar (Wolszczan and Frail, 1992). A few years later, the first exoplanet around a main-sequence star was detected (Mayor and Queloz, 1995).

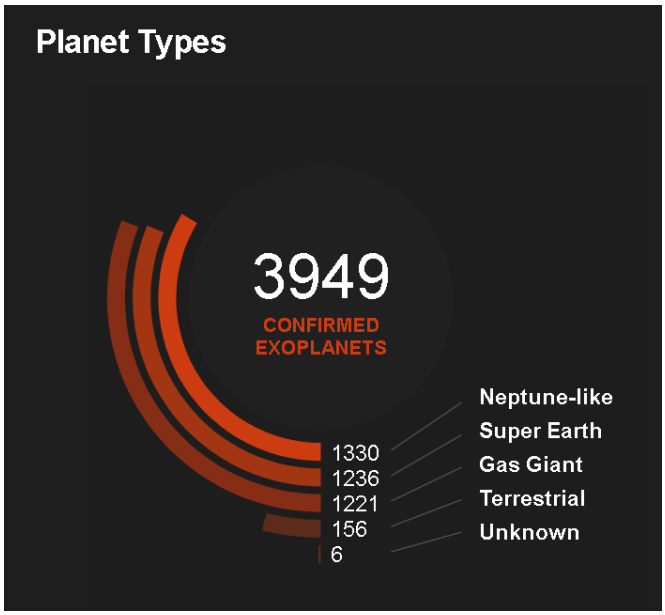

Figure 1.1: Confirmed exoplanets detection and the planet type distribution. Credits: NASA

Until the 90's, only a reduced sample limited to the 8 planets of the Solar system was available to create and fine-tune models on the formation of planetary systems. Today, more than 3900 detections have been confirmed (Figure 1.2). Recent studies reached the conclusion that planetary systems orbiting a star is the common rule

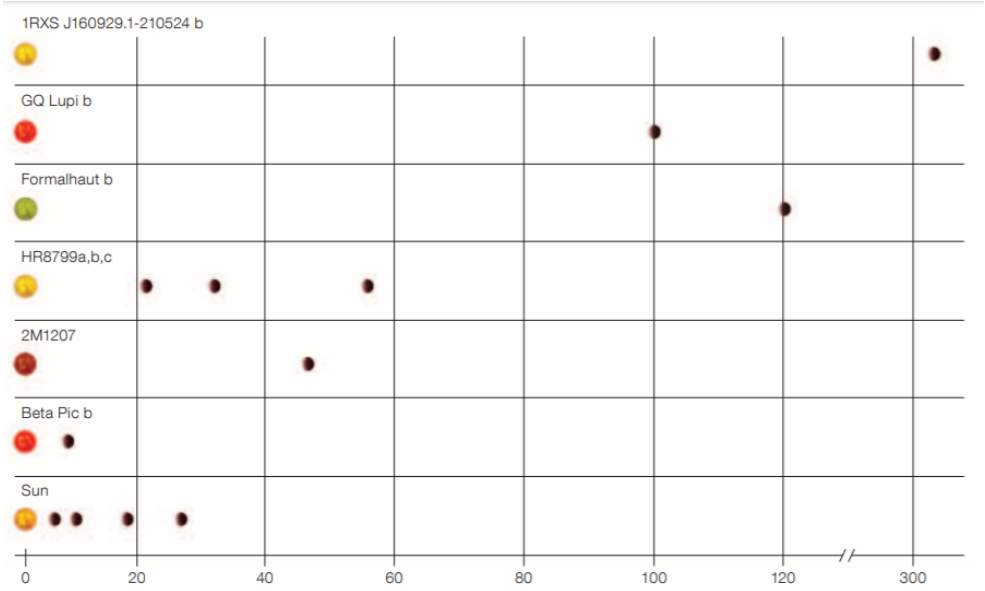

Figure 1.2: This diagram compares our Solar System with some of the planetary systems imaged so far, with the exoplanet distance relative to its host star expressed in astronomical units. The Solar System is illustrated at the bottom, showing the Sun along with the four outer planets, Jupiter, Saturn, Uranus and Neptune. Credits: ESO Press Release.

with an Earth-like planet frequency estimated around 20% (Petigura et al., 2013). Most of the exoplanets discovered belong to the Neptune-like and Jupiter-like categories although Earth-like planets could be the most abundant. These detections have tremendously improved our understanding of planetary systems (Figure 1.2) and added new classes of planets such as hot-Jupiters (giant gaseous planets with small orbits) or super-Earths, more massive than the Earth but smaller than Neptune (Valencia et al., 2007).

Exoplanet observation provides extremely valuable information about the process of planet formation and aim to answer one of the greatest questions of mankind: does life exist elsewhere in the Universe ?

The search for life has been shaped by the conditions which allowed its emergence on Earth, mainly the presence of liquid water. This temperature condition is related to the radiant energy received by an exoplanet from its host star and as a consequence the distance between them. This range of distance allowing liquid water is called the habitable zone (see Figure 1.3). Even if it has been challenged as the only criterion for life emergence, the presence of liquid water outside the habitable zone has been accepted (Jupiter and Saturn's moons for example, Sohl et al. (2010) and Hussmann et al. (2010)). Nevertheless, observations still focus on exoplanets in the habitable zone to detect life (Kopparapu et al., 2013). The closest exoplanet (Proxima Centauri b) being at more than 4 light years from Earth, a space mission to other solar systems is not a viable solution in the close future. However, it is possible to detect the presence of life on an exoplanet from ground-based (or space-borne) observations. An exoplanet hosting life will see its atmosphere composition altered in

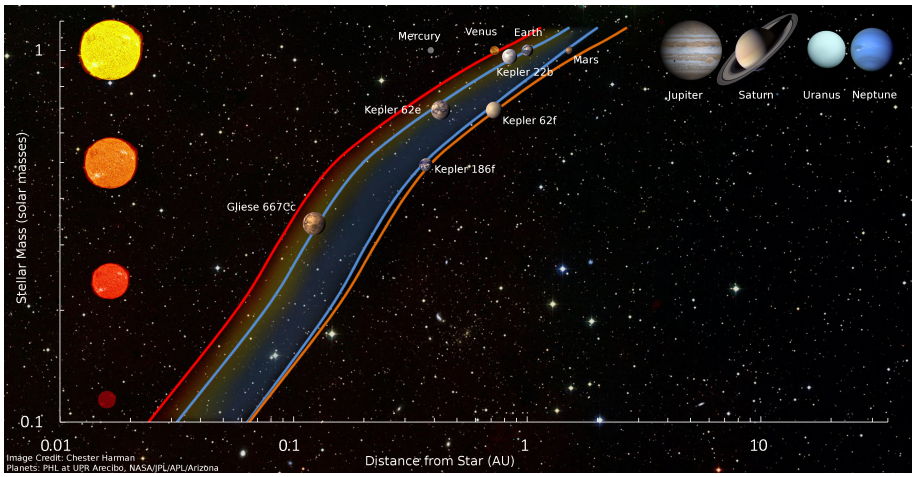

Figure 1.3: Spatial representation of the habitable zone, main area of interest for life detection. The red lines define an optimistic definition of the habitable zone while the blue lines are more conservative.

a way that is not attainable without life. The characteristic markers are called biosignatures: they can be detected by a spectral analysis of the exoplanet atmosphere (Schwieterman et al., 2018).

Remarkable technological and technical progress in the recent years and the new class of extremely large telescopes under construction promise even more discoveries in the future and game-changing breakthroughs.

1.2 Detection methods

Different methods of detection can be used in the hunt for exoplanets and are divided in two main categories: direct and indirect methods. Technological limits and intrinsic preferential targets inherent to each method may create a bias in the pool of discoveries leading to an over representation of Neptune-like and gas giant planets (Kipping and Sandford, 2016).

1.2.1 Indirect methods

Indirect methods constitute a class of exoplanet detection techniques focusing on observing the star to infer the presence of companions. They were the first ones to be developed and represent most of the confirmed detections (>95%, Figure 1.4). The main indirect methods, radial velocity and transit, are briefly described below.

Transit

More than 77% of the exoplanet confirmed detections have been made through transit observations (Figure 1.5). A transit occurs when an exoplanet passes between the star it orbits and the observer. The brightness of the star decreases as the exoplanet blocks part of the starlight. By repeatedly measuring the small flux attenuation, the orbital parameters and radius of the exoplanet can be deduced. Since starlight goes through the planet's atmosphere, in some cases it has been possible to identify its

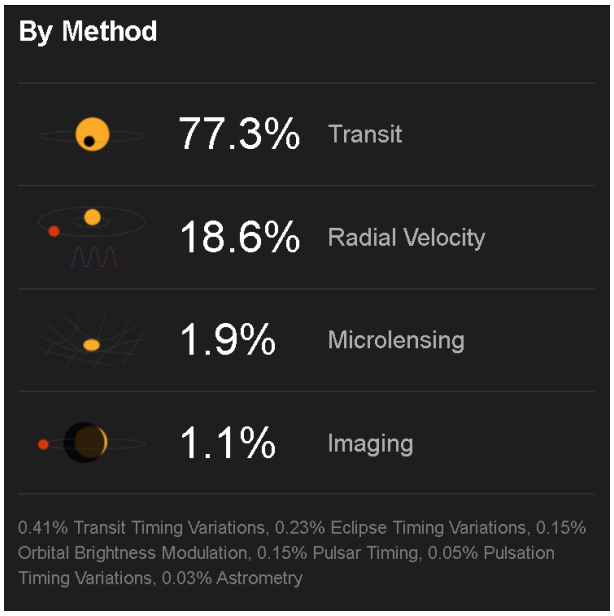

Figure 1.4: Distribution of the main exoplanet detection methods. Credits: NASA.

chemical composition (Deming and Seager (2017), Winn (2010), Sing et al. (2009)). "Hot Jupiters" (massive planets close to the host stars) are the most likely to be observed; their big size creates deeper transits. Red dwarf stars are the preferred candidates for the observations of rocky planets since their small radius increases the depth of the transit. Some of the most successful projects (TRAPPIST, SPECULOOS, The SPECULOOS and TRAPPIST teams et al. (2018)) have been focused on this type of stars. Obviously, only a small portion of all exoplanets can be observed by this method since it requires a specific orientation of the star-planet system to produce transits visible from Earth. Star brightness fluctuations and insufficient photometry accuracy (especially in the case of small exoplanets and bright stars) can also prevent effective transit detections.

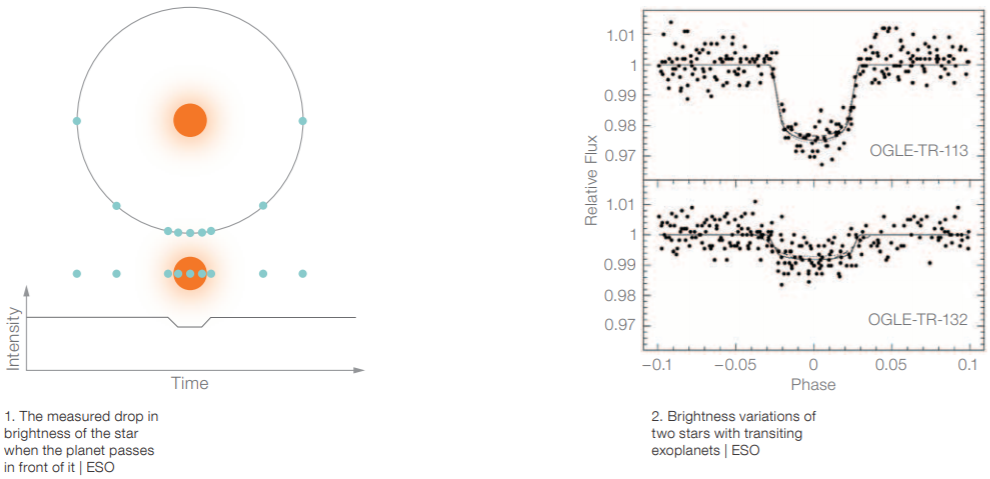

Figure 1.5: The transit method. Credits: ESO Press Release.

Radial Velocity

Radial velocity (Figure 1.6) was until the 2010s the main technique for exoplanet detection. It accounts now for 18.6% of the discoveries. An orbiting exoplanet creates a gravitational pull on the star. As a result, the star will move on a small orbit around the center of gravity of the system and this movement can be quantified by observing the star's spectrum. The Doppler effect predicts a blue- or red-shift of its spectrum when the star moves toward or away from the observer. An estimation on the exoplanet (or companion) mass can also be determined from the spectral shift. The major limitation is that the spectrum shift can only be measured on the star-observer axis. If the orbital plane of the exoplanet is not aligned along this axis, the radial velocity can not capture the complete motion of the star. Only a minimal mass of the planet can be calculated without further observations. This method favors the detection of "hot-Jupiters". Their big mass creates the largest change in radial velocity and the small orbit allows more observations (increased Signal to Noise Ratio). Complex planetary systems (several planets with different masses and various orbit radii) and stellar activity can make the observations less conclusive (Vanderburg et al., 2016).

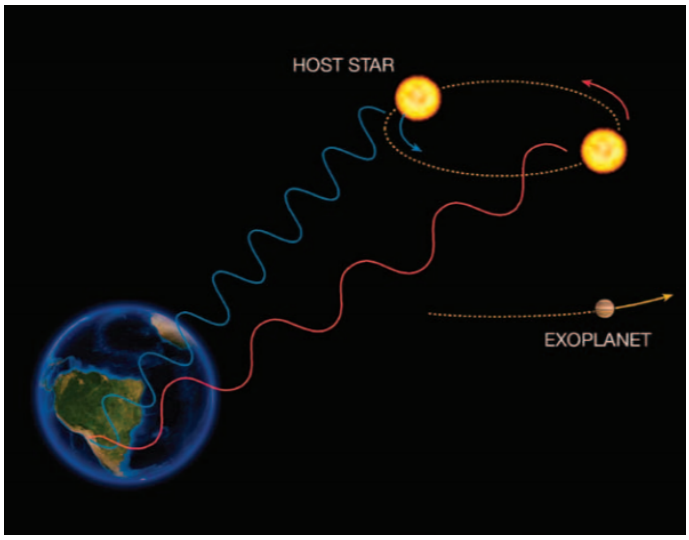

Figure 1.6: The radial velocity method. Credits: ESO Press Release.

1.2.2 Direct methods

As opposed to indirect methods, direct observations collect the light from the exoplanet itself. Direct imaging is a great tool not only for the detection but also for the spectral characterization of exoplanets. Having access to a planet's flux allows (depending on the accuracy) to identify its structure, the composition of its atmosphere and possibly to identify markers of life. It also gives access to an important pool of planetary systems that could not be observed through the previously described indirect methods.

Unfortunately, these methods face two major issues. (i) The angular separation between a distant star and an orbiting exoplanet is really small (few milliarcsec to a few arcsec). (ii) An exoplanet is much fainter than its host star, disregarding whether

its thermal or reflected light is considered. For instance, an Earth-like planet presents a contrast of 10^{-10} with respect to a Sun-like star in the visible (reflected light) or around 10^{-7} in the mid-infrared (thermal emission). The angular resolution of an instrument, i.e. the smallest angle between two objects that the instrument can separate, is a crucial feature of a telescope. A better resolution allows to detect exoplanets closer to their host star. A star and an exoplanet can be considered as point sources in most cases (future 30+m class telescopes will challenge this assertion). In the abscence of aberrations, their direct images are limited by diffraction and lead to the concept of the point spread function (PSF). In the case of an unobstructed circular aperture, this function is described by an Airy pattern. According to the definition, two equally bright point sources are resolved when the maximum of the first PSF is located farther than the first minimum of the second one. The Airy pattern first minimum is observed at an 1.22 λ/D angle, where λ is the wavelength and D the diameter of the circular aperture of the telescope.

Under perfect conditions, the resolving power of a telescope is positively affected by two factors: (i) observing at shorter wavelengths and (ii) increasing the aperture diameter, which also contributes to a better detection of faint objects since more photons are collected. In practice, the angular resolution of ground-based telescopes is strongly limited by atmospheric turbulence and also by the optics quality. The atmosphere, constantly moving with layers of air at different temperatures and densities, can not be considered as a uniform medium but consists of multiple refractive indexes evolving at high frequency due to the wind. The light from the star can be considered as a flat wavefront before going through the atmosphere. After that, the PSF which should be an Airy pattern becomes blurry. Bright, compact and moving spots appear around the PSF (speckles). As a consequence, potential companions buried in either the star widened PSF or in the speckles are less likely to be detected.

The Strehl ratio is the main criterion to assess the quality of a telescope and its instrument. It is defined as the ratio between a given PSF and the theoretical Airy pattern. A telescope strongly limited by atmospheric turbulence can only achieve a very low Strehl ratio. Typically, the best sites for observations have a coherence length (r_0) between 15 and 30 cm. r_0 is the greatest diameter of a circular aperture with less than 1 rad rms phase aberrations on its collected light wavefront. The "seeing" is estimated from the full width at half maximum (FWHM) of a long exposure PSF for a telescope with diameter $\oslash > r_0$. A telescope with a diameter larger than r_0 is not diffraction limited but "seeing-limited". Any aperture larger than r_0 will add no gain to the resolving power (except if it is being used with adaptive optics).

Adaptive Optics

Adaptive Optics (AO, Figure 1.7) is a technical solution used to compensate atmospheric turbulence and aberrations introduced by the optics when operating a telescope at its full potential (first applied for astronomy by Rousset et al. (1990)). AO is a two step process, the wavefront distortion is first measured with a wavefront sensor (WFS: Shack-Hartmann, pyramid, etc..). The information is then processed by a software and sent to a deformable mirror (DM) installed in the optical path. A DM is a mirror with actuators below its surface that can be pulled or pushed to modify its shape as necessary. The DM tunes its shape to compensate the wavefront aberrations. The WFS measures the wavefront corrected and in a close loop adapts the information sent to the DM for a live correction.

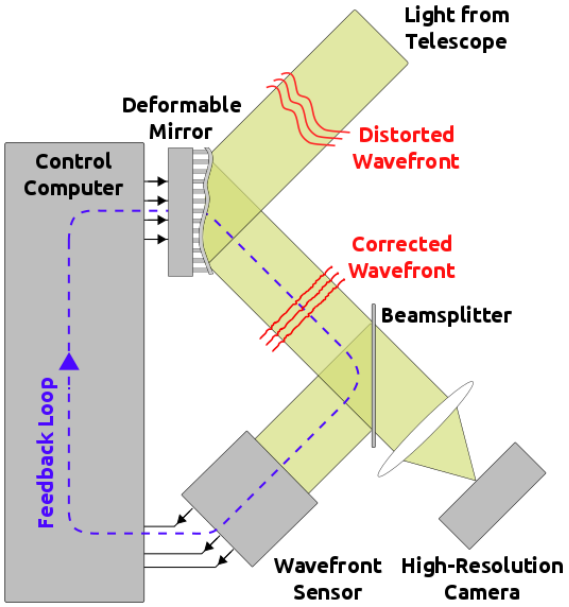

Figure 1.7: Representation of an adaptive optics layout. Credits: mavis-ao.org.

A larger number of DM actuators (and density) guarantees a finer level of aberration correction. State of the art DM for large ground-based telescopes have thousands of actuators. Concerning the frequency, the wavefront correction has to operate at the same or higher frequency than the typical atmospheric turbulence ($\approx$ 1 kHz). Lower frequency AO systems can be used to correct the quasi-static aberrations induced by misalignments and the optics. Nowadays, the best AO systems can use a couple of DMs and WFSs correcting first low order aberrations with a large amplitude and then higher orders with smaller amplitudes (which require finer correction). State of the art adaptive optics systems on 10m-class telescopes provide PSFs with Strehl ratios higher than 90% in the near-infrared (Dekany et al. (2013), Macintosh et al. (2014), Milli et al. (2017), Sahoo et al. (2018)).

Observing techniques

Angular Differential Imaging (ADI, Marois et al. (2006), Figure 1.8) can be used on an alt-azimuth telescope where the pupil rotates with respect to the field. The Earth rotation around its axis makes the field rotate for an observer on the ground. This technique takes advantage of the fact that quasi-static speckles (due to the telescope) are fixed during the observation. In this case, a reference image averaging the speckle can be subtracted from each image. The images are then "derotated" to maximize the flux of a potential companion. It allows to reduce the speckles noise (and partially the starlight) while in the meantime increasing the exoplanet signal.

Spectral Differential Imaging (SDI, Smith (1987), Racine et al. (1999), Lafreniere et al. (2007)) pursues the same goal but uses the difference between an exoplanet and the speckles when the wavelength of observation varies. Speckles are caused by the starlight diffraction and their position changes with respect to the wavelength, contrary to the exoplanet that has a fixed position. Taking into account this behavior, it is possible to strongly attenuate the speckle noise.

Various post-processing techniques consisting of data reduction and combining images aim to reduce the speckle noise and make potential companions more visible. In the Vortex project, we developed our own post-processing package (VIP, vortex image processing, Gomez Gonzalez et al. (2017)) using ADI and principal component analysis (PCA) algorithms.

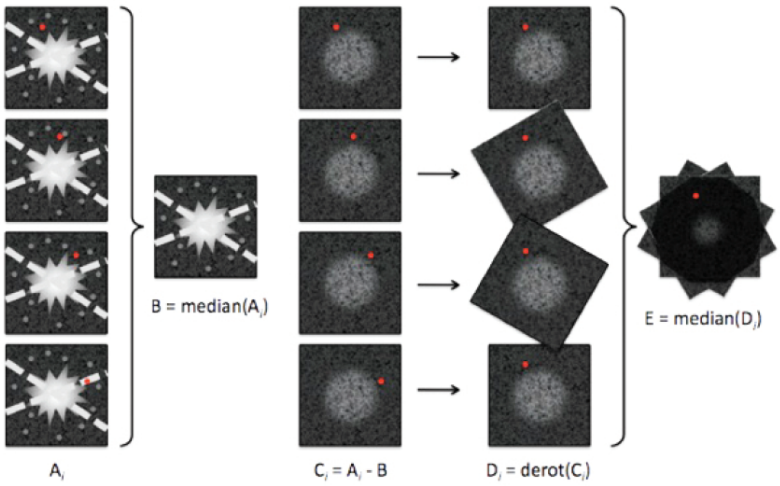

Figure 1.8: Illustration of the ADI image combination technique. A_i corresponds to the series of raw frames taken in pupil-stabilized observing mode. The halo sketched in gray is the quasi-static speckle, the red-highlighted point is the rotating planet signal. Credits: Christian Thalmann, Max Planck Institute for Astronomy.

1.3 Coronagraphy

Coronagraphy is a direct imaging technique aiming to mitigate the contrast issue between an exoplanet and its host star. In 1939, Bernard Lyot designed an optical instrument to observe the Sun's corona without being blinded by its photosphere (Lyot, 1939). The term "coronagraphy" describes systems relying on the principle of blocking the light from the star (on-axis source) to distinguish its surrounding (off-axis sources).

Applied to exoplanet detection, coronagraphy is a high-contrast imaging technique aiming to reduce the blinding glare of a star to enable the detection of very faint objects in its vicinity (Figure 1.9). The emergence of the exoplanet detection field led to remarkable innovations in the coronagraphic techniques. They can be divided in two distinct categories : (i) focal plane and (ii) pupil plane coronagraphs depending on where they use a Fourier spatial filter to produce the coronagraphic effect.

1.3.1 Focal plane coronagraphy

Focal plane coronagraphy relies on an amplitude or phase mask in the focal plane to achieve the starlight cancellation. The coronagraph mask is placed at the focal point and produces the coronagraphic effect that cancels the beam from the on-axis

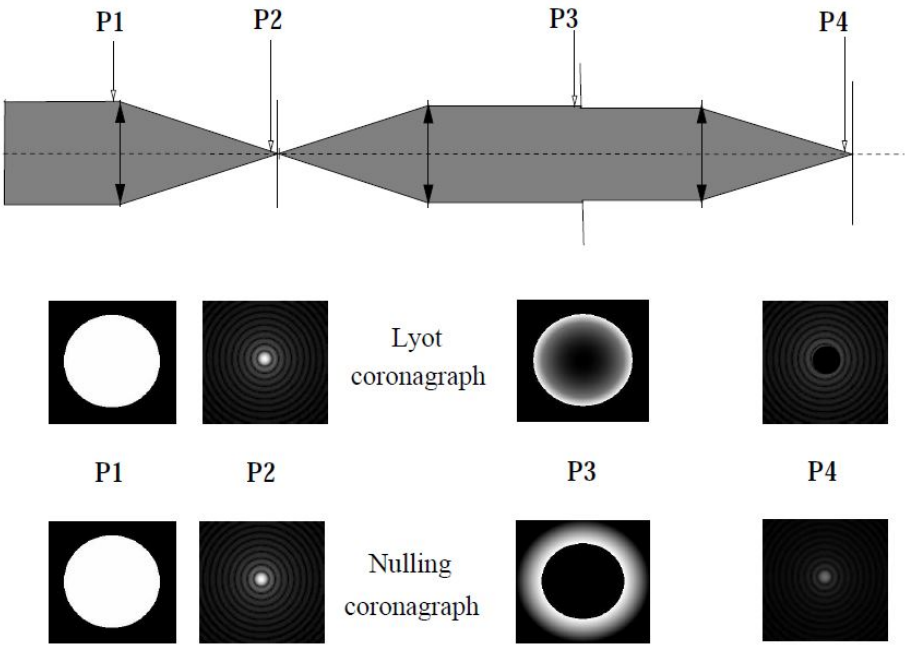

Figure 1.9: The Lyot coronagraph uses an opaque mask in the image plane, whereas the nulling coronagraph (now referred to as the 'Roddier coronagraph') uses a phase mask. Light distribution in the pupil is very different for the two coronagraphs. For the Lyot coronagraph the light is concentrated inside the pupil near the edge. For the phase mask it is moved outside the pupil. This figure shows the light distribution in four different planes for both coronagraphs. Plane P1 is the entrance pupil plane; plane P2 is the focal plane, where the occulting (or phase) mask is; plane P3 is the second pupil plane, where the "Lyot" stop is; and plane P4 is the second focal plane. Credits: Guyon et al. (1999).

source. By diffraction, the light is distributed (partially) outside the geometric pupil and blocked by an undersized (compared to the first aperture) diaphragm called the Lyot stop. When focused, an off-axis source PSF is slightly shifted compared to the on-axis focal plane mask. It is not affected by the mask and the flux propagates through the system. The star light vanishes and potential nearby companions can be observed. Focal plane coronagraphic masks are divided in two categories, they either use amplitude or phase to cancel the starlight.

Amplitude masks

An amplitude mask is an opaque disk placed at the focal point, it blocks physically the light of the core of the PSF. Its size has to be carefully chosen to only block the core of the stellar PSF. Since the PSF diameter varies with respect to the wavelength, amplitude masks are intrinsically chromatic. The drawback of amplitude masks is their large inner-working angle (IWA). The IWA describes the smallest angular separation between the host star and a detectable companion. This limit is set when the transmission reaches 50%. They also do not completely cancel the starlight. The two main reasons are (i) the diffraction around the mask edges and (ii) since the mask has a finite size, it only blocks the core of the PSF allowing the rest to propagate inside

the geometric pupil. Reducing the Lyot stop diameter improves the cancellation but at the price of a low throughput.

Phase masks

As opposed to amplitude masks, phase masks are transparent. They introduce a phase shift to the on-axis source and by destructive interference the light is rejected outside the geometric pupil. The first phase mask, described in Roddier and Roddier (1997) and now referred to as the Roddier coronagraph, consists in a transparent material with a circular step in the center. The step depth e is sized as $\lambda = 2(n-1)e$ and its diameter only covers a part of the PSF core. The principle is to introduce a π phase shift on a small area of the PSF that will destructively interfere with the rest of the PSF to produce the coronagraphic effect. The advantage of such a mask is the smaller IWA since the light is not physically blocked and only the on-axis source is affected. The starlight cancellation is improved and is perfect for a circular aperture and monochromatic source. The drawback is a strong chromaticism, both the diameter and the depth of the step are expressed as a function of λ. The chromatism of the mask can be reduced by using several steps producing different phase shifts (Soummer et al., 2003) at the price of technical difficulties.

To reduce the double chromatic dependance, the four quadrant phase mask was proposed (Rouan et al. (2000), Rouan et al. (2007), Riaud et al. (2001), Boccaletti et al. (2004), Figure 1.10). It consists of 2 quadrants inducing a π phase shift with respect to the other 2 to produce the coronagraphic effect. Only the depth of 2 quadrants depends on λ. However the weaknesses of the FQPM include a sensitivity to central obstruction and spider arms in addition to the loss of transmission at the edges between two quadrants.

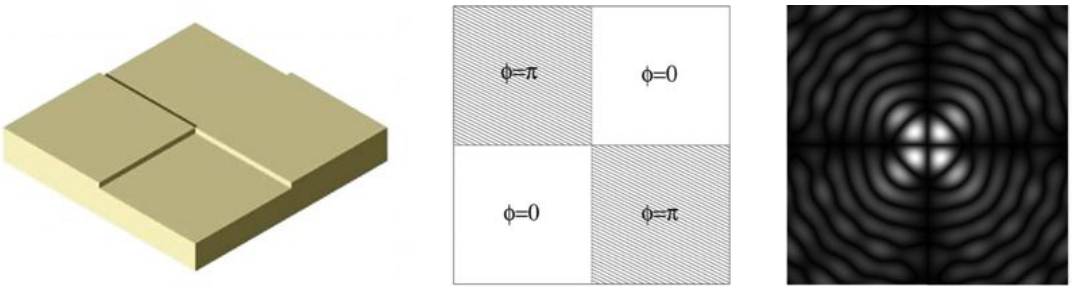

Figure 1.10: Left: Design of the four quadrant phase mask (FQPM). Middle: Two quadrants on one diagonal make the light undergo a π phase shift, whereas the two other quadrants let it pass without shifting the phase. Right: Resulting PSF with a logarithmic intensity scale normalized to the peak flux. In the perfect case (circular aperture, perfect phase shift), the stellar light is perfectly cancelled. From Rouan et al. (2007).

The ultimate step of phase masks evolution is the vortex phase mask coronagraph. Core element of this thesis, it will be extensively described in the next chapter.

1.3.2 Pupil plane coronagraphy

Pupil plane coronagraphy uses amplitude or phase apodizers as spatial filters in the entrance pupil to shape the image of the star downstream.

The apodization can be achieved by variations of amplitude in the entrance pupil. Various shapes can be applied depending on the telescope configurations (spider arms, central obstruction) and the observation goals. The price of their performance is a considerable diminution of the instrument throughput (Shaped Pupil Coronagraph, Kasdin et al. (2004)). An other method is the phase apodization of the pupil such as the apodized phase plate (APP, Codona and Angel (2004)). The diffraction mitigate the speckle in some specific zones of the pupil (dark zones) but reinforce them in other zones by symmetry. At maximum, a 180° dark zone can be created to facilitate the detection of faint companions. The main limitations of the APP are its detection zone and outer working angle.

1.3.3 Hybrid solutions

Coronagraphs such as the PIAACMC (phase induced amplitude apodization complex mask coronagraph, see Figure 1.11, Guyon et al. (2010)) combines both techniques and a specific phase mask to offer a complete attenuation of an on-axis source, excellent throughput (>99%) and small IWA (<$1\lambda/D$). The drawbacks of such a coronagraph are the increased complexity of the instrument layout and the technological challenge of the optics manufacturing.

Amplitude masks are commonly used with pupil plane coronagraphs (Shaped pupil Lyot, apodized pupil Lyot, PIAACMC, hybrid Lyot, Ruane et al. (2018)).

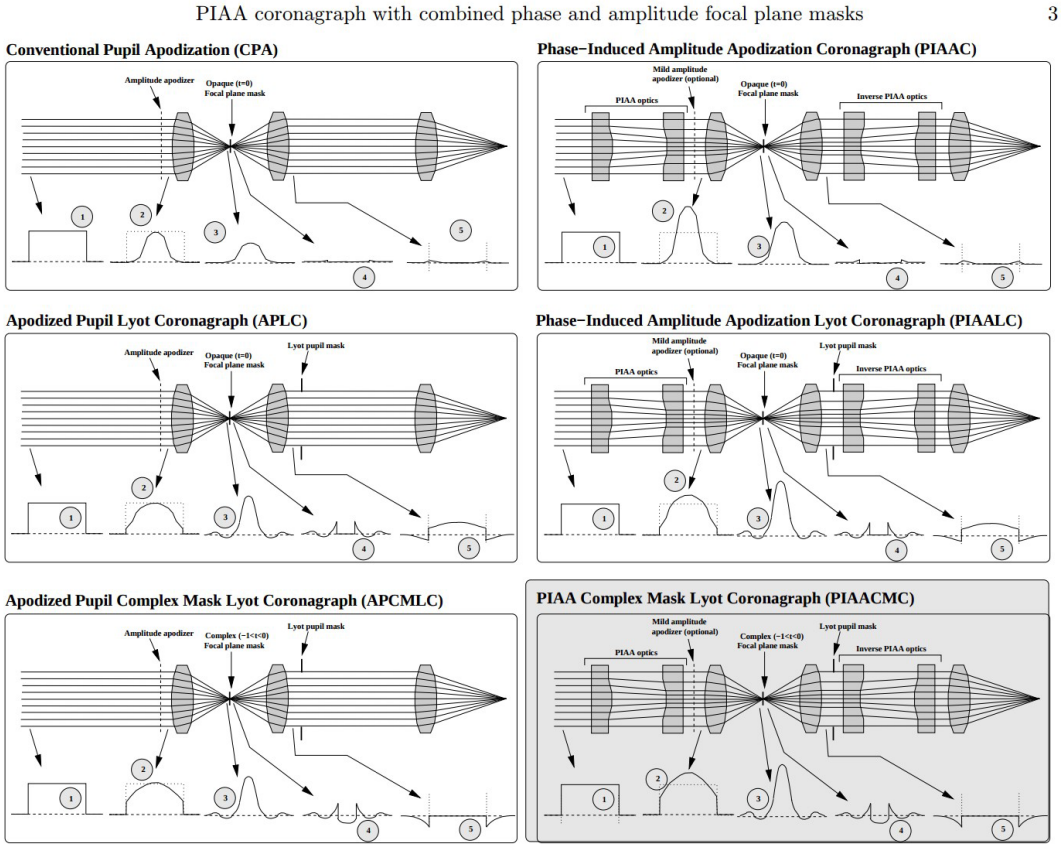

Figure 1.11: Coronagraphic architectures. In CPA (top left), the coronagraphic effect is obtained by the combination of a pupil plane apodizer and a focal plane mask. Performance is augmented in the Apodized Pupil Lyot Coronagraph (APLC) by introducing a Lyot mask in the output pupil plane (center left). Further performance improvement is achieved by replacing the opaque focal plane occulting mask with a partially transmissive phase-shifting mask (bottom left). The right part of this figure shows the equivalent coronagraph designs when apodization is performed by lossless PIAA optics instead of a classical apodizer. A graphical representation of complex amplitude in a few relevant planes is shown for each coronagraph: (1) telescope entrance pupil, (2) pupil after apodization, (3) focal plane before introduction of the focal plane mask, (4) focal plane after the focal plane mask, and (5) exit pupil plane before truncation by the Lyot mask. The PIAA Complex Mask Lyot Coronagraph (PIAACMC), shown in the bottom right of this figure, offers the highest performance of all configurations. Credits: Guyon et al. (2010).

2

THEORY AND MANUFACTURING OF CHARGE 2 VECTOR VORTEX CORONAGRAPHS

2.1 Vortex phase mask

2.1.1 Theory

The vortex phase mask (Mawet et al. (2005), Foo et al. (2005), Jenkins (2008), Swartzlander Jr (2009); Mawet et al. (2011), Serabyn et al. (2011)) is a novel approach aiming to overcome the issues faced by the previously described phase masks, which relied on a step difference to create a phase shift. The idea is to produce a continuous phase shift around the optical axis (Figure 2.1). The center is a singularity where the phase is not defined, nulling the light locally and creating an optical vortex. Vortex coronagraphs have a small IWA (down to $0.9\lambda/D$) and high throughput, absence of dark zones limiting the detection, and excellent starlight cancellation.

The helical phase ramp produced by the vector vortex phase mask can be written as $\exp(i\Phi)$ with $\Phi = l\theta$, where θ is the focal plane azimuthal coordinate and l the topological charge: an even number describing the number of times the phase Φ accumulates 2π along the optical center of the vortex (Pancharatnam, 1956). It can be shown mathematically that for a circular aperture and a vortex with an even topological charge ($\neq 0$), the light is fully diffracted outside the geometric image of the pupil and can be stopped by the slightly undersized Lyot stop. The phase ramp can be achieved through two different ways. First, with a scalar vortex: a dielectric material is shaped as an helix to apply the desired phase shift to both orthogonal polarization components of the light. In this case, the vortex is highly chromatic and the manufacturing presents a serious technological challenge in terms of accuracy. The second solution that will be the focus of this thesis is the vector vortex coronagraph (VVC,Mawet et al. (2005) and Delacroix et al. (2010),) and is widely recognized as one of the most promising approaches in coronagraphy.

2.1.2 The subwavelength grating vortex coronagraph

The vector vortex phase masks uses a half-wave plate (HWP) inducing a π phase shift between the light polarizations components, which rotates around the optical axis, to create the phase ramp. For a complete rotation, the HWP produces a helical phase ramp with an overall 4π phase shift. This simple structure corresponds to a charge 2 ($2\times2\pi$) VVC. It has been shown that vector and scalar vortices present the same phase ramp (Mawet et al. (2005); Niv et al. (2006)).

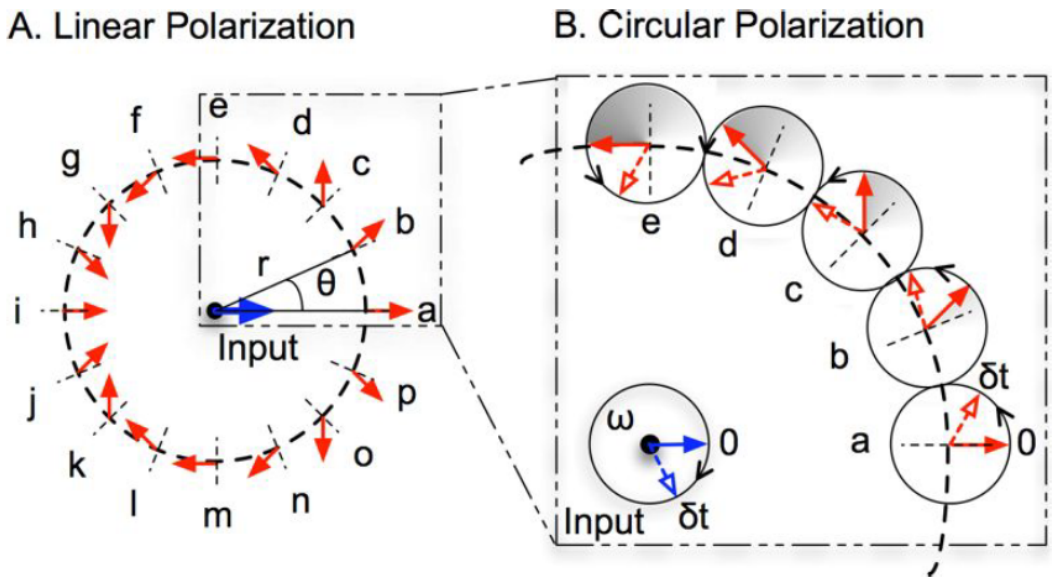

Figure 2.1: The VVC azimuthal phase ramp obtained with a rotationally symmetric half-wave plate (HWP). The rotating optical axis orientation is represented with dashed lines perpendicular to the circumference. The net effect of a HWP on a linear impinging polarization is to rotate it by -2 $\times$ α where α is the angle between the incoming polarization direction and the fast optical axis. An incoming horizontal polarization (blue arrow) is transformed by the vector vortex so that it spins around its center twice as fast as the azimuthal coordinate θ (red arrows). Right: For circular polarization, the starting angle 0 is rotated, therefore the output field rotation is strictly equivalent to a phase delay. From Mawet et al. (2011).

VVCs have been manufactured using 3 different technologies: liquid crystal polymers (LCP), photonic crystal polymers (PCP) and subwavelength gratings (SG). Among these technlogies, only SG are currently mature for applications in the mid-infrared domain (a spectral range of great interest, see Section 2.2).

This thesis focuses on subwavelength grating vortex coronagraphs (SGVCs). Subwavelength gratings have unique properties in terms of light diffraction. Only the zeroth order propagates as long as the period of the grating Λ is smaller than λ/n (n being the grating refractive index). In this case, it has been demonstrated that one can use the birefringence induced by etching a subwavelength grating on top of a transparent substrate in order to produce a spatially variant achromatic half-wave plate (HWP, Kikuta et al. (1997)). The phase shift depends on two factors: the wavelength and the difference between the two refractive indices of the HWP (which are also related to the wavelength). Physical parameters of the SG can be tuned to make

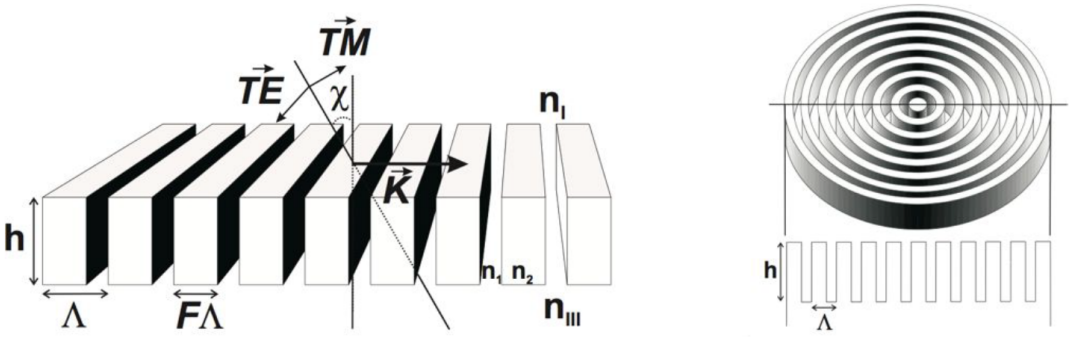

Figure 2.2: Left: Schematic diagram of a SG. The incident light beam vector is perpendicular to the grating lines of depth h and a periodicity Λ. The filling factor F is such that FΛ corresponds to the width of the grating walls. Right: AGPM coronagraph scheme. From Mawet et al. (2005).

the two factors proportional and create a close to achromatic HWP across a large spectral band. The achromaticity is a much needed feature for coronagraphs to operate over a large wavelength range, allowing spectral analysis and a significantly higher signal-to-noise ratio (SNR). Since the SG is not perfectly achromatic along the spectral band, a coronagraph using this technology will never produce a perfect cancellation of the star light due to chromatic errors in the π phase shift induced between the two orthogonal polarizations. The textbook effect of chromatic errors is to produce a scaled-down version of the non-coronagraphic PSF. The ratio between the original and the scale down PSF will define the performance of such a mask (see Section 3.1). A charge 2 VVC using SG has a simple pattern and is called the Annular Groove Phase Mask (AGPM, Figure 2.2).

2.2 AGPM design and manufacturing

2.2.1 Design

The MIR wavelength range is a sweet spot for the direct imaging of young planetary systems, where good wavefront quality can be obtained from the ground with standard adaptive optics correction. The luminosity ratio between thermal emission of a young exoplanet and its host star is also maximized in this region.

To answer the growing demand for coronagraphs in the H- (1.44 to 1.78 μm), K- (1.95 to 2.35 μm), L- (3.5 to 4.1 μm), M- (4.6 to 5 μm) and N- (11 to 13.2 μm) bands, SGVC (subwavelength grating vortex coronagraph) solutions have been developed and optimized for those regions. AGPMs are designed and optimized using Rigorous coupled-wave analysis (RCWA, Moharam and Gaylord (1981)) to model an optimal π phase shift between the two transverse modes of the light across the spectral band considered. RCWA is a Fourier-space semi analytical solving method for grating diffraction. Four parameters are taken into account, the period of the grating Λ, the filling factor F (ratio between the walls width and the period Λ), the depth h of the grooves and the sidewall angle α (usually constrained between 2.5° and 3° due to manufacturing limits). The 4 parameters are optimized within the realistic model

Table 2.1: Optimal grating parameters for various spectral windows (20% bandwidth) using RCWA simulations. From Delacroix (2013).

20% BW		Gratings parameters				Rejection ratio
Filter	Range (μm)	Λ (μm)	$\alpha(^\circ)$	F	h (μm)	
N	11-13.2	4.6	3.0	0.45	16.9	2354
L	3.5-4.1	1.42	3.0	0.45	5.21	2457
K	2.0-2.4	0.82	3.0	0.45	3.02	2366
H	1.5-1.8	0.61	3.0	0.45	2.26	2341
J	1.15-1.4	0.48	3.0	0.45	1.75	2353

conditions that were set after an iterative process between design and manufacturing. In Table 2.1 are displayed optimal parameters for each spectral band depending on the sidewall angle (α).

The RCWA method solves Maxwell's equations through a discretized AGPM layer by layer. The limitations and approximations in the RCWA modeling of the AGPM are beyond the scope of this thesis but are further discussed in Delacroix (2013) and Mawet (2006). We consider RCWA performance simulations as an accurate description of the AGPM theoretical limits.

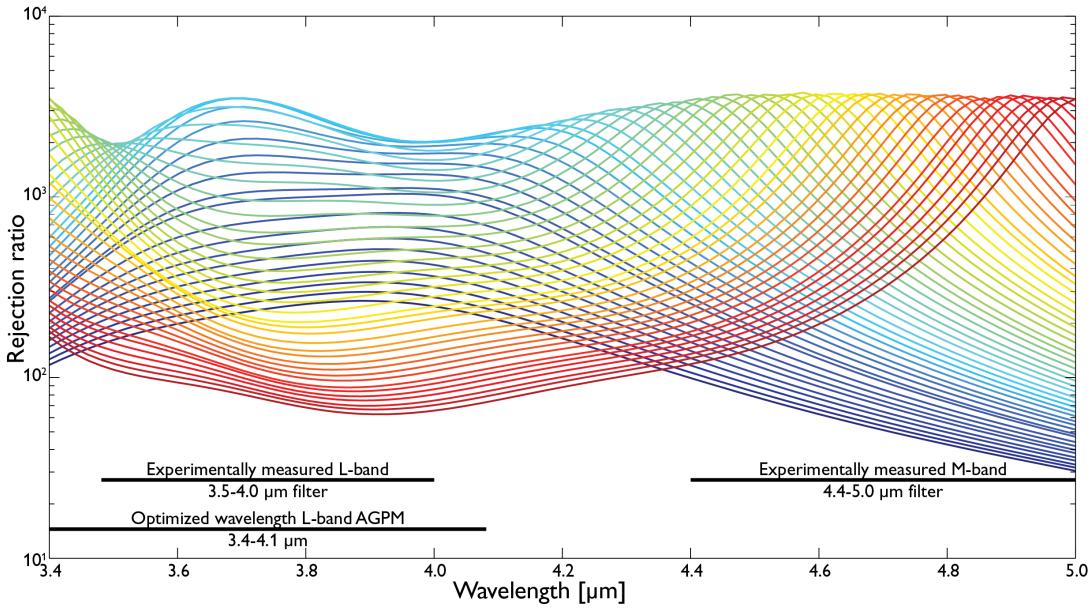

Figure 2.3: Best rejection ratios achievable for AGPMs with optimal parameters in different spectral bands, the grating depth is varied between 5.0 and 6.0 μm from blue to red, with the lines separated by steps of 0.02 μm. The sidewall angle is set to 2.45°. From Vargas Catalán et al. (2016).

The Figure 2.3 illustrates the best null depth achievable across a the L- and M-bands with various gratings depths and otherwise optimized parameters. However, we have to take into account that most likely the manufactured AGPMs will not perfectly reached the exact optimal parameters. The Figure 2.4 shows how the deviation from the optimal filling factor or depth will affect the null depth of a given AGPM.

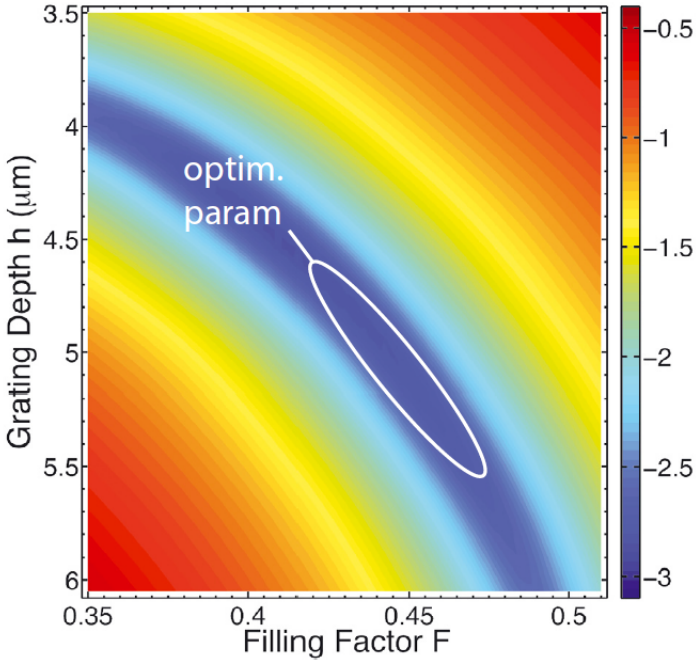

Figure 2.4: RCWA multi-parametric simulation: mean null depth (logarithmic scale) over the whole L band (3.5-4.1 μm) with α ranging from 2.7° to 3.2°. The period is set to Λ = 1.42 μm (SG limit). From Delacroix et al. (2013).

Details about the modeling of SG can be found in the following publications : Mawet (2006) and Delacroix (2013).

2.2.2 Manufacturing

AGPMs are manufactured by our collaborators at the Uppsala University in Sweden. They are etched on a synthetic diamond substrate which has been selected for its unique characteristics:

- transparency in the MIR
- high refractive index
- good mechanical resistance, low thermal expansion, resistant to chemicals

Several steps are needed to produce an AGPM (see Fig 2.5). The diamond substrate is coated with different metal layers. The AGPM pattern is printed in a photoresist layer coated on top. The different layers are etched to finally obtain the diamond AGPM. Scanning electron microscope or other non-invasive methods can not verify all the parameters of the newly etched AGPMs (in particular the groove depth). To partially solve this issue, a test sample is etched at the same time as the AGPM and cracked after each layer etched to monitor the process and tune it accordingly. The process was described in details in the following papers: Forsberg and Karlsson (2013), Delacroix (2013), Vargas Catalán et al. (2016) and Catalán et al. (2018).

The first AGPMs have been optimized for the N-band since it is in this band that the grating parameters are the largest making the first manufacturing trials

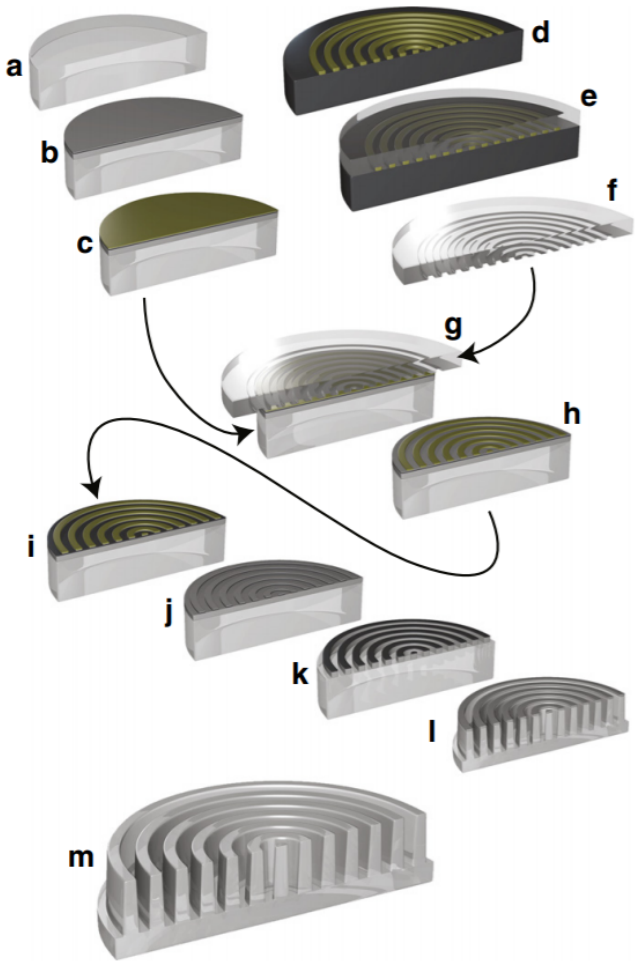

Figure 2.5: Process steps in brief. Diamond substrates are cleaned in solvents and acids (a). Three masking layers are sputtered onto the diamond substrate (b): a thick Al layer, followed by a Si layer and finally a thinner Al layer. A layer of nanoimprint polymer is then spin coated on top of the stack (c). The patterns are written to silicon wafers either by laser- or by e-beam lithography (d). A thin layer of polydimethylsiloxane (PDMS) is molded on the patterned wafer (e) and peeled off (f). The structured PDMS is used as stamp in nanoimprint lithography to transfer the pattern to the polymer film at the top of the mask stack on the diamond substrate (g, h). Plasma etching is employed to texture the diamond surface in the following way: the thin polymer pattern is used as mask to etch the pattern in the top Al layer in a Cl2/BCl3 plasma (i). The Si layer is then etched using the top Al layer as mask in an Ar/SF6 plasma (j). The Si layer serves as mask for etching the thick Al layer in cycled Cl2/BCl3 and O2 plasmas (k). With the Al mask finished, the diamond is etched in an Ar/O2 plasma with strong bias (l). Finally, remaining mask material is removed with strong acids (m). From Forsberg and Karlsson (2013).

easier (grating parameters are proportional to λ). Over the years, the process has been perfected (Figure 2.6) and reached outstanding accuracy enabling shorter and shorter wavelengths range for the AGPM. Once manufactured, the AGPMs have their performance assessed before their potential installation on large ground-based

telescopes. Developing a testing facility capable to accurately measure their performance and describe their behavior is the main subject of this thesis.

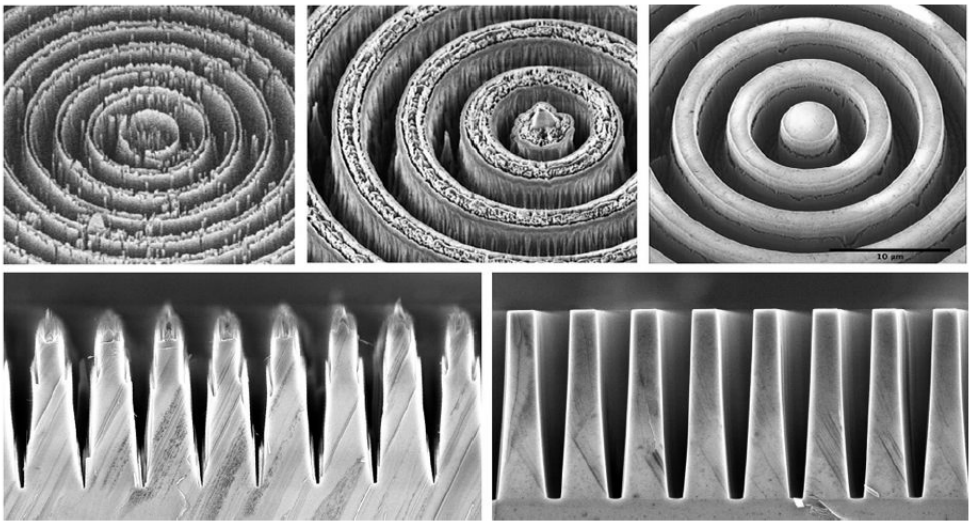

Figure 2.6: Evolution of the manufacturing of diamond AGPMs. Top: N-band AGPMs, with periods $\approx$ 4.6 μm, manufactured in November 2009, October 2010, and February 2012 (from left to right). Bottom: cracked spares of L-band AGPMs, with periods $\approx$ 1.4 μm, manufactured in March 2011 and September 2012 (from left to right). From Delacroix (2013).

2.2.3 Anti-reflective gratings

The first AGPM manufactured had lower than predicted rejection ratio as the on-axis light reflected inside the AGPM was not canceled by the optical vortex. Fixing this issue is mandatory to reach performance close to the simulations and also to improve the throughput of the AGPM since coronagraphic instruments usually have to face the issue of low flux observations.

To avoid internal reflections, instead of a single layer film it is possible to use SG as an anti-reflective intermediate medium (Figure 2.7). The refractive index of a SG can be tuned by adjusting its filling factor and take the appropriate value to minimize the total reflectivity of the AGPM (Karlsson and Nikolajeff, 2003). Delacroix (2013) described a $\sim$17% backside reflection of the bare diamond substrate in the L-band, reduced to $\sim$1.9% thanks to the ARG. The theoretical transmission in the L-band is averaged to $\sim$87% at L-band (limited by photon absorption in the diamond substrate, Forsberg and Karlsson (2013)).

Experimental results on the ARG are detailed in section 6.3.

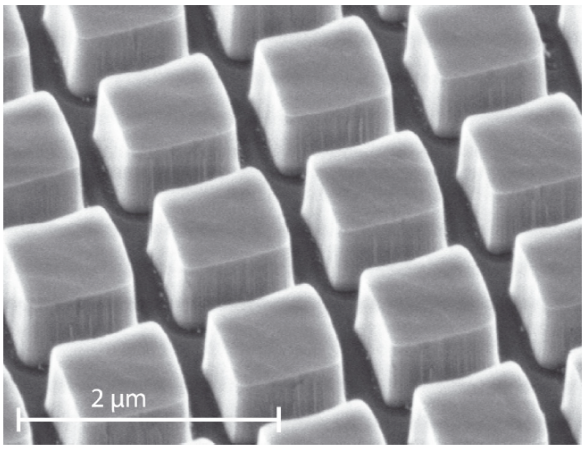

Figure 2.7: SEM picture of the anti-reflective grating (ARG) etched on the backside of the AGPM. From Delacroix (2013).

PART II

Development of the VODCA bench

3

CONTEXT AND HERITAGE

We describe in this section how the AGPM performance was assessed until 2014. These tests helped us to define how to achieve the best measurements of our phase masks and what were the requirements in the development of a dedicated test bench.

3.1 Test protocol

The AGPM test protocol aims to provide an accurate method to assess their performance, allowing a fair comparison between the different manufactured AGPMs and their corresponding data collected throughout the past years. Following Delacroix (2013), we chose to evaluate the mask quality with its null depth. The null depth is the flux ratio between two images, one with the beam focused on the center of the mask (on-axis, the PSF is attenuated) and one off-axis (the PSF is not attenuated). By decentering the mask by at least 2 mm ($> 10\lambda/D$) we make sure that the off-axis PSF is not affected by the vortex effect but still takes into account the transmission of the mask. The flux is only integrated in a defined zone of the PSF. An extremely small integration zone would be similar to the peak-to-peak attenuation. It is commonly used for coronagraphic evaluation but not selected in our case since the AGPM (when on-axis) significantly changes the shape of the PSF. Using this method would not accurately described the mask performance. On the opposite, an extremely large integration zone (the full image) would include an important background and speckle noise.

Defining the integration zone as λ/D, which roughly corresponds to the full width at half maximum (FWHM) of the PSF, is the most appropriate choice. Most of the intensity is contained within this diameter, limiting the loss of information and increasing the signal-to-noise ratio. The null depth equation is:

$$ND_{AGPM} = \frac{\int_0^{FWHM} \int_0^{2\pi} I_{off}(r,\theta)\, r\, d\theta\, dr}{\int_0^{FWHM} \int_0^{2\pi} I_{cor}(r,\theta)\, r\, d\theta\, dr}, \tag{3.1}$$

where I_{cor} and I_{off} are the averaged coronagraphic and off-axis images (see Delacroix (2013)). The rejection ratio, defined as 1/ND, is also commonly used and will be the main indicator of the AGPM performance in this thesis.

Table 3.1: Rejection ratios measured on IRCT with the He-Ne and the L-band source (AGPM and ARG refer to the mask side facing the beam).

	He-Ne		Broadband	
	AGPM	ARG	AGPM	ARG
AGPM-L2			38	
AGPM-L5	169		349	
AGPM-L6	208	171	87	93
AGPM-L8	28	31	41	32

3.2 Existing facilities for AGPM tests

Performance assessment of AGPM requires a coronagraphic test bench with specific optical equipment and configuration. The minimum optical equipment is an infrared point source in the wavelength range of the masks and the appropriate detector. The basic configuration includes the access to one focal plane (where the AGPM will be placed) and after it, a plane conjugate to the entrance pupil (where the Lyot stop will be placed). It follows the classic coronagraphic setup (see Section 1.3).

3.2.1 IRCT

In July 2014, L-band AGPMs were tested on the InfraRed Coronagraphic Testbed (IRCT located at the Jet Propulsion Laboratory, Pasadena, USA). It includes a faint broad band thermal source with a filter limiting the spectral band from 3440 to 4075 nm. Unfortunately the source had a low flux output leading to a poor SNR especially for the on-axis PSF where the initially low flux is divided by a ratio >100. A He-Ne laser at 3.49 μm was also available (Fig. 3.1). The f# on the AGPM is 17 and we had the possibility to image the pupil plane. Unfortunately no shutter was available on the bench. For the background subtraction, the background frame was taken after the science frame by turning off or blocking the source output. It led to an imperfect subtraction because the background fluctuated fast enough to make a noticeable difference (see Section 6.1 background frame subtraction).

On top of the rejection ratio measurements (Table 3.1), we also tested the influence of the phase mask side facing the beam (AGPM or AR grating). No evidence was found suggesting that the orientation of the phase mask affects either the rejection ratio achieved or the radial profile of the coronagraphic PSF.

The AGPM focus and tip/tilt sensitivity were also investigated. To do so, the phase mask mount was shifted along the beam for defocus (z axis), and perpendicularly to it (x or y axis) to simulate tip/tilt instead of really tilting the wavefront. The only difference between these two methods is that the PSF is not translated on the detector when the AGPM is translated, however, the shape of the PSF is affected in the same way. For each position, the rejection ratio was evaluated. Concerning the defocus (see Fig. 3.2), the rejection ratio has been estimated in two different ways. First, the usual way (see Section 3.1), by integrating in the FWHM zone of the PSF (rejection ratio). Second, integrating the flux in a larger area (4 times the FWHM). Even if this approach is not optimal for AGPM performance assessment (see Section 3.1), it seems more appropriate for this study as it is clear that even if the flux at the center of the PSF does not significantly increase with defocus, the light leaks in the

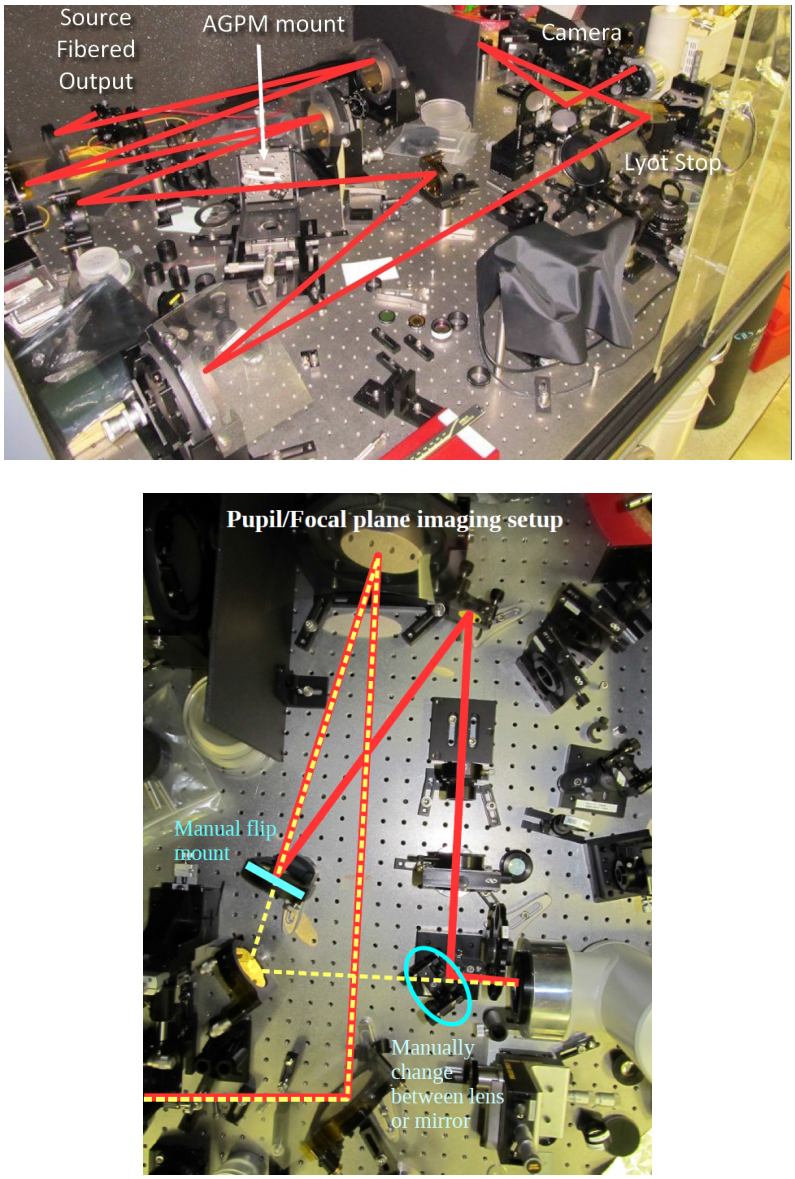

Figure 3.1: Pictures of IRCT. Top: layout of the coronagraphic bench. Bottom: Difference between the focal plane and the pupil plane imaging setup

first annuli of the PSF, reducing the contrast performance.

We conclude that a misplacement of the AGPM by $\pm$ 300 μm did not significantly influence (less than 5% decrease, see Fig. 3.2) the rejection ratio achieved on IRCT and the mask performance.

The same procedure was applied to tip/tilt shift (Fig. 3.3). When observing with a telescope, the light leaking in the image is related to the amount of tip-tilt affecting the beam. These measurements contributed to the development of the Quadrant Analysis of Coronagraphic Images for Tip-tilt Sensing, QACITS (Huby et al., 2015).

In conclusion, IRCT was a good starting point for AGPM evaluation and allowed a better understanding of the needs for high rejection ratio evaluation (proper background subtraction and source power). It also emphasized the major role played by tip/tilt alignment on the rejection ratio achieved (discussed in details in Section

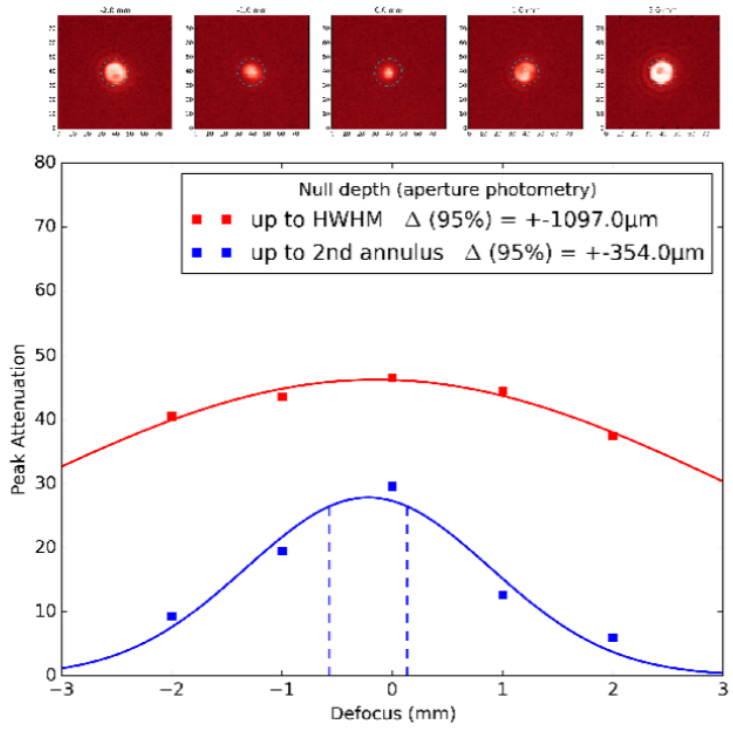

Figure 3.2: Influence of the defocus on the rejection ratio. The flux is integrated over the FWHM (red curve) and up to the second annulus of the PSF (blue curve)

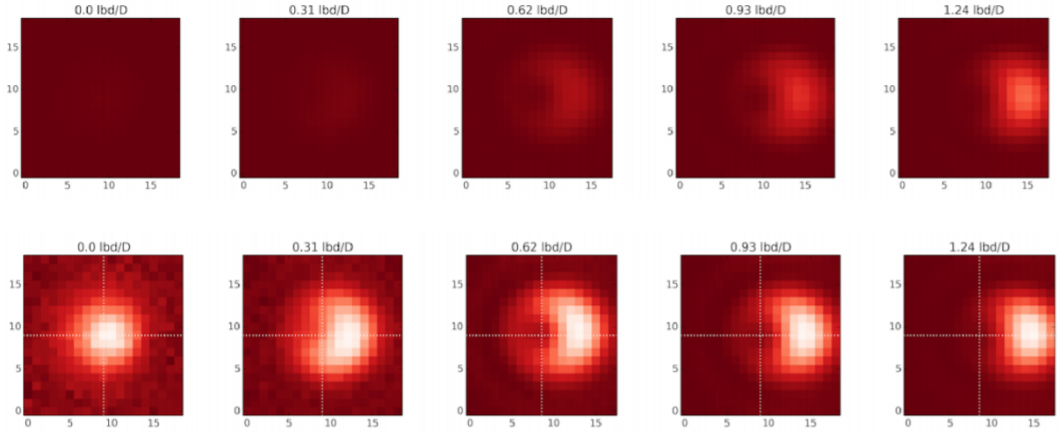

Figure 3.3: Tip influence on the PSF shape. Top: same scale – Bottom: adjusted scale

7.2.1). On the contrary, AGPMs showed a relatively lower sensitivity to focus misalignment (discussed in details in sect 7.2.2).

3.2.2 YACADIRE

YACADIRE is a test bench from the Observatoire of Meudon (France). Its detailed description can be found in Delacroix (2013). It was the main facility where we used to test our AGPMs until 2014. AGPMs were tested in L, K and tentatively also M bands. We also tested the peak attenuation evolution when tip or tilt are applied.

Limitations

YACADIRE's limitations in the AGPM performance evaluation have been clearly identified throughout the years. As stated in Section 1.5, the vortex best nulling effect takes place when the PSF is perfectly aligned with the center of the phase mask. Slight shift from this position implies a decrease of the rejection ratio (discussed in Section 3.2.1 and 7). As a consequence, any factor resulting in a non-perfectly aligned PSF decreases the achievable rejection ratio. The main limiting factor on YACADIRE is the manual alignment of the AGPM. The 10 μm incremental step of the AGPM mount manual actuators did not allow us to effectively find the best position. Repeating the alignment several times and selecting the best rejection ratios was our solution to partially overcome this issue. This time-consuming method still left us with a non-negligible error on the alignment. Mechanical vibrations and air turbulence were less critical factors even though they caused jitter, also resulting in shifting the PSF position on the mask. The source limited power (set at the maximum) was also an issue since it only left the integration time of the camera as a variable to handle the dynamic range in intensity between off- and on-axis PSF. High-flux cases were quickly solved by decreasing the integration time. However, low-flux cases (it includes most of on-axis vortex phase mask measurements) still remained an issue since the integration time has an upper limit which corresponds to the background saturation of the detector while several integrations can be co-added to increase the SNR, the initial alignment still relies on individual integrations, where we need to be able to identify the coronagraphic PSF.

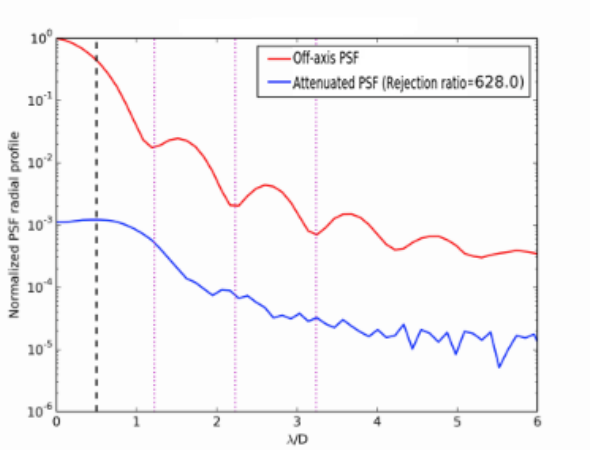

Figure 3.4: Rejection ratio measured on YACADIRE for AGPM-L15.

Considering the limitations stated above and the fact that the AGPM was manually aligned based along the indications of the individual (background-subtracted) images, in the case of high performance AGPM (rejection ratio > 500), the minimum of the attenuated PSF intensity could not be precisely found due to low signal-to

noise ratio resulting in less reliable alignments and measurements of the on-axis leakage term. There was no control of aberrations on YACADIRE to compensate misalignment and non-perfect surface quality of the optical elements. Therefore, the last factor limiting the performance was the wavefront quality. However the typical off-axis PSFs radial profile stayed close to the theoretical Airy pattern and several annuli were visible (Figure 3.4). It indicates an overall acceptable, yet improvable, wavefront quality on the bench. The coronagraphic PSF gives us more information on the bench aberrations. The intensity is constant until approximately λ/D, while it should peak on axis and then decrease rapidly (as the off-axis PSF). It indicates the presence of low order optical aberrations. Some of them (tip/tilt and focus) could have been reduced by a more accurate alignment.

In conclusion, considering the best performance measured on YACADIRE (see table 3.2), 10^3 can be considered as the upper limit on the achievable rejection ratio. The masks have been measured repeatedly and the dispersion of the measurements led us to estimate typical statistical error around 15%.

Summary of AGPM tests

Following the conclusion reached in Section 3.2.1, the AGPM side facing the beam plays little to no role in the rejection ratio achieved. Other tests were run on focus and tip/tilt influence giving the same results as on IRCT. Here are summarized the best rejection ratios measured on YACADIRE for each AGPM available at the time.

Table 3.2: Best rejection ratio measured on YACADIRE.

AGPM	Rejection ratio
AGPM-L4	500 $\pm$75
AGPM-L5	620 $\pm$93
AGPM-L8	60 $\pm$9
AGPM-L9r2	397 $\pm$60
AGPM-L11r	984 $\pm$148
AGPM-L14	370 $\pm$56
AGPM-L15	628 $\pm$94

3.3 Need for a Liège-based dedicated test bench

On YACADIRE, the rejection ratios measured over the L-band were limited to a maximum of 10^3. RCWA simulations predict that the rejection ratio of the AGPMs can reach up to 2.5×10^3 considering realistic grating parameters. Because our applications are essentially ground-based, reaching such a high rejection rate is largely sufficient, as the actual on-sky rejection rate will generally be limited to a few hundred due to atmospheric turbulence and by the particular shape of the telescope pupil (central obscuration, spider arms). Yet, measuring the intrinsic performance of AGPMs is still crucial, because such measurements allow us to derive the exact parameters of the subwavelength grating, and thereby evaluate the quality of the manufacturing process.

To this end, a Liège-based test bench has been designed. A first requirement is to achieve a high signal-to-noise ratio. The source has to deliver enough power to overcome the loss of power due to the bench configuration and the coronagraphic effect considerably decreasing the flux reaching the detector. Simulating a star as a point source with enough power requires one or several lasers, which have to operate in the different infrared bands (H, K, L, M) for which the AGPM have been designed (sect 4.3). The thermal background emission at room temperature (around 300 K) peaks in the mid-infrared around 10 μm. In the 1 to 5 μm region we are interested in, this emission is still significant. The detector has to be cooled down when operating in this range of wavelengths to avoid being flooded by its own thermal radiation. The pixel pitch of the detector has to be small enough to properly sample the PSF. The choice of the camera will be discussed in sect 4.4. As mentioned in Section 3.3, the AGPM alignment accuracy is a priority to reach higher rejection rates. Motorized actuators with incremental steps small enough compared to the PSF size ensure an optimal positioning of the mask. In addition, a deformable mirror is needed for wavefront control and for the evaluation of the impact of aberration on the rejection ratio.

4

DESIGN AND HARDWARE

In this section, the current configuration of the Vortex Optical Demonstrator for Coronagraphic Applications (VODCA) is presented and the optical elements of the bench are detailed.

4.1 Bench layout

The VODCA optical bench layout displayed in Figure **?** fulfills the previously stated requirements. The first part of the bench implements the beam shaping (shutter, neutral densities and spectral filters) while the second part is dedicated to coronagraphy. In this configuration the deformable mirror defines the entrance pupil. All of its actuators are used so that the full potential of the DM is reached, but it presents one drawback. Considering the 8.7° angle of the incoming beam compared to a normal incident beam, the actual pupil defined by the DM is not perfectly circular. Nevertheless, it can be approximated as circular since the ratio between the horizontal diameter (affected by the beam angle) and the vertical diameter (not affected) of the pupil is 0.988.

A previous configuration of the bench involved two off-axis parabolas (OAPs) around the DM. They were set up after the beam shaping part. The advantage of such a configuration was the access to another pupil plane between the OAPs, where the DM was positioned. The second pupil plane between the two full parabolas was used to tune the diameter of the beam up to 30 mm. The Lyot stop was shaped accordingly. This solution was abandoned for two reasons: (i) the alignment complexity added to VODCA and (ii) the OAPs surface quality introduced optical aberrations which, combined with potential misalignment (introducing astigmatism and coma mostly), could not be properly corrected for by the DM. VODCA offers the possibility to switch to a layout without deformable mirror (details in sect 10). A diaphragm with the same diameter as the DM replaces it (and the two plane mirrors) and defines the entrance pupil. To keep the Lyot stop in a conjugated plane with the entrance pupil, the diaphragm has to be set at a designated position between the parabolas.

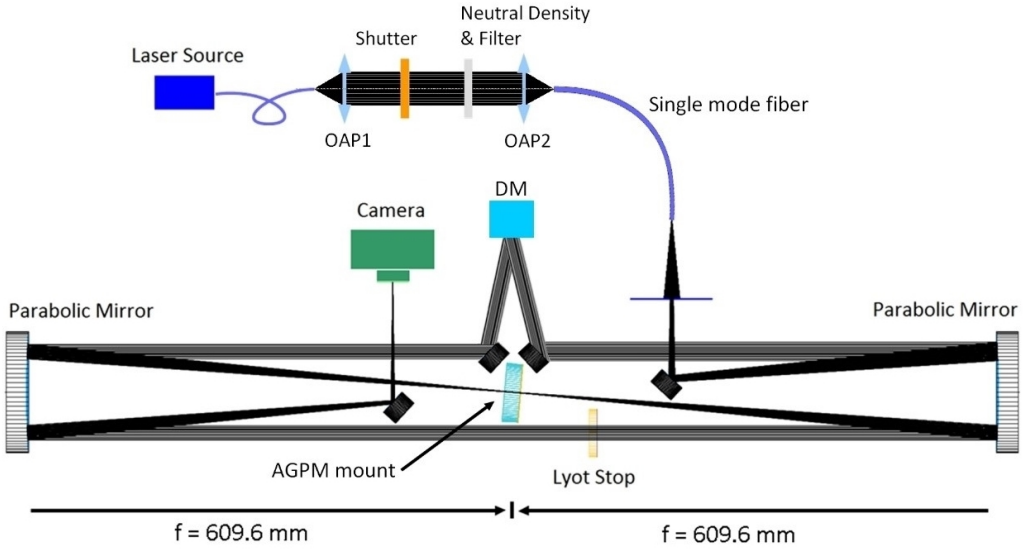

Figure 4.1: VODCA current configuration including the deformable mirror.

4.2 Optics

VODCA has been designed as a fully reflective bench to avoid chromatic aberrations while working over a broad range of wavelengths. Gold and aluminum coatings were selected to ensure the highest reflectivity of the surfaces. They guarantee a minimum reflectivity of 95% in the spectral range where VODCA operates (1 to 5 μm). Two silver-coated off axis parabolas from Edmund Optics are used in the "beam shaping" part. In the coronagraphic part, we use regular Thorlabs gold-coated flat mirrors and two silver-coated parabolas (Edmund Optics) at f = 609.6 mm. An achromatic doublet lens (Thorlabs) optimized between 3 and 5 μm is also available. Located before the camera, it allows to image the pupil plane if needed. In its standard configuration (with DM), VODCA has a f# of 45 on the AGPM. The core size of the PSF (FWHM) is $1.028\lambda \times f\#$. In the L band it varies from 167 to 190 μm.

4.3 Sources

All the lasers used have a fibered output to easily switch between them and guarantee the same source position. We choose single mode fiber output to guarantee an aberration-free wavefront.

4.3.1 Red alignment laser

A red He-Ne 632nm laser, that we inject in a fiber, is used for alignment. The alignment procedure is detailed in Section 4.8.

4.3.2 Supercontinuum laser

Description and optimal use

The Supercontinuum (SC) laser from Le Verre Fluoré offers the perfect solution to the requirements of our bench. The SC laser is made of a high power, pulsed monochromatic laser at 1.55 μm. This pumped laser is injected into a fluoride fiber where non-linear effects produce spectral broadening. The output fiber delivers a 255mW beam at maximum power, its core diameter is 8.5 μm with a 0.23 numerical aperture (NA). The SC delivers a continuum spectrum from 0.8 to 4 μm, single mode above 1.6 μm. It therefore allows us to cover the H, K and L bands (H: 1.44-1.77 μm, K: 1.95-2.35 μm and L: 3.5-4.1 μm). It has also the advantages of a laser, a spatially coherent and high power beam. The higher flux output is a significant improvement for the SNR compared to the source used so far on YACADIRE (a tungsten lamp injected in a single-mode fibre, see Section 3.3.2). Using the SC laser, the AGPM will be evaluated in similar spectral conditions (continuous spectrum in the chosen infrared band) as on the telescopes where they will be installed.

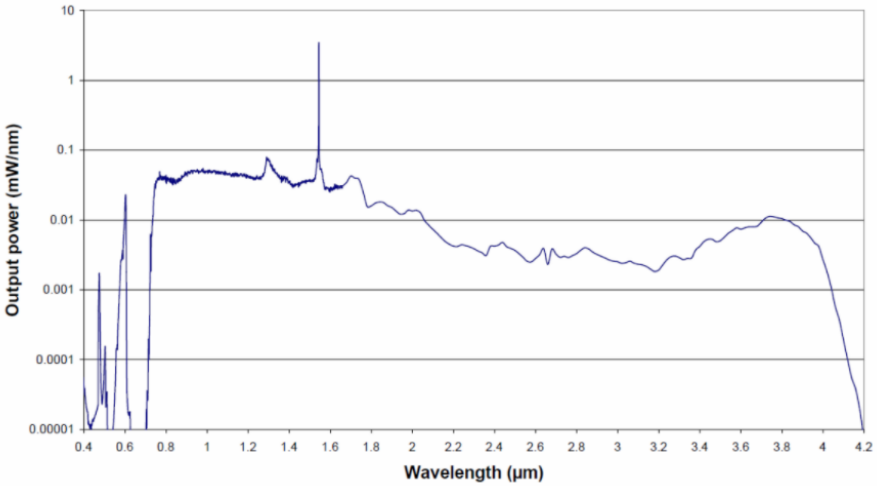

Figure 4.2: Supercontinuum spectrum delivered at full power (from Le Verre Fluoré).

Stability

A flickering phenomenon has been observed while operating the SC laser. It can be caused by two factors:

1) Small integration time. The pump laser has a repetition rate of 100 kHz with 0.7 ns pulses. Each pulse has an average power of 2μJ. As a consequence, any integration time will average a number of pulses that can vary. For small integration time (shorter than 100μs) this variation is significant enough for a flickering to be observed. For the source to be approximated as continuous, the integration time on the detector has to be longer than 1 ms to average at least 100 pulses (see Section 4.4.).

2) Pump laser power. The spectrum broadening, produced by a non-linear effect, depends mostly on the power of the pumped laser. The broadest spectrum is only

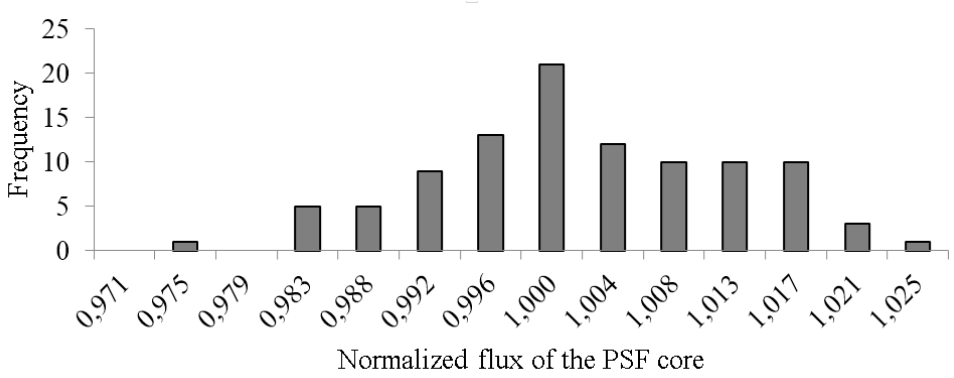

Figure 4.3: Histogram of the PSF core total flux considering 100 frames.

available at full power (Fig. 4.2). At the higher or lower end of the spectrum, sub optimal operating power will produce large fluctuations since some pulses might not be powerful enough to create a spectrum reaching this range of wavelengths. The solution is to always operate at maximum power. In standard operating conditions, the Super Continuum laser power is set at the maximum. The flux variation was evaluated in regular L-band AGPM performance assessment conditions (i.e. with the L-BBF filter, a neutral density (see Section 4.6) and the lowest exposure time commonly used, 1ms). The result is shown in Fig. 4.3, the flux is normalized with respect to the average of the data collected.

The average flux here is 479981 and the standard deviation is 4957. The distribution has its peak close to the mean and the peak-to-valley flux variation represents 5% of the average flux. Increasing the exposure time does not change noticeably this ratio (4.5% peak-to-valley fluctuation measured for 2 ms exposure time frames). The influence of the source flux variation is further discussed in Section 6.5.

4.3.3 1.55 μm laser and M band quantum cascade laser

Two monochromatic sources are available on VODCA. For characterization at 4.6 μm, we used a quantum cascade laser (QCL) from Alpes lasers, which delivers a single-mode narrow-line emission around 4.6 μm. The laser is fiber-coupled, which allows us to use it in place of the SC laser just by switching the input fiber to the bench. We typically operate the source in a low flux regime and at a temperature of 25°C. At a constant temperature, this laser source is very stable and we measured on VODCA little to no flux variation (<1% rms). We consider adding a second QCL at 5.0 μm for a better coverage of the M-band. A 1.55 single-mode μm laser was also used before the Supercontinuum laser was available.

4.4 Camera

Considering the operation range of our SC and QCL sources, the camera had to operate at least in the 1.6-4.6μm wavelength range. The most appropriate solution was found to be the FLIR A6700sc camera. The detector is a 512×640 15μm pixels array sensitive from the end of the visible light spectrum up to 5μm in the infrared. We do not use build-in lenses with the camera since it would shorten the operating

spectrum from 3 to 5μm and introduce chromatic aberrations. Most of our measurements require to evaluate the flux in a strictly defined area, which is the PSF core. We also need accurate measurements of the rest of the PSF to provide information about aberrations and SNR. For this purpose, it is necessary for the camera to properly sample these zones.

As an Airy pattern, the PSF full width at half maximum (FWHM) is defined by:

$$FWHM_{AGPM} = 1.028\,\lambda\,f\# \tag{4.1}$$

Assuming 3.6μm and 4.1μm as extreme values for wavelengths (λ) allowed by our broad L-band filter, the PSF core size varies between 167 and 190 μm on the AGPM. Since the Lyot stop reduces the beam size by 20% after the phase mask, the f# is multiplied by 1.25 (1/0.8 = 1.25). It increases the size of the PSF on the detector by the same factor. Taking into account the specifications of the camera (15μm pixel pitch), between 14 and 16 pixels are sampling the PSF core, which provides enough details on the PSF shape.

The camera is cooled down to 77 K to decrease the background radiation of the detector itself (see sect 3.3). The integration time can vary from 480 ns to several seconds but is generally set between 1 and 5 ms (compliant with source flux fluctuations, sect 4.3.2). The frame rate goes up to 480 Hz. The drawback of such a device is the time needed to reach the 77 K temperature (between 10 and 15 min) and the vibrations introduced by the built-in cooling system. The vibration issue was limited to a reasonable amount with a wide sturdy mount. The effects of the vibrations are discussed in Section 6.3.

4.4.1 Linearity

The camera operates with a 14-bit dynamic range (counts from 0 to 16384). The following protocol aims to evaluate the linearity of the camera and define a suitable pixel response range for precise coronagraphic measurements. There we assume that the flux responsivity of the detector as the main source of non-linearity and not the accuracy of the integration time (the resolution is 160 ns according to the manufacturer and the minimum achievable is 480 ns).

Several measurements at different integration time were recorded with only the background emission, as displayed in Figure **?**. A linear equation was used to fit the data set. The relative error of the fit was then computed (see Figure **?**). The integration time, assumed not to be subject to errors, can be translated to pixel counts (in the case of only background emission).

In conclusion, the flux measured on the camera presents less than 0.7% errors from 3000 to 15000 (pixel count).

4.4.2 Operating range

The lowest operating conditions used for the camera was a 1 ms integration time (Section 4.3.3.2). During such a time interval, the minimal pixel count possible (i.e. only background emission) is greater than 3000, which is within the linearity range (Section 4.4.1). Concerning the upper limit, we set it up to an integration time of 4ms. It corresponds to a pixel count of more than 10 000 only due to background emission, which leaves up to 5000 counts of dynamic range for the laser source flux evaluation.

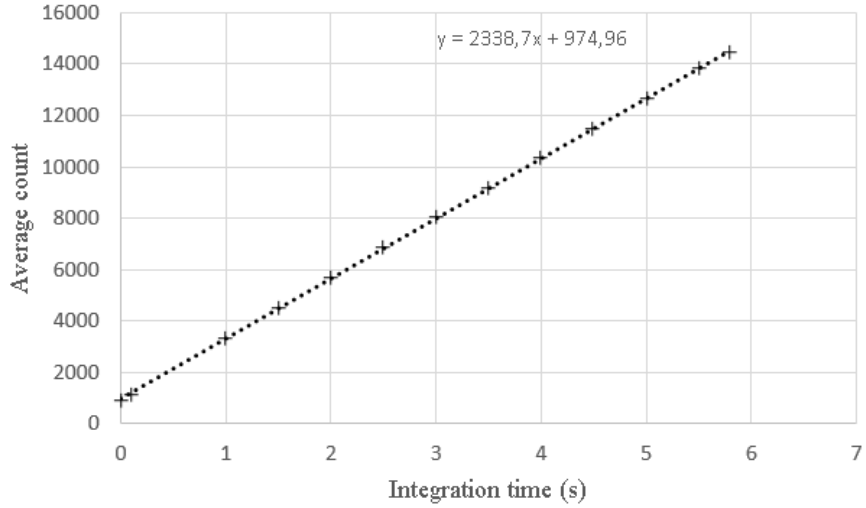

Figure 4.4: Averaged pixel value measuring only the background emission for integration time varying between 0 and 5.8 ms.

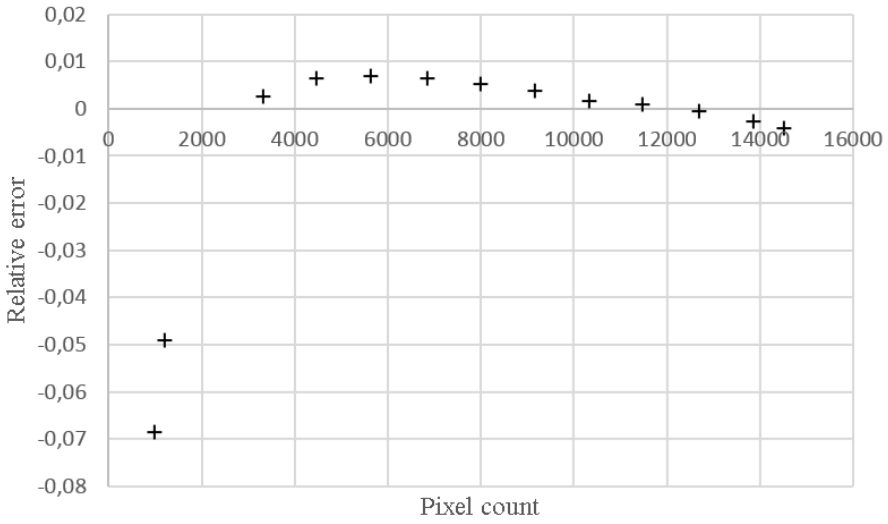

Figure 4.5: Error between averaged pixel value and the fit.

Longer integration times are not recommended since the background emission will get close to the counts limit of the detector leaving only a small dynamic range for the signal, which could lead to non-linearity or saturation in the collected data.

4.5 AGPM mount

As stated before, the AGPM precise centering was one of the most important requirements in the VODCA set up. A Newport precision alignment 3-axis stage guarantees long-term stability with 6 mm travel in the X and Y axes, 13 mm travel in the Z axis (with an angular deviation better than 100 μrad around any axis). A rotation mount

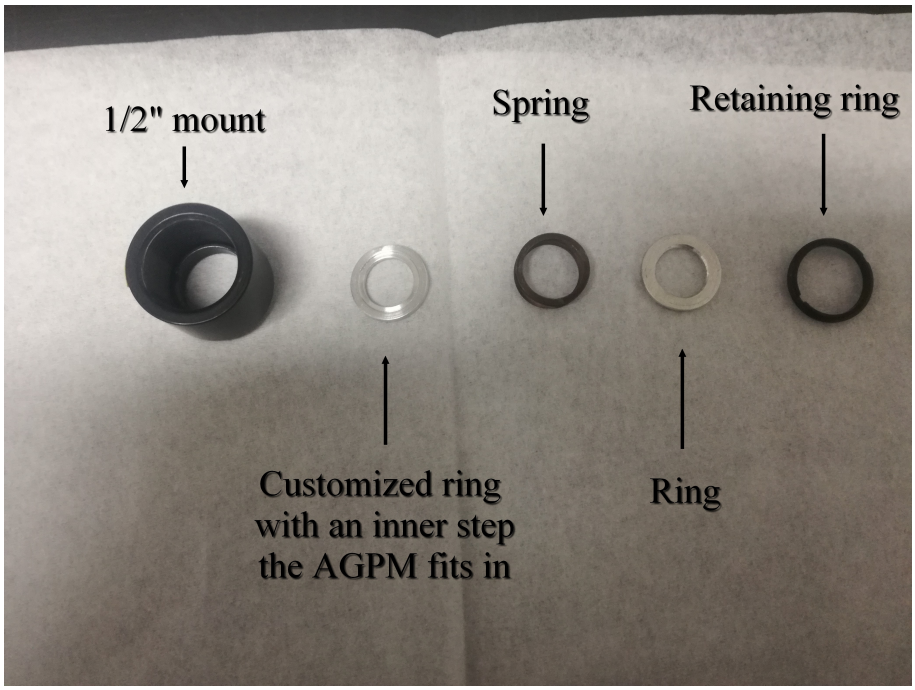

Figure 4.6: Picture of the AGPM mount

is placed on top of it (see Section 8). The complete stage is compact and fits with the bench layout without vignetting the beam. Along the 3 axes, high resolution Newport actuators have been placed. They achieve 10nm micro steps (one step is 160 nm broke down in 30 or 10 nm micro steps). The drawback of such actuators is the repeatability. According to Newport, because of the friction coupling between the piezo legs and the rotating nut, the actual step size is not 100% accurate or repeatable. It can vary from actuator to actuator and depends further on the load, speed, direction of motion and other parameters. This is further discussed in Section 5.1.2.

The AGPM itself is placed in a dedicated mount (see Figure 4.6 and Figure 4.7). It consists of a 1/2" lens tube with two specially designed rings and a spring inside. The mount ensures that the AGPM is always centered inside of the lens tube and always placed at the same position on the bench. A spring is used to safely distribute the pressure on the AGPM and avoid damage from the ring (especially when screwing). Switching from an AGPM to another is easy, saving precious amounts of time when aligning the center of a newly installed phase mask.

4.6 Beam-shaping part of VODCA

The SC laser spectrum covers several infrared bands (Section 4.3.3). To adjust the beam according to our needs in terms of spectral range, we use different filters, one broad- and three narrow-band filters (see Table 4.1) in every band we cover (H: 1.44-1.77 μm, K: 1.95-2.35 μm and L: 3.5-4.1 μm). It is important to characterize our phase masks over representative broadband filters to determine whether they are suitable for integration on ground-based telescopes. Narrow band filters fulfill a different role. The rejection ratio is measured as a function of wavelength and compared to RCWA simulations to infer the corresponding grating parameters. This is a crucial

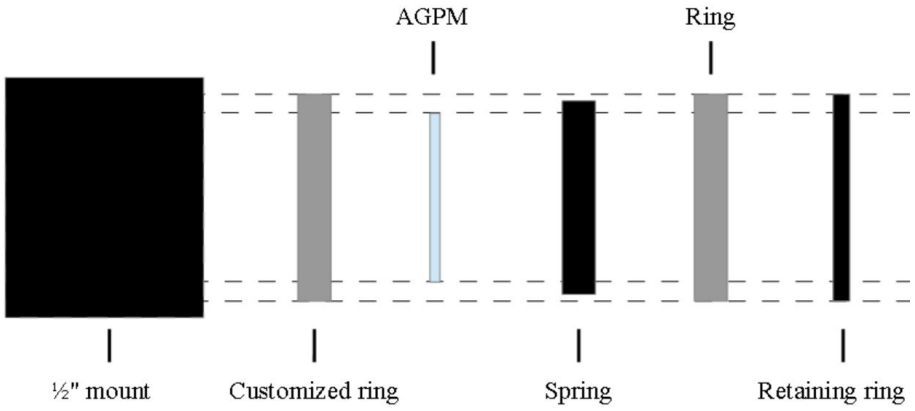

Figure 4.7: Representation of the AGPM mount components inside the lens tube.

step in the characterization of AGPMs, due to the lack of a non-destructive metrological method for the measurement of the grating depth. The optical evaluation is thus necessary to determine whether the grooves have been etched too deep or too shallow, which can subsequently be improved by an additional etching step (see Sections 6.4.1 and 9.1).

Table 4.1: Wavelengths covered by the different filters available on VODCA.

Filter	Wavelength (nm)
H-NBF1	1475-1565
H-NBF2	1592-1657
H-NBF3	1656-1753
H-BBF	1530-1730

Filter	Wavelength (nm)
K-NBF1	1960-2070
K-NBF2	2205-2255
K-NBF3	2295-2345
K-BBF	2000-2500

Filter	Wavelength (nm)
L-NBF1	3425-3525
L-NBF2	3710-3890
L-NBF3	3960-4120
L-BBF	3575-4125

The SC laser power decreases naturally at both ends of the spectrum (Fig. 4.2). Using narrow band filters in these regions leads to a significantly lower signal-to-noise ratio (SNR) compared to a broad band filter. As an extreme example, the SNR with the L-BBF filter (see Table 4.1) is 100 times higher than with L-NBF3. Because the different laser sources on VODCA always operate at a fixed power (Section 4.3) and considering the camera dynamic range (Section 4.4), measuring accurately high rejection ratios (both high intensity off-axis PSF and low intensity on-axis PSF) is not possible with all the different filters. The solution is to use a set of neutral densities (Table 4.2).

Table 4.2: Neutral densities transmission measured on VODCA.

Filter	ND1	ND2	ND1×ND2
L-NBF1	0.1160	0.0125	0.0015
L-NBF2	0.1131	0.0120	0.0014
L-NBF3	0.1108	0.0131	0.0015
L-BBF	0.1150	0.0122	0.0014

The shutter is placed after the laser output. This specific position, upstream the single-mode fiber, guarantees a better background evaluation and subtraction (Section 6.1). The neutral densities, the filters and the remotely controlled shutter form the beam-shaping part of VODCA. A fiber with a 6.3 μm core diameter and 0.23 numerical aperture, providing single-mode behavior above 1.6 μm, connects the beam-shaping part to the coronagraphic part of VODCA. We consider that the beam-shaping part creates a 50% loss of transmission compared to plugging the SC directly to the coronagraphic part. This is due both to the imperfect injection into the fiber, and to the loss of flux that can occur within the first collimator (first OAP) or on the second OAP reflection.

4.7 Deformable mirror

VODCA uses an ALPAO deformable mirror (continuous reflective protected-silver coated surface) featuring 97 actuators on a 13.5 mm aperture (Figure 4.8). The DM has two goals: (i) to correct the static aberrations (see Section 5.2) comparable to non-common path aberrations (NCPA) on telescopes and (ii) to study the influence of optical aberrations on the rejection ratio (Section 7 & 11.3). The distance between 2 actuators is 1.5 mm and a maximum of 60 μm stroke on tip/tilt can be achieved.

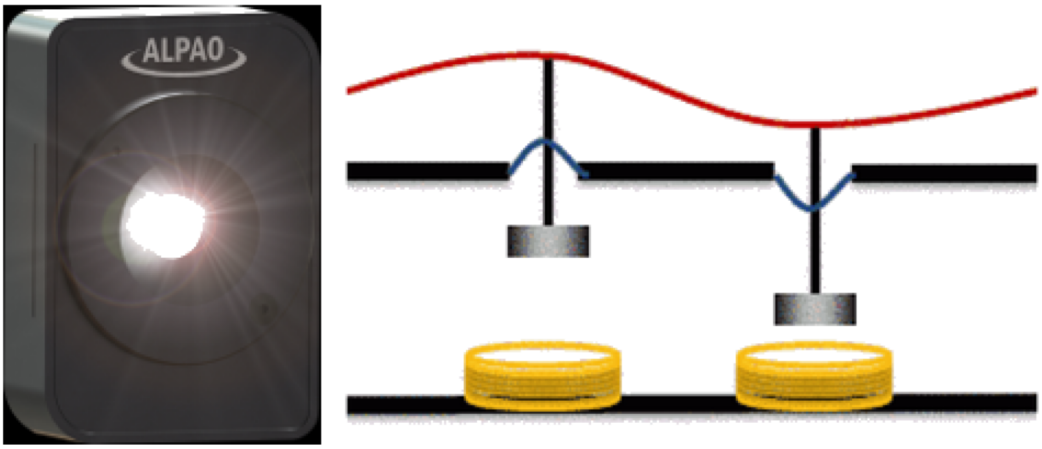

Figure 4.8: Left: Picture of an ALPAO DM. Right: DM surface schematic. By applying a current in the coils (yellow), the magnets (grey, hold by a spring (blue)) are moved up and down to deform the membrane (red). Credits: ALPAO.

On VODCA, we need the intensity on the DM (which defines the input pupil) to be as uniform as possible. The fiber delivers a Gaussian beam but only a small central portion is selected. Considering the 609.6 mm focal length of the parabolas and the DM diameter, it corresponds to selecting only the beams with an angle

$\leq 0.63°$ from the fiber output (less than 5% of the 13.3° acceptance cone of the fiber). The uniformity of the flux intensity at the entrance pupil is not limited by the Gaussian nature of the fiber output but mostly by the roughness of the optical surfaces and diffraction patterns from hard edges of the optics on the optical path. We empirically consider that the uniformity is sufficient and does not affect the AGPMs performance.

4.7.1 Stability over time

The mirror and the bench as a whole are subject to slow mechanical drifts with time. The wavefront correction described in Section 5.2 can only be applied prior to the AGPM performance measurements. When the DM correction is no longer up to date, the wavefront quality will eventually decrease below a satisfying level. As a consequence, the rejection ratio will decrease too. In Fig. 4.9, the rejection ratio of an AGPM has been evaluated through time. The DM correction (see sect 5.2) was done just before time 0 and stayed the same through the entire experiment. The stability of the rejection ratio is required to accurately compare the different measurements on a given AGPM. If we aim at less than 5% error on the rejection ratio evaluation (Section 5.1.2), the measurements on the same mask have to be performed during a 2-hour interval after the aberrations minimization has been run to guarantee a stable environment.

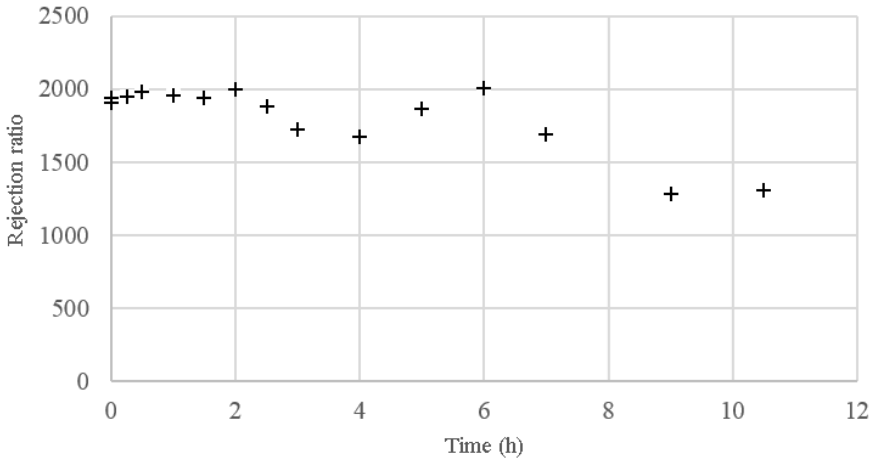

Figure 4.9: Rejection ratio evolution of an AGPM as a function of time with the same DM correction.

The deformable mirror uses a python interface and not the main LabVIEW interface (see Section 5). Using the python interface, the aberrations minimization routine is run and the DM shape is saved as a FITS file. When switching to the LabVIEW interface, the DM has to be reset and then the shape previously saved is applied. It was mandatory to evaluate the accuracy of this process. It was done using an average AGPM (L9r2). Different shapes of the deformable mirror were used (correcting different numbers of modes, see sect 6.5.1). The steps followed are:

1) a routine is run correcting a certain number of modes (shape number),
2) the deformable mirror shape is saved.

The steps 3) to 5) are repeated 5 times:

3) the shape is applied,
4) the rejection ratio is measured (see Sections 3.1 and 6.1),
5) the deformable mirror shape is set to 0.

Table 4.3: Rejection ratio measured for the same DM shape (shape set to 0 after each measurement).

Shape number	1	2	3	4	5	6	7
Rejection ratio	52	113	144	234	459	413	352
	53	114	148	238	465	411	350
	54	115	148	239	469	410	347
	55	116	147	242	469	411	348
	54	116	148	245	469	409	348
Standard deviation	1.020	1.166	1.549	3.720	3.919	1.327	1.789

As shown in Table 4.3, the deformable mirror presents an extremely good repeatability concerning the shape applied. In conclusion, switching from an interface to the other does not affect the wavefront correction and as a consequence, the rejection ratio achieved as long as it is done within a short period of time. Applying a DM shape saved more than a few hours before is useful as a starting point for a new aberrations minimization, the routine obtains the best DM shape faster than when it starts from actuators having their amplitude set at 0 (close to a flat shape of the DM surface).

4.8 VODCA alignment

Through the years of development, VODCA's layout has evolved. It has been aligned, dismantled and aligned again on several occasions. The complete alignment process is long and complex, and needs to be done carefully. Its accuracy will determine the optical quality of the bench and the best performance achievable by the AGPM. The DM can correct minor aberrations but will not compensate for a poor alignment. We describe in this section the most effective way to align VODCA in the different configurations available.

Due to the difficulty and safety issues, a red laser is preferred over an IR source to align VODCA. To assess the quality of a collimated beam we use a shearing interferometer and for a focal point we maximize the flux on the camera. The FLIR camera sensitivity range has its lower end slightly covering the red laser emission wavelength (632.8nm) but since the window material protecting the detector is not completely transparent in the visible, internal reflections create a blurry image. It is sufficient for a first approximation, then one can switch to an IR laser for more accuracy.

The first and most important step is to align the two main parabolas (f=609.6mm, ⌀=152.4mm). The distance between them is twice their focal length. A collimated beam sized at 20mm is aimed at one parabola at middle height and close to one of its side. The beam should be reflected twice on each parabolas, each time close

to one side of the parabola. A beam closer to the side of the parabolas has the advantage of creating more space (between the two collimated beams) and less chance of vignetting from the optics between the parabolas. The distance between both parabolas is fixed by making sure that the two outside beams between them are collimated. The parabolas mounts, which have two adjustable axes, are used for fine tuning. A simple way to verify the layout symmetry is to check the two beam focal points: one is created after the first reflection on parabola 1, the second created after a reflection on parabola 2 and one more on parabola 1. The focal points have to be indistinguishable.

The second step consists of placing the camera and fibered source. A flat mirror directs the beam to the FLIR camera, its position is set by maximizing the flux on the detector. Particular attention has to be paid to the fiber placement to avoid introducing aberrations. Before starting the alignment, the PSF position on the camera is noted and used as a reference. The fibered source has to produce a beam that follows the same path as the first collimated beam and as a consequence will produce a PSF at the same position on the detector. The AGPM mount z axis is aligned along the beam propagation axis. AGPM tests can be performed with fair quality (see Section 6.5) in this basic configuration. However, getting closer to the intrinsic limit of our masks requires to add a level of complexity to VODCA with the DM. Two flat mirrors direct the beam on the DM placed at 30cm away (extending the optical path), a greater distance is preferable to reduce the beam incidence angle on the DM. Since the DM defines the entrance pupil, the LS has to be in the same pupil plane. Spatial constraints on VODCA (LS vignetting) limit the available positions for the LS and as a consequence limit the distance between the flat mirrors and the DM. Following the same principle described above, adding the DM does not modify the optical path on the remaining part of the layout.

A "beam-shaping" is added to VODCA to facilitate filters and neutral densities manipulation. The SC laser is plugged on a built-in collimator (using an OAP), which is followed by a shutter and a filter wheel. Then the beam is injected in the fiber through an OAP on a 3-axis mount. Unwanted reflections on VODCA need to be given careful consideration as they can produce ghosts on the camera and interfere with the coronagraphic measurements.

5 SOFTWARE

5.1 LabVIEW interface

5.1.1 Developing a complete interface

The camera, the shutter and the AGPM mount actuators were chosen to be controlled simultaneously through LabVIEW. With a fully automatized interface, the AGPM performance assessment needs less manpower (no more than one person is needed). It is less time consuming and increases the repeatability and accuracy of the measurements (compared to the previous testbeds). LabVIEW is a data acquisition and interface creation software from National Instruments. The custom interface developed specially for VODCA is meant to be as user friendly as possible. The main sub-programs are designed for frame acquisition and background subtraction. Many options are available including the number of frames to be recorded, the background subtraction method (see Section 6.1), and the frame averaging option for the display (which slows down the refresh rate). The camera, the shutter and the actuators can be controlled individually with all the available features. On VODCA we do not aim at high frequency data acquisition and the interface has not been optimized for real time computation (such as closed loop wavefront control). As an output, the interface produces an average frame or a cube of frames in FITS format.

5.1.2 Centering routine

Description

The vortex coronagraph being very sensitive to centering errors, it is crucial to ensure that the phase mask is aligned with the beam since any deviation from this optimal position will result in leakage affecting the measured performance. Manual centering was a major source of uncertainty in the early performance assessment. Several alignments were required each time to minimize this error, introducing a non-negligible source of variability in the measurements. An automatic routine has been designed to fix this issue. It is less time-consuming and the centering achieved is more precise and reproducible.

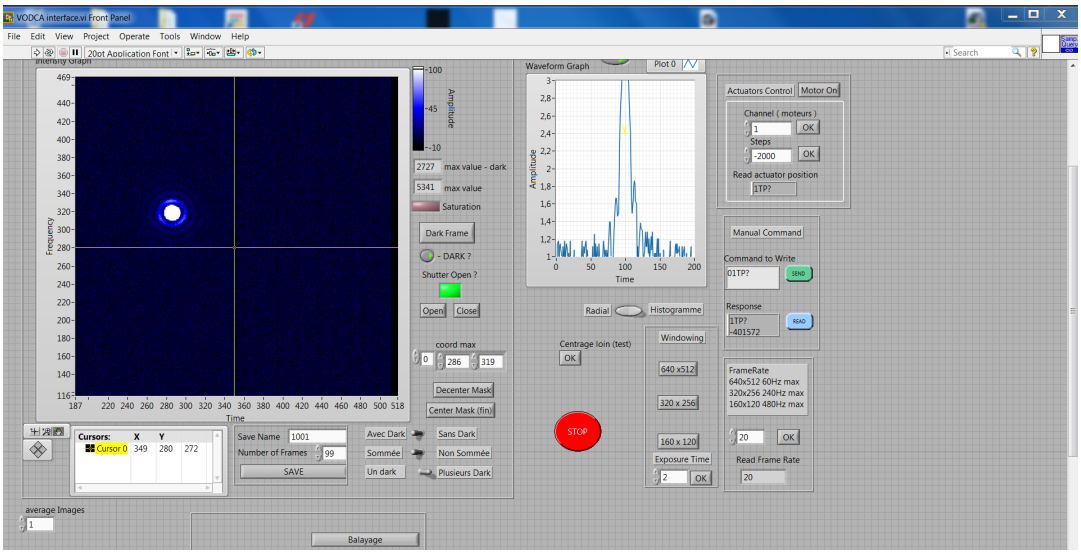

Figure 5.1: VODCA interface.

The criterion of minimization used is the flux integrated over a designated area around the PSF center. An option allows the routine to use another criterion: minimizing the highest flux of a pixel over the full image. The time saved with this less complex but less reliable criterion is negligible compared to the image acquisition. The protocol is a four-step process, using scans in the x and y axis (which are perpendicular to the optical path) with two different steps (large, 1 μm, and small, 0.25 μm) to find the optimal position and then proceed to put the vortex phase mask in this position. We first use a basic quadratic model (Huby et al., 2015) of the leakage to infer the vortex position based on a large-step grid, and then use smaller, incremental steps around the calculated minimum for an improved accuracy (Figure 5.3). Given the hysteresis inherent to the actuators, relying only on the calculated fit of the data leads to unacceptable errors on the positioning. A balance has to be found between the accuracy, the robustness, and the duration of the centering procedure. Accuracy and robustness are affected by turbulence, vibrations, and source fluctuations, while the bench stability limits the duration.

The most accurate routine (capability of finding the best position) would imply a weak robustness (rate of success for achieving the accuracy criteria) and/or an unacceptable running time (> 15min). The parameters selected (reasonable duration, i.e. < 5 min) result in a routine accurate and robust enough to achieve, on a serie of 17 successive alignments with a mean of 2023 in rejection ratio, a standard deviation of 116 (5.7%). The success rate is 94% (see Figure 5.2).

5.2 Python interface for aberrations correction

5.2.1 Description

A dedicated python interface (developed and integrated by Gilles Orban de Xivry) is in charge of the deformable mirror control. As mentioned earlier, VODCA features a DM with 97 actuators providing additional leverage in terms of aberrations control on the bench. Motivated by its flexibility and the many tools available in Python,

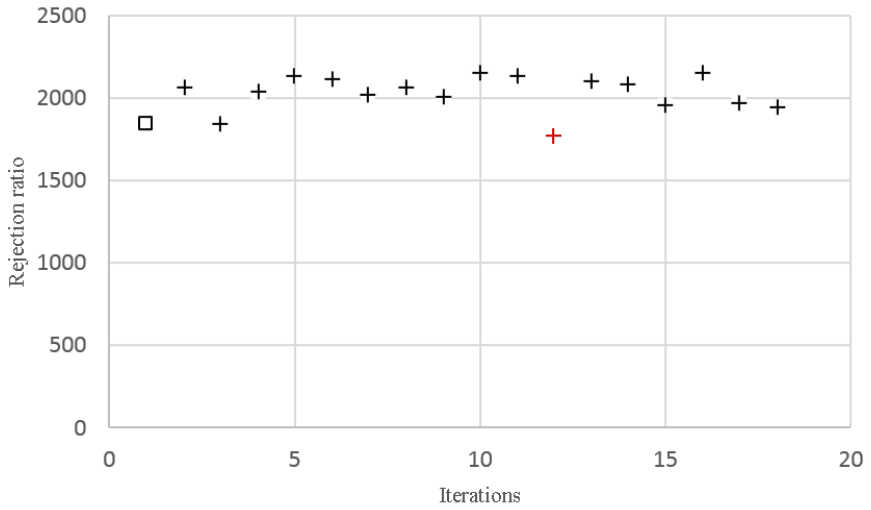

Figure 5.2: Rejection ratio after successive runs of the centering routine. The square is for the rejection ratio measured just after the aberrations minimization on the DM. The red cross is a failed attempt of the routine to successfully find the optimal position.

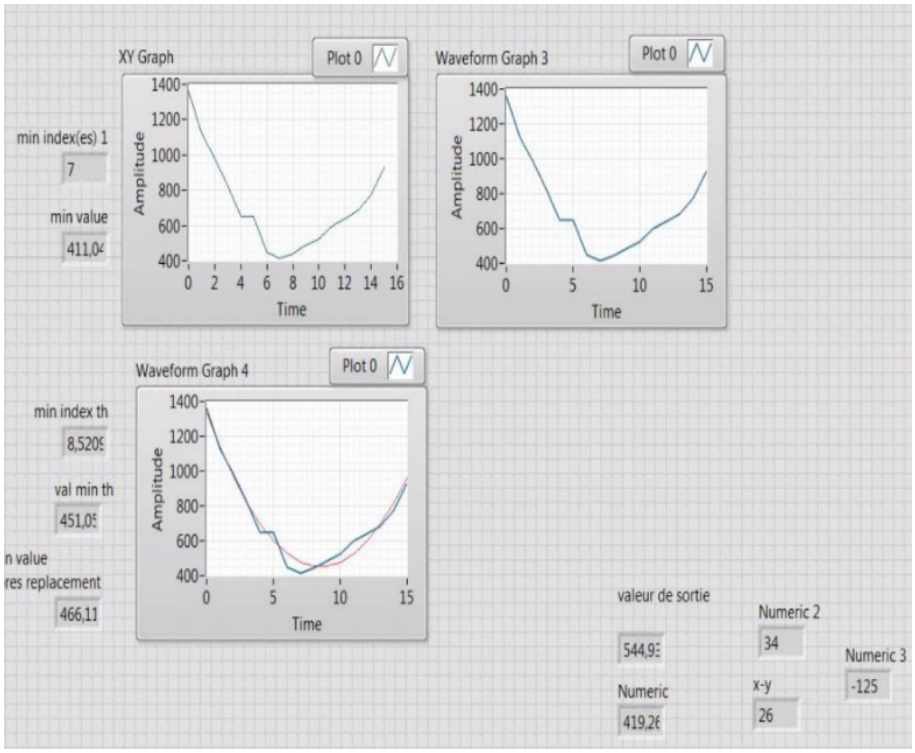

Figure 5.3: Example of indicators (hidden) of the centering routine interface running. They display the rejection ratio approximation for every step taken and the quadratic fit (lower graph).

we have implemented a multi-threaded software with a Qt interface to control and optimize the DM shape based on the FLIR camera images. The software allows

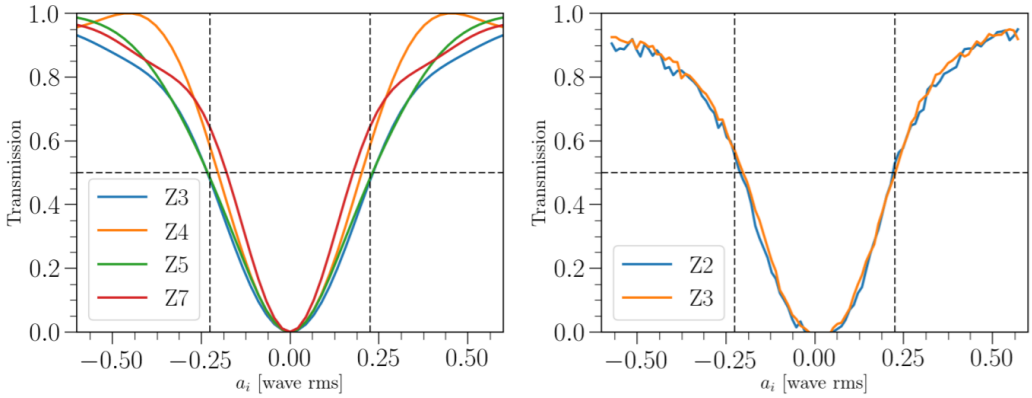

Figure 5.4: Flux leakage of the vortex coronagraph as a function of Zernike aberrations. (Left) Simulations for several Zernike (tilt, focus, astigmatism, coma) showing similar trend close to zero aberrations. (Right) Leakage measurements for tip-tilt in L-band on the VODCA bench with an AGPM (Orban de Xivry et al., 2017)

fast operations and online monitoring of the performance. We chose for VODCA a PSF sharpening techniques for aberrations minimization since it does not require additional hardware and can be easily implemented. A classical approach for PSF sharpening would be maximizing the Strehl ratio but the peak flux measurement is quite sensitive to vibrations or source fluctuations. On VODCA, we preferred a different approach, in which we implemented a simple and empirical technique to optimize the post-coronagraphic light rejection but still inspired from image sharpening techniques. Behind the vortex phase mask, the remaining flux (or leakage) is approximately quadratic with the amount of aberrations (see Figure 5.4). In these conditions, by minimizing the leakage we empirically reach the wavefront shape that maximizes the AGPM performance. This wavefront is expected to correspond to the best possible flatness, at least for low spatial frequencies (see Section 7.1 for more details).

While details can be found in Orban de Xivry et al. (2017), we summarize hereafter our procedure based on the post-coronagraphic PSFs:
1. selection of a metric and a minimization algorithm,
2. selection of a modal basis (e.g. Zernike or mirror modes), the coefficients of which are the free parameters of the optimization problem,
3. for each iteration, acquire and average a number of images, evaluate the metric and find the next solution of the modal basis.

Among the minimization algorithms available, we mostly used the Powell's method, which proved to be the fastest and most robust. The routine allows different metrics for PSF sharpening, the best results have been demonstrated by a minimization flux inside a radius of approximatively $7\lambda/D$ around the PSF center. It uses a set of directions and perfom one-dimensional minimization at a time. It does not rely on computing gradients. In our case, when optimizing a large set of parameters, those directions generally end up being each mode (Orban de Xivry et al., 2017). The DM operates on its own modal basis but can be switched to the commonly used Zernike base. This PSF sharpening technique for coronagraphy has brought some noticeable gain on measured raw contrast curves by improving wavefront control.

While the introduction of the DM and this optimization routine add some complexity to the bench and its operation, it ultimately improves the measurements and their repeatability. It is however expensive in terms of execution time requirement. Limitations and performance are discussed in Orban de Xivry et al. (2017). The same limitations to the optical quality of VODCA affect the aberrations minimization (vibrations, SNR, source behavior). An additional effect that has to be considered with this routine is the "creep effect". When a new shape is applied, a slow drift tends to occur relatively to the past shapes applied. A proper warm-up time (30 min) before operating the DM has proven to partially mitigate this effect.

5.2.2 Operation

Operating the python routine is a time-consuming process (see Section 7.2). The AGPM has to be centered beforehand (on-axis) in the best position while small deviations can be compensated by the DM (tip/tilt), they add additional stress to the DM and should be avoided. Starting the minimization routine requires a manual input of the PSF center position and the size of the box around the PSF center. The routine will only consider this area of the image. The minimization algorithm finds the investigated mode amplitude that minimizes the flux and then moves on to the next mode. Large improvement on a mode can affect the evaluation of the rest of the modes. In other words, to achieve the best flux minimization the routine has to go through each mode several times (2 is a minimum, 3 is usual). In theory, the DM can correct up to 97 modes, which results in an important amount of time for the minimization routine. Typically starting from a flat DM surface, it takes several hours to complete the routine with 97 modes.

The bench slowly drifts with time (Section 4.7.1), but starting a minimization from a previous DM shape still saves a significant amount of time. Since the amplitude of the low-orders is the most important, it is possible to switch to a "semi-manual" way of operating the routine to make it less time-consuming. In the case where the routine hits its allowed threshold in terms of amplitude for a given mode, it is wiser to stop the routine and fully correct the mode. It mostly happens when the routine does not start from a DM saved shape. Increasing the threshold is another option but has to be considered carefully not to damage the DM (and limit the "creep effect") or saturate the detector, since high amplitude aberrations drastically increase the flux of an on-axis AGPM. The python routine also allows to take pictures and plot PSFs if needed.

The experimental results and gain are detailed in Sections 6 and 7. The python interface is also used to investigate the influence of aberration on the AGPM performance (see Section 8).

5.2.3 Expected achievable flatness of the wavefront

ALPAO guarantees that the best wavefront flatness achievable in close loop is 12.22 nm RMS. No direct confirmation of this measurement was possible since no wavefront sensor or wavefront sensing technique is yet fully functional and available on VODCA. By investigating aberrations levels on VODCA and their effect on AGPM performance we estimate a more realistic 30 nm RMS wavefront error on VODCA (see Section 7.1).

PART III

Using the VODCA bench

6

PERFORMANCE MEASUREMENTS FOR L-BAND AGPMS

6.1 Procedure

The procedure is based on the rejection ratio evaluation (see Section 3.1). Before actually recording useful frames on VODCA, the first step is to ensure that the wavefront is as flat as possible. To do so, we used the routine described in Section 5.2 and corrected up to 97 modes with the DM. The shutter used for background subtraction is synchronized with the camera through the LabVIEW interface, to obtain background measurements and subtract them from the scientific frames in real time. Every single frame acquisition is thus systematically followed by an acquisition of a background frame. For each off- and on-axis image, we averaged 100 individual background-subtracted frames. On average, a complete acquisition (100 background-subtracted frames) takes 2 minutes. Although the shutter and the camera can operate at a much higher rate, the LabVIEW acquisition has to be slowed down to prevent de-synchronization between the shutter and the camera. De-synchronization can lead to different results from the inversion of data and background frames to "half frames" recorded while the shutter closes/opens. Operating at this speed, we experience no dropped frame. Robustness is a crucial feature for the frame acquisition since (i) the measurements have to be done in a limited time and (ii) the control for missed synchronization is not straightforward and would add unnecessary complexity to the process. Although less time consuming, one single background measurement for a whole sequence of acquisitions proved to be insufficient to capture background fluctuations.

6.1.1 Number of frames averaged

As stated in Section 4 and more detailed in sect 6.5, various effects have the potential to cause variability in the measurements. Averaging frames minimizes the variability issue. Using a large number of averaged frames leads to negligible difference between two data sets recorded in the same conditions, thus reducing the uncertainty of a single data set. Since the bench cannot be considered as stable for a long

period of time (see sect 4.7.1), the number of averaged frames has to be limited.

To evaluate the influence of the number of frames we used the following protocol: 4000 frames are recorded, and split into 20 cubes. For each cube, n frames are averaged. The averaged frame is compared to the averaged frame for the other 19 cubes. The standard deviation is computed. n varies from 1 to 200. On-axis (attenuated PSF) and off-axis (non-attenuated PSF) were tested.

In this experiment only, the 4000 images were recorded without background subtraction in-between to allow for a more homogenous data set and reduce the duration of the recording. The flux on the camera is high enough not to be affected by a poorer background subtraction.

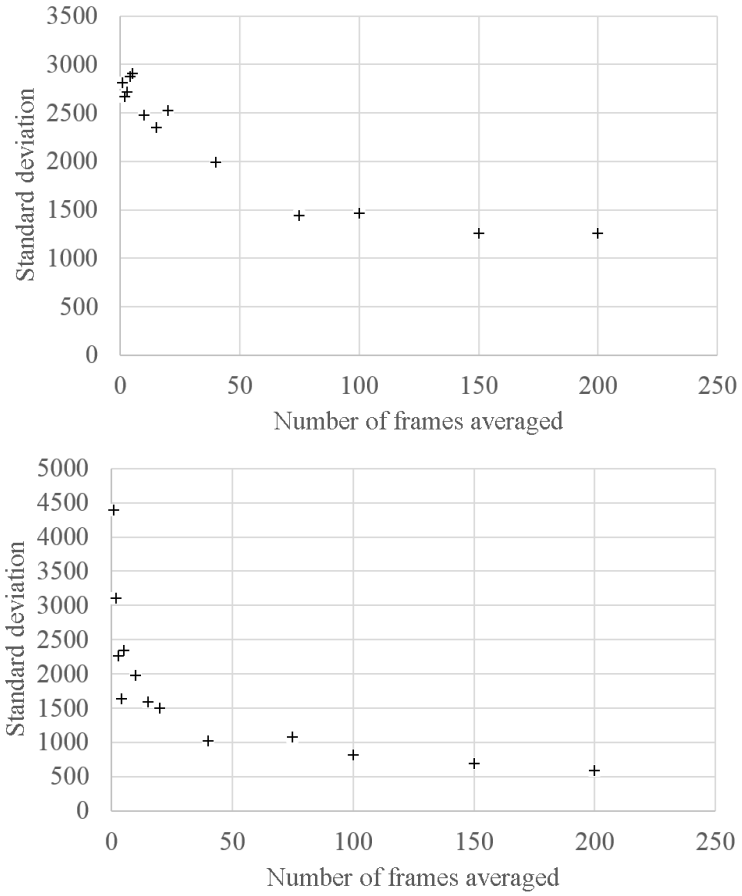

Figure 6.1: Effect of frames averaging on on- (top) and off- (bottom) axis PSF.

Mechanical vibrations affect the PSF position in both on- and off-axis cases, but has a stronger impact on on-axis PSFs. Not only its position but its intensity is affected due to the nulling effect being sensitive to positioning. The consequence is a standard deviation decreasing as expected at a lower rate for the on-axis PSF as shown in Figure 6.1. Based on these results, we decided to average 100 frames for both on- and off-axis PSFs, since it is a good trade-off between small dispersion (especially for on-axis-PSF) and time efficiency.

6.2 Measured performance

In table 6.1 are presented the best rejection ratios measured for all AGPMs that have been tested on VODCA.

Table 6.1: Best AGPM rejection ratio measured on VODCA with L-band filters and in the M-band (monochromatic source). The accuracy of the centering routine ($\pm$1-σ, Section 3.3) defines the errors on the rejection.

	L-BBF	L-NBF1	L-NBF2	L-NBF3	4.6 μm
AGPM-L4	566 $\pm$32	292 $\pm$17	669 $\pm$38	789 $\pm$45	70 $\pm$4
AGPM-L5	1501 $\pm$86	588 $\pm$34	2092 $\pm$119	1715 $\pm$98	48 $\pm$3
AGPM-L8	168 $\pm$10	94 $\pm$5	64 $\pm$4	32 $\pm$2	18 $\pm$1
AGPM-L9r2	852 $\pm$49	337 $\pm$19	924 $\pm$53	830 $\pm$47	141 $\pm$8
AGPM-L11r	2404 $\pm$137	3213 $\pm$183	1683 $\pm$96	543 $\pm$31	75 $\pm$4
AGPM-L12r	84 $\pm$5	86 $\pm$5	87 $\pm$5	146 $\pm$8	1773 $\pm$95
AGPM-L13r	176 $\pm$10	92 $\pm$5	207 $\pm$12	483 $\pm$28	134 $\pm$7
AGPM-L14	864 $\pm$49	258 $\pm$15	995 $\pm$57	802 $\pm$46	55 $\pm$3
AGPM-L15	1430 $\pm$82	717 $\pm$41	1378 $\pm$79	1448 $\pm$83	50 $\pm$3

The L-band AGPM were tested in the L band with the SC laser source in the broadband and narrow band filters, as well as in the M-band using the 4.6 μm laser source, to check if they meet the requirements for scientific operation on a ground-based 10-m class telescope. The results are compiled in Table 6.1, where AGPMs identified with a "r" have been re-etched to improve their original coronagraphic performance. The re-etching consists mostly in tuning the etch depth. In the case of AGPM-L9r2, this procedure was done twice (see Section 6.4.1 for details).

6.3 Transmission

Each AGPM has an Anti-Reflective Grating (ARG, see Section 2.2.3) etched on the backside of the component to reduce internal reflection inside the phase mask. Transmission measurements of AGPMs aim to confirm the ARG simulations and its manufacturing process. Using the L-BBF filter, an off-axis PSF image is compared to the reference image without the mask in the optical train, to compute the transmission of the AGPM. The same procedure was repeated with the 4.6μm laser source. In Table 6.2, all the AGPMs show a transmission in the 82% to 85% range at L band, close to our expectations. The measured transmission significantly decreases in the M-band, due to increased phonon absorption around 4.6 μm.

6.4 Comparison with previous results

Characterizing the same AGPM on different benches provides a tool to evaluate the optical quality of the bench. Some AGPMs have been tested in the past on the YACADIRE test bench at the Paris Observatory. The rejection ratios measured with this bench are globally lower than those measured on VODCA (see 6.3). The protocol for data acquisition was the same, however no automated centering routine nor DM were available on YACADIRE. Reducing aberrations through better alignment and better wavefront correction is key to reach the intrinsic limit of the AGPM

Table 6.2: AGPM transmission in the L-BBF filter and at 4.6 μm. Error bars are included only for AGPMs that have been measured several times. AGPM-L13 has not been evaluated in the L band due to its limited availability.

	L-BBF	4.6 μm
AGPM-L4	82%	66%
AGPM-L5	85.4% $\pm$0.1	61%
AGPM-L8	82.9% $\pm$0.4	62%
AGPM-L9r2	84.7% $\pm$0.9	70% $\pm$3
AGPM-L11r	83.7% $\pm$0.1	58% $\pm$2
AGPM-L12r	85% $\pm$0.7	68.5% $\pm$2.5
AGPM-L13		64%
AGPM-L14	83%	65%
AGPM-L15	83.5% $\pm$0.5	66% $\pm$1

in terms of rejection ratio. Other factors such as signal-to-noise ratio and accurate mask centering were also taken into account while designing and building VODCA. It confirms the overall better optical quality of VODCA. Unfortunately, no in-depth study was performed to evaluate with precision the error budget of the measured rejection ratios on YACADIRE. The masks have been measured repeatedly and the dispersion of the measurements led us to estimate typical statistical errors around 15%. To provide a fairer comparison between the VODCA and YACADIRE results, we also quote the rejection ratios measured on VODCA without wavefront control. The quality of these measurements is reduced compared to the case with wavefront control, as discussed below (Section 7.1), but it is still significantly higher than on YACADIRE thanks to the more optimal design and to the automatic centering procedure.

Table 6.3: Comparison between the best results with the L-BBF filter on VODCA and YACADIRE. AGPM L4 and L14 have not been tested without DM due to their limited availability.

	VODCA (with DM)	VODCA (without DM)	YACADIRE
AGPM-L4	566 $\pm$32		500 $\pm$75
AGPM-L5	1501 $\pm$86	950 $\pm$54	620 $\pm$93
AGPM-L8	168 $\pm$10	52 $\pm$3	60 $\pm$9
AGPM-L9r2	852 $\pm$49	536 $\pm$31	397 $\pm$60
AGPM-L11r	2404 $\pm$137	1300 $\pm$74	984 $\pm$148
AGPM-L14	864 $\pm$49		370 $\pm$56
AGPM-L15	1430 $\pm$82	1251 $\pm$71	628 $\pm$94

6.4.1 Re-etching

AGPMs are not perfectly achromatic. They guarantee a minimum rejection ratio for a broad spectrum (corresponding to an infrared spectral band) but across this wavelength range, the performance varies. It is directly related to the physical characteristics of the mask. On VODCA, we use narrow band filters. They allow us to explore the rejection ratio as a function of wavelength. These measurements can then be compared to Rigorous Coupled-Wave Analysis (RCWA) to infer the corresponding grating parameters. This is much needed because of the lack of non-destructive

metrological method for the gratings evaluation. Most of the time during AGPM manufacturing, a test sample is also etched following the same steps for the purpose of being cracked and have its grating parameters (depth, filling factor and sidewall angle) measured. It only provides a rough estimation concerning the actual masks since the etching process is not perfectly uniform. Having access to the gratings parameters of an AGPM help us to confirm the validity of the manufacturing process and improve it if necessary. In the case of some AGPMs, after optical evaluation and RCWA simulations it was found that a better rejection ratio could be reached by changing the grating depth. Re-etching was done on components which showed a low rejection ratio.

The re-etching process is briefly summarized below:
(i) if the depth of the grating has to be reduced, the AGPM is filled with resist then goes through a step of plasma etching. The resist on top of the mask is etched quickly while inside the grooves it will protect the bottom much longer,
(ii) in the opposite case, we sputter an Al film that is thicker on the top than at the bottom. The next step of etching will dig deeper in the trenches producing a grating with a larger depth.

Re-etching is actually a more complex process that is described in details in Vargas Catalán et al. (2016).

Example

Several AGPMs have been re-etched for operations in K and L bands (Table 6.4). The performance noticeably improved. Significant examples include AGPM-L9r2 and L11: with rejection ratios originally below 100 to respectively 400 and 900 in L-band. The rejection ratios are all from YACADIRE to allow for a fair comparison since the masks have only been tested on this bench before re-etching.

Table 6.4: Rejection ratios in the broadband L filter for the optimized AGPMs (Vargas Catalán et al., 2016).

	Tuning process	R before tuning	Δh (μm)	R after tuning
AGPM-L9	Al deposition	30	+0.40	100
AGPM-L9r2	Al deposition	100	+0.38	400
AGPM-L11r	Resist filling	70	-0.32	910
AGPM-L12r	Resist filling	70	-0.42	470
AGPM-L13r	Resist filling	110	-0.29	190

We experimentally demonstrated the benefit of re-etching and a better understanding of the etching process. It allowed us to reduce the waste of the manufacturing process and produce more effectively high performance AGPMs. Re-etching proved to be a powerful tool in the development of high rejection ratio AGPMs. Several low performance masks have been successfully turned into high performance masks. Etching new masks is a long and costly process but it increases significantly the success rate of AGPM manufacturing.

7

VODCA OPTICAL QUALITY AND LIMITATIONS

7.1 Influence of wavefront correction

In the case of broadband measurements, an AGPM will never produce a perfect cancellation of the star light due to chromatic errors in the π phase shift induced between the two orthogonal polarizations by the subwavelength grating. The textbook effect of chromatic errors is to produce a scaled-down version of the non-coronagraphic PSF. This is illustrated in Fig. 7.1, where the VODCA bench was operated without DM, using one of the available AGPM (AGPM-L11r). The coronagraphic PSF is slightly broadened compared to the off-axis PSF, but corresponds otherwise rather well to the expected, scaled-down version of the off-axis PSF. The broadening of the central part of the PSF points towards the presence of low-order aberrations, while very little high order aberrations seem to affect the contrast curve at larger separations.

The same measurements were then repeated after inserting the DM in the optical train and optimizing its shape to minimize the rejection ratio, as described in Section 5.2. In Fig. 7.2 are displayed the same measurements (same AGPM) as in Fig. 7.1, with aberrations control by the deformable mirror. Two main differences can be noted with respect to Fig. 7.1: a higher rejection ratio (2400 instead of 1300), but also a higher star light level beyond 1.0 λ/D. The higher rejection ratio suggests that the intrinsic limit of the AGPM in terms of star light rejection was not reached in the first measurement without DM, while the increased residuals at larger separation point towards increased aberrations at the corresponding spatial frequencies, which introduce non-corrected speckles responsible for the plateau-shape of the attenuated PSF noticeable after 1.5 λ/D. Since it features 97 actuators, the DM should in principle control the wavefront up to 5 λ/D. The level of aberrations in the 1.5-5λ/D range suggests that either our optimization strategy is not working well for these spatial frequencies, or that the DM intrinsically introduces aberrations at these frequencies.

We have simulated the influence of wavefront errors, evenly distributed between the first 100 Zernike modes as described in Table 7.1. The plateau observed in Figure 7.3 at a level of about 4×10^{-4} in the coronagraphic PSF can then be reproduced with a total wavefront error of 30 nm rms, which means an rms error of 3 nm for each individual Zernike mode. The level of the plateau is roughly proportional to rms

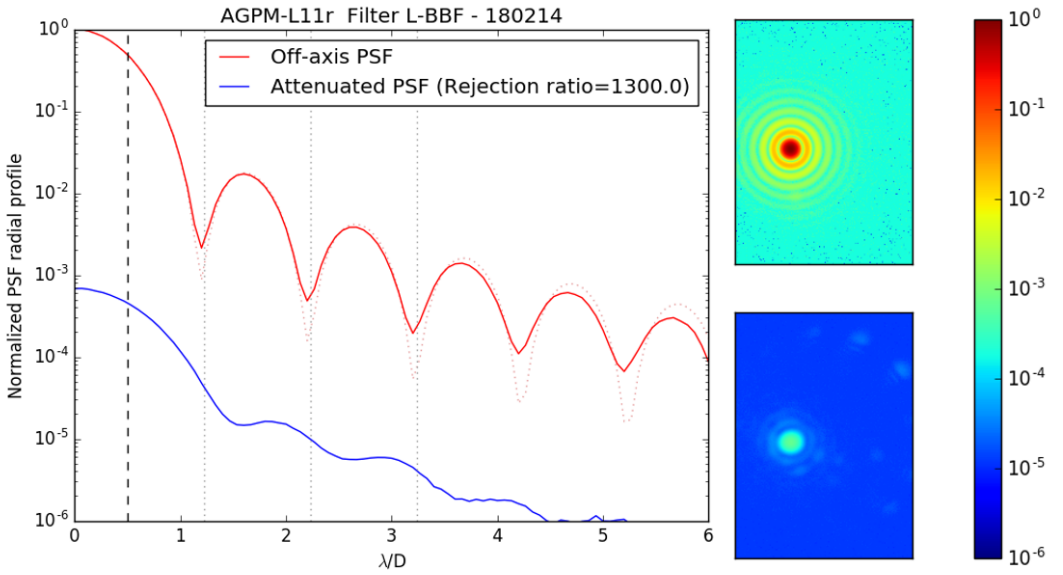

Figure 7.1: Left: Radial profiles for the coronagraphic (blue) and non-coronagraphic (red) PSFs, using the same undersized Lyot stop. The dashed vertical line represents the area over which the flux is integrated to calculate the rejection ratio. The dashed red lines correspond to the theoretical Airy pattern. Right: Illustration of the off-axis (top) and on-axis (bottom) PSFs.

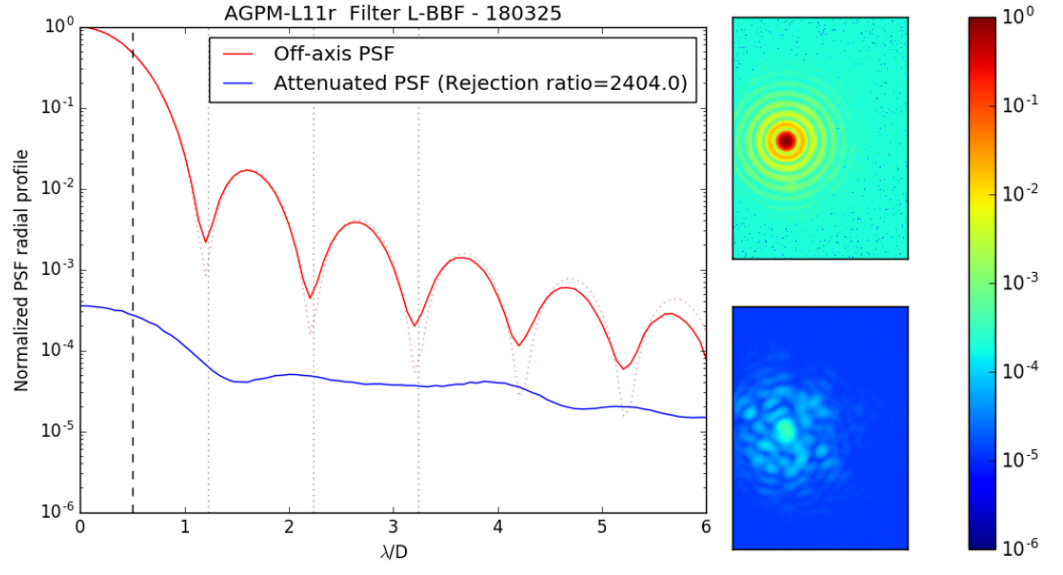

Figure 7.2: Same as Fig 7.1 when the DM is introduced in VODCA and optimized to improve the rejection ratio.

errors on each mode, while the spatial extent of the plateau depends on the number of modes included.

Table 7.1: Simulation parameters

Fraction Lyot stop	80%
Central obscuration	None
Intrinsic rejection ratio	2404
Wavelength (μm)	3.75
Number of Zernike modes	100
Wavefront error rms (nm)	30

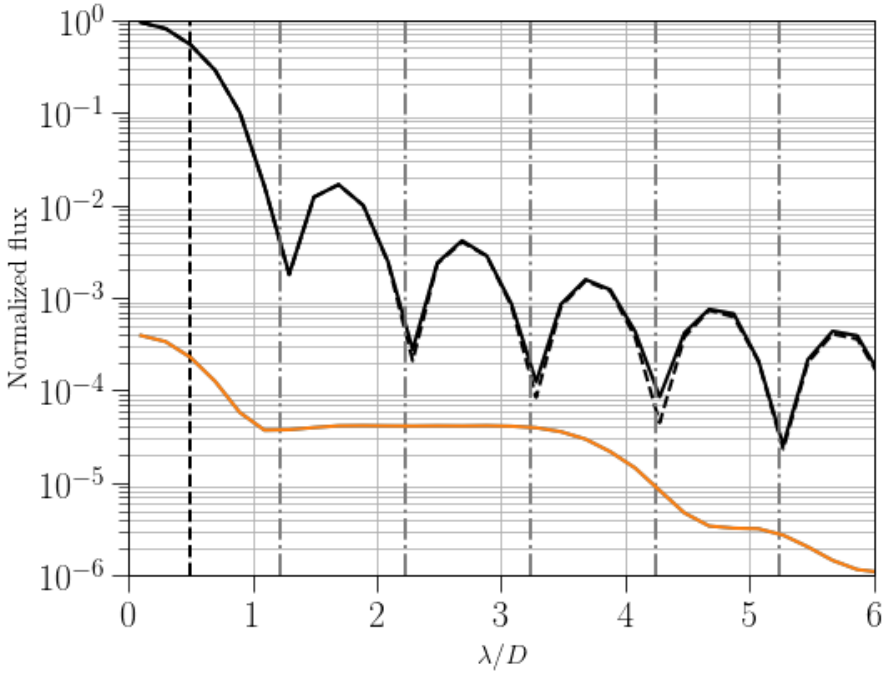

Figure 7.3: Simulated off-axis (black) and coronagraphic (orange) PSFs using the parameters of Table 7.1.

From these measurements and simulations, we conclude that using wavefront control (as described in Section 5.2) significantly reduces the power in the lowest aberration orders, but also increases the aberration level in higher order modes within the DM control region, and thereby reduces performance beyond about 1 λ/D. Without DM, the bench presents a higher level of low-order aberrations (i.e., lower attenuation on the PSF core) but a lower level of high order aberrations since the radial profile intensity decreases as expected with angular separation (as in aberration-free simulations). We note that the estimated level of aberrations in presence of the DM (30 nm rms spread onto 100 modes) is significantly larger than the expected best flat for the DM (=12.22 nm rms measured by the manufacturer). This suggests that a better correction would be possible by implementing a better wavefront control strategy, based e.g. on a bona-fide infrared wavefront sensor.

7.2 Effect of time-limited wavefront control on rejection ratio

The aberrations minimization is a time consuming step in the AGPM performance measurement (see Section 5.2). Correcting fewer modes on the deformable mirror reduces its execution time. In this section we investigate the influence of the number of modes corrected on the rejection ratio achieved. To do so, all the available AGPMs were tested since they present various maximum rejection ratios (see Section 6.2). For each one of them, an aberration minimization is run for a defined number of modes and the rejection ratio is then computed. The process is repeated for every 10 modes until 70. The results are displayed in Fig 7.4.

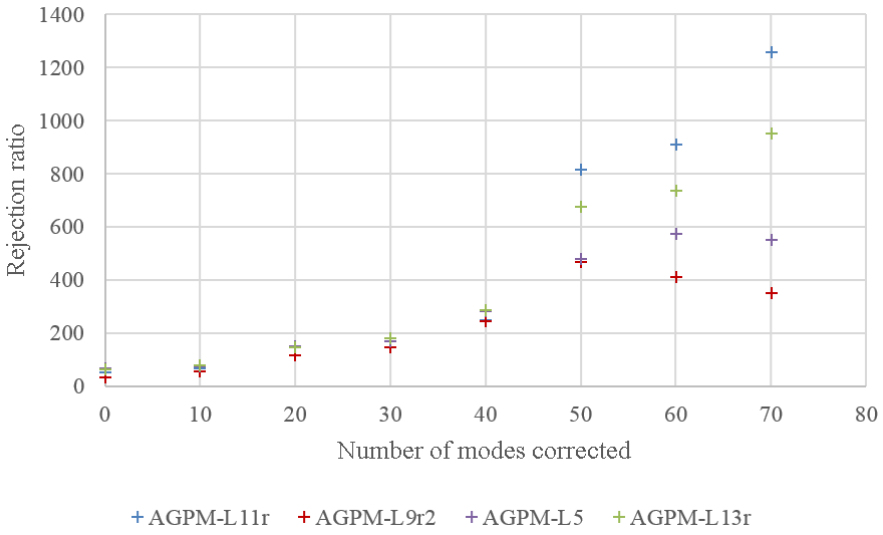

Figure 7.4: Rejection ratio reached when the aberrations minimization routine corrects the first 0 to 70 modes. The measurements have been performed for the 4 AGPMs available at that time.

All the AGPMs tested show similar rejection ratios for a number of modes lower than 40. In this regime, the wavefront quality is completely limiting the performance. Significant differences appear when more than 40 modes are corrected. High performance AGPMs increase their rejection ratio when more modes are corrected (verified for any number of modes). The other AGPMs follow the same behavior until their performance reaches a plateau, where increasing the number of modes does not increase any longer their rejection ratio. The plateau depends on the AGPM quality. Their rejection ratio can decrease after it has reached its maximum. Trying to correct high orders when the AGPM is the limiting factor can be counter-productive since the aberrations correction routine is based on flux minimization. If the flux is already minimal for a specific mask, correcting higher order modes can only lead to errors and a decreased performance. The number of modes corrected has to be adjusted in a step-by-step process but can be usually limited to typically 70 modes. Reducing the number of modes corrected below 70 affects the significantly the performance and cannot be considered as a time-saving protocol.

Considering Figure 7.4, three different regimes can be defined if we assume that the wavefront error decreases with the number of modes corrected:

1. for highly aberrated wavefronts, the error appears to strictly define the highest rejection ratio for any AGPM,

2. in the case of moderate aberrations, the rejection ratio achievable depends on two factors, the wavefront error and the intrinsic performance of the AGPM considered,

3. the last case corresponds to minimally aberrated wavefronts where the physical parameters and/or defects of the mask become the limiting factor of the performance, in this case the wavefront error is not correlated to the AGPM rejection ratio.

In the future, wavefront sensing techniques or a wavefront sensor will be available on VODCA. Measuring accurately the wavefront error at different stages of the correction and the rejection ratios of several AGPMs will allow to conclude on the relation between wavefront error, modes corrected and rejection ratio achievable for AGPMs.

7.3 Optical quality

Vibrations and turbulence are expected to affect the rejection ratios measured on VODCA. In order to evaluate their influence, we measured the motion of the non-coronagraphic PSF on the detector. A peak-to-valley (PtV) motion ≈0.4 pixel (=6 μm) was measured, which corresponds to about 0.035 λ/D at L band. Assuming that the same level of vibration affects the beam at the intermediate focus where the AGPM is located (a pessimistic assumption as the detector is the main source of vibration on the bench), this would lead to an additional stellar leakage of only about 2×10^{-4}, which is negligible compared to the intrinsic performance of the AGPM to be tested.
Beyond pointing jitter, charge-2 vortex phase masks like the AGPMs are known to be sensitive to low order aberrations in general. Simulations of a perfect AGPM in L-band with an 80% Lyot stop (as in VODCA) and no central obstruction have been carried out to estimate the maximum aberration level that can be tolerated in order to measure rejection ratios greater than 10^3. The analysis was performed independently for the main low order Zernike modes Z2 (tip), Z4 (focus), Z5 (astigmatism), Z7 (coma), Z9 (trefoil). For each of these modes, we varied the wavefront rms and simulated off- and on-axis PSFs. For each couple of PSFs, we computed the rejection ratio. The results are illustrated in Fig 7.5. The aberration level where the rejection ratio reaches 10^3 (resp. 2×10^3) is listed for each mode in Table 7.2.

Our simulations show that the rejection ratio is particularly sensitive to astigmatism, while quite resilient to focus. This is because the additional stellar leakage induced by focus errors mostly affects the first Airy ring. The rejection ratio, which is computed on the PSF core, is therefore not as affected as for the other aberrations, but the performance still significantly decreases in the first Airy ring and beyond (see Table 7.2).

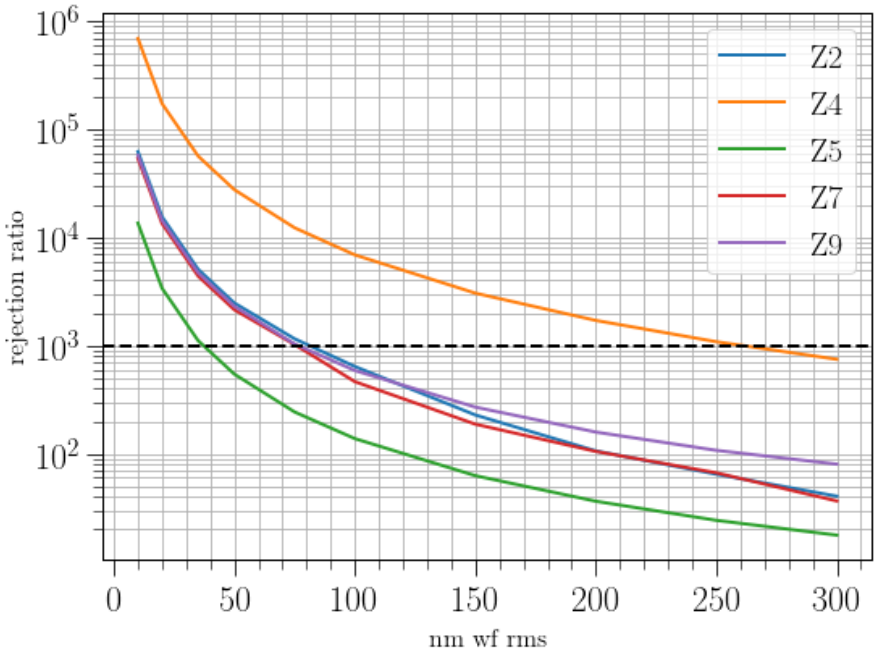

Figure 7.5: Theoretical rejection ratio computed as a function of the amplitude of five low order aberrations (Z2: tip, Z4: focus, Z5: astigmatism, Z6: coma, Z7: trefoil).

Table 7.2: Aberrations level limiting the rejection ratio (RR) to 10^3 and 2×10^3.

Mode	Wavefront rms (nm)	
	RR = 10^3	RR = 2×10^3
Z2	81	26
Z4	260	84
Z5	37	12
Z7	76	24
Z9	76	25

7.4 Conclusion on VODCA's measurement precision

It has always been an challenge to distinguish what actually limits the measured performance between the bench and the intrinsic potential of the AGPM (if not both). The case of AGPM-L11r has been key to largely solve the issue. This particular AGPM shows an outstanding rejection ratio of 2400 (resp. 3200) in broad band (resp. narrow band). Comparing these performances with the simulations, we infer the minimum optical quality of our bench. We conclude that the aberrations in the lower order modes are not larger than the values given in the right-most column of Table 7.2. Actually, because the previous analysis pertains to each mode taken separately, the aberrations are most probably much smaller than these limits, and probably of the order of 3 nm rms per mode, as discussed in Section 7.1.

AGPM-L11r has its rejection ratios close to the RCWA simulations, which predict the best rejection ratio to be >2500 over the L-band with a peak >3500 at a specific

wavelength (Vargas Catalán et al., 2016). We safely assume that these AGPM grating parameters are not strictly optimal and still partly account for the loss of performance compared to the simulations. We conclude that we reached our goal in terms of optical quality in the development of the VODCA bench and that it is able to deliver accurate measurements of AGPMs close to their theoretical limits. We are confident to provide AGPM rejection ratio measurements with less than 5% error (see Section 5.1.2).

The VODCA bench is most probably capable of measuring rejection ratios even larger than 3000, although since we are close to the theoretical limit of the AGPMs in this configuration, it is hard to evaluate the exact bench limitation in the absence of an actual infrared wavefront sensor.

8

INFLUENCE OF ABERRATIONS

8.1 Introduction and test protocol

The last section highlighted the influence of the wavefront quality on the measured rejection ratio. There, we detail the influence of specific optical aberrations on the AGPM performance. We focus on low order modes since they present the higher amplitude and affect the most the rejection ratio.

In Section 3.2.1, the tip, tilt and focus influences on the AGPM performance were measured for the first time using the IRCT testbench at NASA/JPL. Tip/tilt and focus were the only low order aberrations that we could create by physically moving the mask. Now that we have access to a deformable mirror on the VODCA bench, the aberrations will be introduced through the deformable mirror using Zernike modes. These polynomials form an orthogonal base, commonly used to characterize wavefront distortion. The low-order Zernike modes are associated with classical Seidel optical aberrations. Considering a circular aperture with a normalized diameter, each point can be defined in polar coordinates by its angle ϕ and its radial distance ρ from the center which verify :

$$0 \leq \rho \leq 1, \tag{8.1}$$
$$0 \leq \phi < 2\pi, \tag{8.2}$$

Zernike polynomials are defined, in the case of the even ones by

$$Z_n^m(\rho, \phi) = R_n^m(\rho) \cos(m\phi) \tag{8.3}$$

and in the case of the odd ones by

$$Z_n^{-m}(\rho, \phi) = R_n^m(\rho) \sin(m\phi), \tag{8.4}$$

with m and n being positive integers and $n \geq m$ and

$$R_n^m(\rho) = \sum_{k=0}^{\frac{n-m}{2}} \frac{(-1)^k (n-k)!}{k!(\frac{n+m}{2}-k)!(\frac{n-m}{2}-k)!} \rho^{n-2k} \qquad \text{if } n-m \text{ even}, \tag{8.5}$$

$$R_n^m(\rho) = 0 \qquad \text{if } n-m \text{ odd}, \tag{8.6}$$

The aberrations seen by the AGPM will be the sum of the aberrations introduced by the DM and of the ones already present on the bench. Since no wavefront sensing measurement is available this second factor needs to be reduced as much as possible. The bench is set in the optimal conditions for rejection ratio evaluation. The DM script is run to provide a wavefront with the least amount of aberrations possible. As detailed in part 5.2, the DM operates in its own modal basis for better results. It means that it has to be switched to a Zernike basis before continuing the process. The DM shape is saved as a reference. The ALPAO deformable mirror has a built-in functionality allowing it to introduce Zernike modes with a certain amplitude. As a consequence any amplitude change on the actuators to create a Zernike mode will be applied on top of the reference shape. The actual amount of the Zernike mode introduced on the bench was verified. We used the tip and tilt modes for this measurement and confirm that there is a direct relationship between the RMS phase across the pupil associated to tip/tilt and displacement in the focal plane Δx:

$$\Delta x = 4\, f\# \, tilt_{RMS}. \tag{8.7}$$

The infrared detector has 15μm pixels. By measuring the PSF movement in pixels units on the camera, we obtain the shift in μm, which is plotted against the level of tilt introduced on the DM in Figure 8.1.

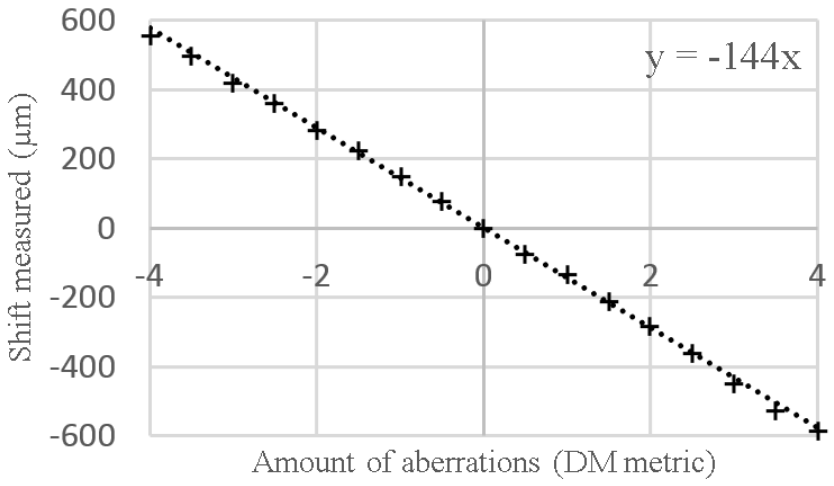

Figure 8.1: Shift measured of the PSF when tilt is applied from the DM.

The slope of the curve (144, see Fig 8.1) was used in equation 8.7 for the variable Δx. Taking into account of the $f\#$ of 45, it was deduced that the amplitude introduced according to the ALPAO software metric had to be corrected by a factor of 0.8 to estimate the real amplitude on tip/tilt introduced on the bench. The same ratio was applied for the higher orders. Assuming that the DM amplitude calibration is the same for all the modes considered here. Zernike modes corresponding to tip (or tilt),

focus, astigmatism and coma are introduced and the rejection ratio measured for amplitude up to 0.32μm RMS. Introducing more aberrations is counter-productive because (i) it could potentially be a threat to the safety of the DM membrane and actuators and (ii) the rejection ratio will be too low (<20) to add any significant value to the experiment. The experimental results are then compared to the simulations presented in Section 7.3. The main limitation of such a comparison is that our experimental results take into account only the aberrations introduced after running the aberrations minimization routine. In this experiment, the residual non-corrected aberrations are ignored (due to the lack of WFS) but still affect the rejection ratio. In Section 7.3, we estimated that these residual aberrations are not negligible and represents a wavefront error level around 30nm RMS spread over 100 modes. In the lower range of introduced aberrations, the actual aberrations on the bench are dominated by the residual ones. In this case, we expect that our experimental results diverge from the simulations. Moving to the higher range of introduced aberrations, the proportion of residual aberrations in the total aberrations of the bench will decrease. We expect that our experimental results will better fit the simulations in this region.

8.2 Results

8.2.1 Tip/tilt

Tip and tilt quantify the position along the x and y axes (considering z as the propagation axis). Quick variation in tip and tilt is called pointing jitter. It is a major concern in terms of rejection ratio achievable. On large ground-based telescopes it is usually corrected by a dedicated adaptive optics system and tracking/pointing technique. There, we rather study the influence of static non-common path tip and tilt. On VODCA, several steps ensure a minimization of the tip/tilt. First a manual centering of the mask, then an automatized routine. The DM minimization routine also reduces the tip and tilt aberrations.

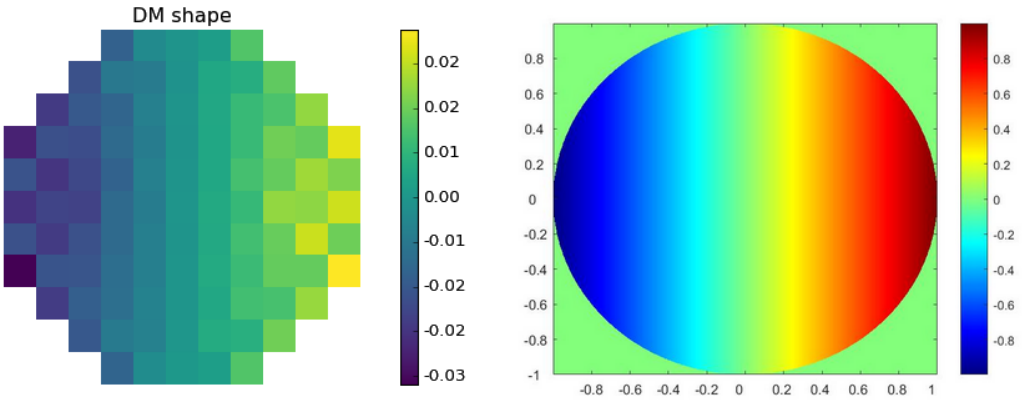

Figure 8.2: Left: Deformable mirror shape. Right : Tilt simulation.

In Figure 8.2, the injected mode (tilt in this case) is applied to the DM, its shape is shown on the left panel. The right panel displays the tilt simulation following the expression of tilt in Zernike polynomial :

$$Z_1^1 = \rho \cos(\phi). \tag{8.8}$$

On the left panel of Figure 8.2 is the zernike polynomial projected on the 11x11 actuators deformable mirror.

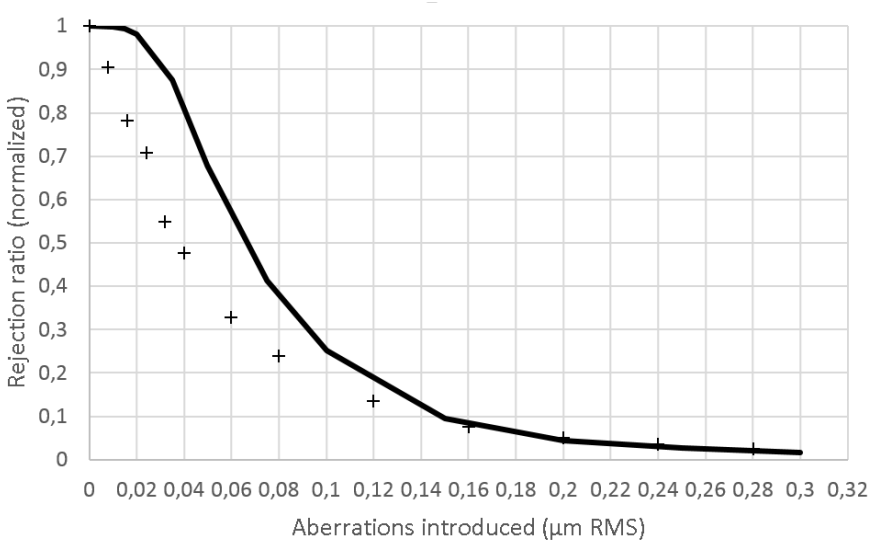

Figure 8.3: Influence of tip and tilt on the rejection ratio. Cross marks: experimental results, line: simulation.

In Fig. 8.3, as expected the rejection ratio decreases rapidly when tip is introduced. The experimental results follow the trend but do not reproduce the exact shape of the simulation especially in the <0.02μm region. This is due to the residual aberration level on VODCA. The results get closer to the simulation for aberrations >0.16μm.

8.2.2 Focus

Focus (or defocus) refers to a shift between the optimal position (at a focal point of the system) and the actual position of the object or optics along the propagation axis. In our case it can be introduced by several optics on VODCA. The fiber output after the beam shaping part and the AGPM have to be placed at the focal point to minimize defocus. If the detector is not at the focal plane, it does not impact directly the AGPM performance but it undermines the information quality we get from the PSF shape and affects the data processing. On VODCA, the correct alignment between the fiber output and the detector is done manually by maximizing the flux on the PSF peak and/or minimizing the flux at the first zero of the Airy disk describing the PSF. The AGPM is positioned manually along the propagation axis by maximizing the rejection ratio (assuming the best rejection ratio is achieved at the best focus). Finally the DM minimization routine reduces the remaining defocus aberration.

On the right panel of Figure 8.4 is displayed the simulation following the expression of focus in Zernike polynomial :

$$Z_0^1 = 2\rho^2 - 1. \tag{8.9}$$

On the left panel of Figure 8.4 is the Zernike polynomial projected on the 11x11 actuators deformable mirror.

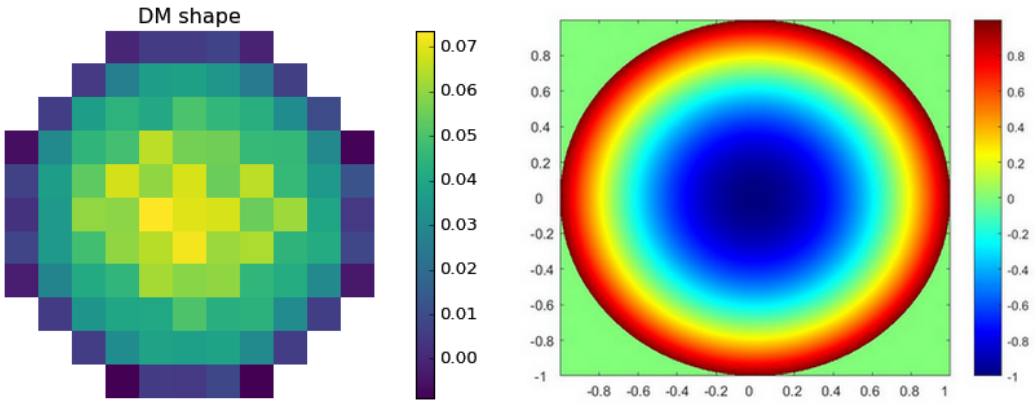

Figure 8.4: Left: Deformable mirror shape. Right : Focus simulation.

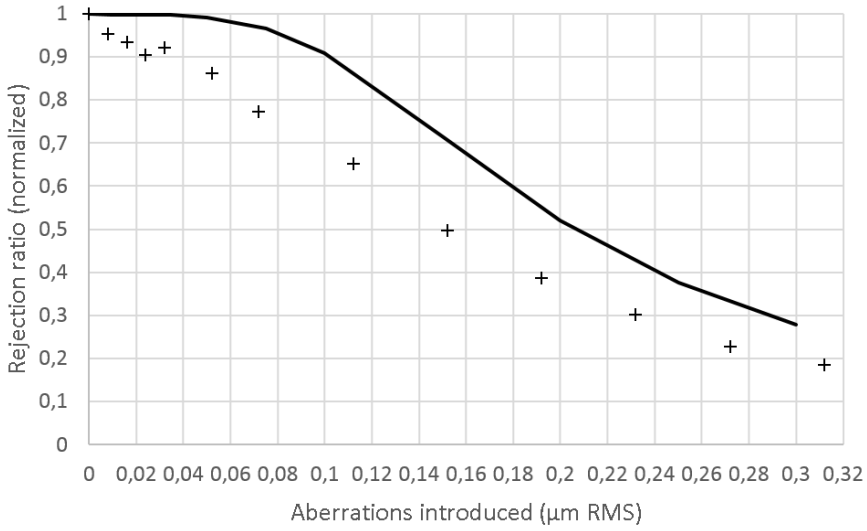

Figure 8.5: Influence of focus on the rejection ratio. Cross marks: experimental results, line: simulation.

In Fig. 8.5 we observe that the AGPM rejection ratio is significantly less sensitive to focus aberrations compared to tip/tilt, confirming the trend from the preliminary results obtained on IRCT and YACADIRE. The experimental results follow the simulation but do not meet even for high level of introduced aberrations. This can be due to the larger than expected amount of residual defocus, and/or to the presence of other low-order aberrations.

8.2.3 Astigmatism

Astigmatism in an optical aberration described by a shift of a beam best focal point between rays propagating in two perpendicular planes. It can be caused by using the outer part of large optics (for example the parabolas on VODCA). The DM minimization routine reduces the astigmatism aberration.

On the right panel of Figure 8.6 is displayed the simulation following the expression of astigmatism in Zernike polynomial:

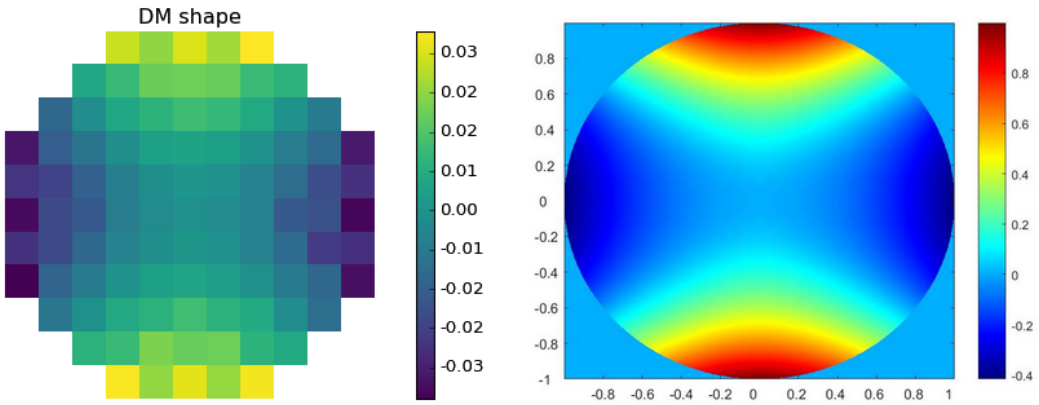

Figure 8.6: Left: Deformable mirror shape. Right : Astigmatism simulation.

$$Z_2^2 = \rho^2 \cos(2\phi). \tag{8.10}$$

On the left panel of Figure 8.6 is the Zernike polynomial projected on the 11x11 actuators deformable mirror.

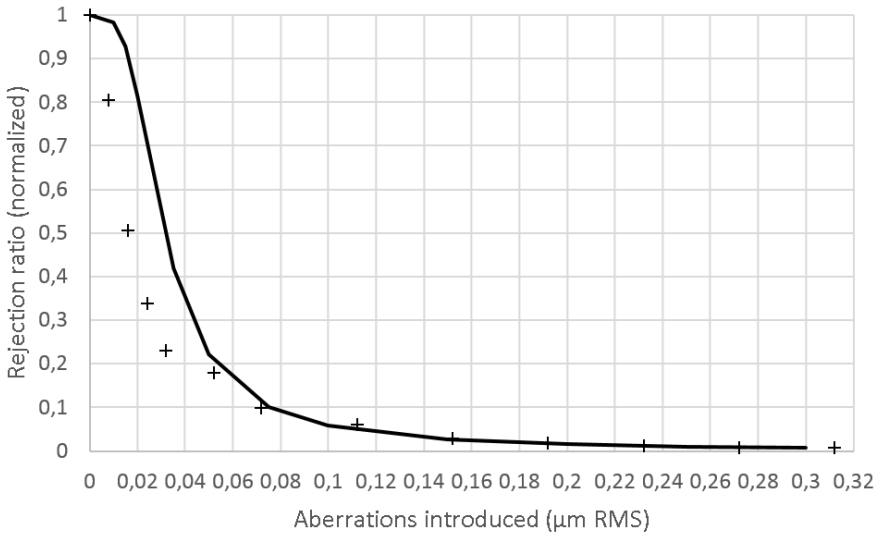

Figure 8.7: Influence of astigmatism on the rejection ratio. Cross marks: experimental results, line: simulation.

The rejection ratio appears to be strongly affected by astigmatism. Similar to the other aberrations, the experimental results follow the simulation trend. In the astigmatism case, the simulation predicts correctly the rejection ratio for aberration introduced >0.05μm.

8.2.4 Coma

Coma is the last aberration investigated. It leads to the distinctive shape of an off-axis point source having a "tail". Coma is by default induced by a parabola when

rays are not parallel to the optical axis. On VODCA, coma can be minimized by a proper alignment and by the DM minimization routine.

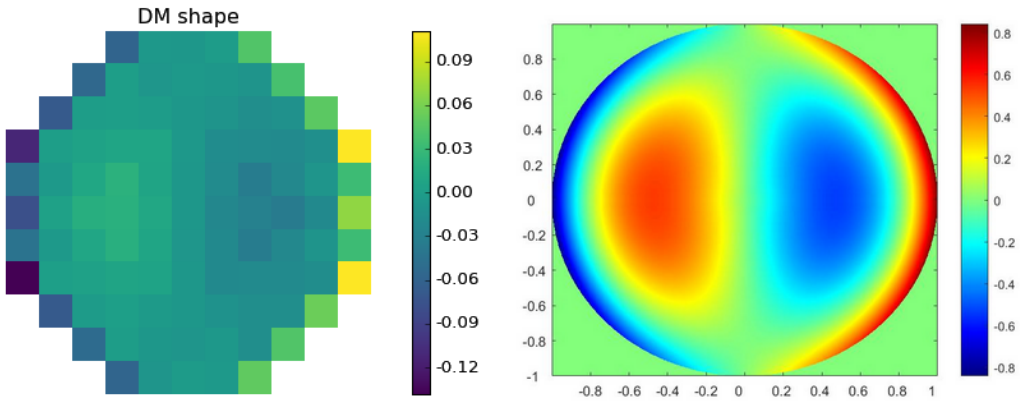

Figure 8.8: Left: Deformable mirror shape. Right : Coma simulation.

On the right panel of Figure 8.8 is displayed the simulation following the expression of coma in Zernike polynomial :

$$Z_1^2 = (3\rho^2 - 2)\rho\, cos(\phi). \tag{8.11}$$

On the left panel of Figure 8.8 is the Zernike polynomial projected on the 11x11 actuators deformable mirror.

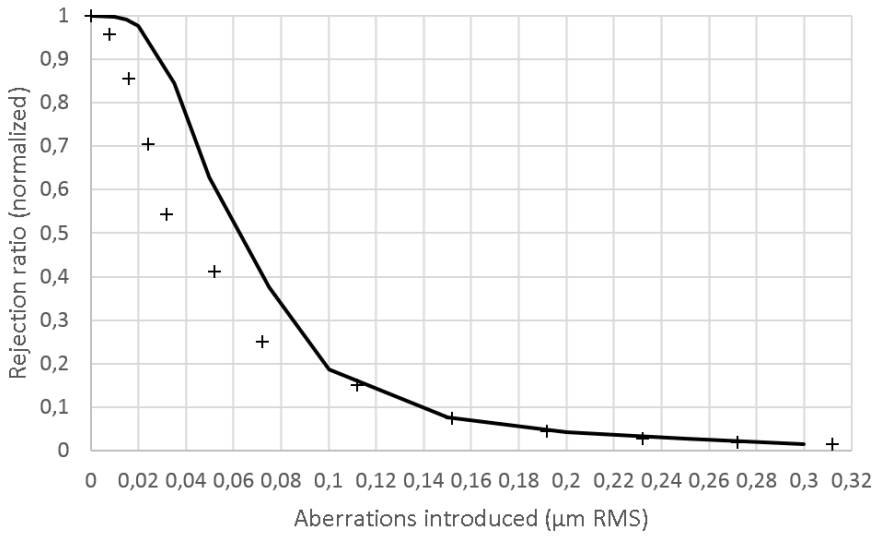

Figure 8.9: Influence of coma on the rejection ratio. Cross marks: experimental results, line: simulation.

Coma, as astigmatism, affects the rejection ratio. In a previous VODCA configuration including two additional off-axis parabolas, the rejection ratios achieved were lower than expected and the aberrations on the bench were more important. The off-axis parabolas (and potential misalignment) introduced astigmatism and coma that were not completely corrected by the DM and the rejection ratio significantly decreased. Experimentally we assumed that the AGPM is more sensitive to coma

and astigmatism compared to the lower order aberrations. Figures 8.9 and 8.7 confirm our first assumption (with astigmatism having the most influence). The results in Fig 8.9 are similar to the previous aberrations studied. The simulation fit to the experimental measurements for aberrations introduced >0.1μm.

8.2.5 Conclusion

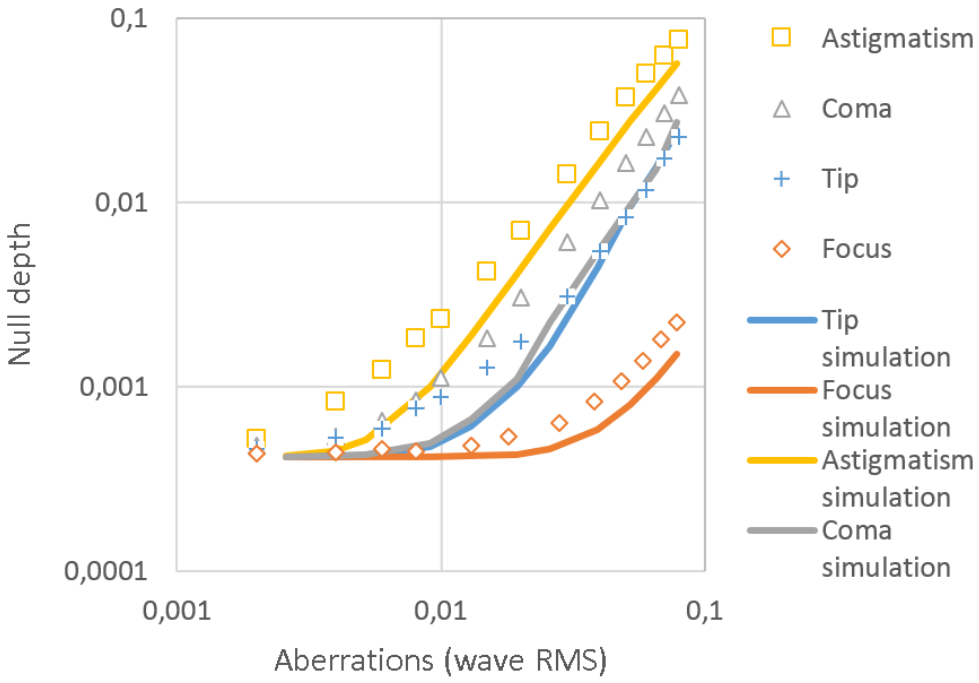

Figure 8.10: Influence of low-order aberrations on the null depth.

The conclusion on the influence of aberration is summarized in Figure 8.10. The results are plotted as the null depth against the introduced aberrations. The minimal null depth common to each aberration curve represents the ideal case on VODCA where a given AGPM reaches its best performance considering the non corrected residual aberrations of the bench. Below 0.005 wave RMS of aberration introduced, the introduced aberrations are small compared to the non-corrected aberrations. Above 0.005 wave RMS the introduced aberrations become more and more predominant, in this region the null depth evolution gives us a better understanding of how sensitive the AGPM performance is to low-order aberrations. The results confirm the first investigations discussed in Section 3.2.1. Aberrations significantly decrease the rejection ratio and the AGPMs react slightly differently to each low order aberration. Astigmatism is the most harmful aberration while focus is the least harmful. The AGPM behavior confirms our expectations even if our simulations do not fit perfectly the experimental results while being fairly close for higher levels of introduced aberrations. The next step for this experiment will be the measurement of the residual aberrations on the bench (through a WFS or other techniques). We will be able to accurately tune the simulations parameters to have a better fit of the VODCA aberrations and then compare the simulations to the experimental results in the same conditions.

8.3 Influence of the incoming beam angle

We have only considered so far the model of an AGPM placed perpendicularly to the incident light. Since the beginning of AGPM testing, the incidence angle of the beam on the mask has been carefully set as close as possible to 0°.

The following experiment aims to evaluate the influence of the variation in the incidence angle on the AGPM. On VODCA, a Thorlabs rotation stage (5 arcmin resolution) allows to easily rotate the AGPM. Its performance was assessed for both negative and positive incidence angles. The standard procedure for rejection ratio evaluation was followed and the mask was aligned after each rotation to prevent non conclusive results due to small misalignments.

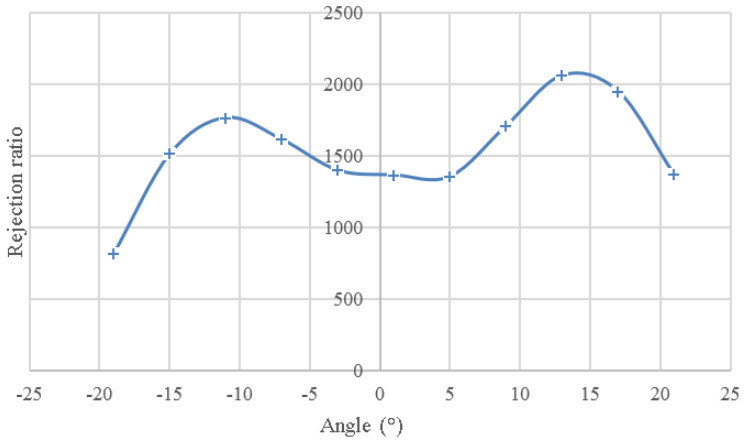

Figure 8.11: Influence of the incidence beam angle on the AGPM null depth.

Contrary to what was expected, the peak in terms of rejection ratio is not reached at a normal incidence. We observe a decrease in this region and a symmetric peak for a 12° incidence (Figure 8.11). Then it naturally decreases for larger angles. This phenomenon has been observed for two different axes of rotation of the AGPM (along the vertical and horizontal axes). Two factors could be at the origin of this behavior.

Firstly, it is well known that an internal reflection occurs inside the AGPM. It is reduced by the ARG etched on one side of the mask. In theory, the ARG reduces the backside reflection from 17% to less than 2%. The remaining light will have multiple reflections inside the 300μm thick mask. At the end, some of this light will propagate along the optical axis towards the camera. In the case of a high performance AGPM, when the rejection ratio is above 1000, it might not be negligible. This can partially explain the drop in performance for low incidence angles. When the angle increases, the reflected leaking light does no longer propagate along the optical axis and will not affect the attenuated PSF.

Secondly, since the AGPM etching process cannot be perfectly controlled, the physical dimensions of the AGPM will slightly differ from the optimal values (in terms of depth and sidewall angle), resulting in suboptimal performance. When the AGPM is rotated, the incident light sees the grating dimensions with a slight modification due to the angle. The period and groove depth will be geometrically reduced. In the case the AGPM grating parameters were originally slightly oversized, it will

now be seen as an optimal dimension mask, thus potentially increasing the rejection ratio until a certain angle.

As a conclusion, the AGPM presents a low sensitivity with respect to the incidence angle of the beam. Setting it up exactly to 0° is not a major issue to consider on an instrument.

This study presents a major limitation that will require further investigations. Our first hypothesis implies that the effect is only visible with high performance ratio (>1000) AGPMs. Only one AGPM has been tested since it was the only mask available with a high rejection ratio at the time these tests were done. More AGPMs have to be studied following the same protocol to conclude on this effect.

9

PERFORMANCE MEASUREMENTS IN OTHER BANDS: H, K AND M

The first AGPMs were developed mainly for the N and L bands. In the course of this thesis, we started to explore other bands at shorter wavelengths thanks to the progress made in the manufacturing process. VODCA has been focused on the performance assessment of L-band AGPMs since the majority of our masks have been etched for this wavelength range, but we also aim to reach the same measurement accuracy in the H, K and M bands.

9.1 M-band AGPMs

On VODCA, the M band is only covered by a monochromatic QCL at 4.6μm. In the future, a 5 μm source will be added to have a better fit of the AGPMs behavior in this region. The aberrations minimization in this band is done using the same protocol as in the L-band with the same performance.

An M band AGPM was needed for the ERIS instrument of the VLT, while a series of AGPMs performing well in both L and M bands were needed for Keck/NIRC2 and LBT/LMIRcam. On VODCA, our L band AGPMs were evaluated in the M band showing poor results. Most rejection ratio were close to 50. The best peaked at 150, which is according to our RCWA simulations, close to the best performance we can expect along such a large bandwidth (from 3.5 to 5 μm). Two were chosen for re-etching AGPM-L12 and AGPM-L13. They previously showed a rejection ratio peak in the L band around 1000 or higher and poor performance in the M band (rejection ratio 50). The goal was to modify their physical dimensions to shift the rejection ratio peak to higher wavelengths (M band). A mask with a rejection ratio is considered correct above 500 and good abve 1000. They have been tested again after re-etching and the modification is clearly noticeable while affecting them differently (see Table 9.1). AGPM-L13r did not perform as expected. Its rejection ratio in L band dropped from 1430 to 176. Meanwhile it did not increase significantly in the M band (50 to 134). This AGPM does not meet the requirements. AGPM-L12r dropped too in the L band but its performance in M band are extremely satisfying (rejection ratio of 1773).

It has been selected to be installed in the ERIS instrument. The L-M band AGPMs now installed on NIRC2 and LMIRcam have rejection ratio $\geq$150 in both bands.

Table 9.1: M band tuning.

REJECTION RATIO					
AGPM	L-BBF	L-NBF1	L-NBF2	L-NBF3	4.6 μm
AGPM-L12r (before)	977 $\pm$56	1958 $\pm$112	942 $\pm$54	327 $\pm$19	53 $\pm$3
After re etching	84 $\pm$5	86 $\pm$5	87 $\pm$5	146 $\pm$8	1773 $\pm$95
AGPM-L13 (before)	1430 $\pm$82	717 $\pm$41	1378 $\pm$79	1448 $\pm$83	50 $\pm$3
After re etching	176 $\pm$10	92 $\pm$5	207 $\pm$12	483 $\pm$28	134 $\pm$7

9.2 H and K bands AGPMs

One H band and two K band AGPMs have been manufactured. In K band, out of the 2 manufactured AGPMs, one has been cracked for inspection, the only one left, K1, showed poor performance (on YACADIRE) with a rejection ratio of 10. After re-etching, it reached 400.

On VODCA, H and K bands AGPM evaluation proved to be a challenge compared to L or M band tests. Rejection ratio higher than 100 could not be reached in the current configuration of VODCA. The deformable mirror routine was unable to perform with the same accuracy at shorter wavelengths compared to L band. It has not been possible to solve this issue so far. The VODCA's layout has been modified and the DM removed. In this configuration, the K1 AGPM reached rejection ratio around 200, which is still half of the performance measured on YACADIRE. This is a totally unanticipated result that we have not been able to explain so far. Access to an infrared wavefront sensor would arguably allow us to give an explanation to this behavior. The K1 AGPM is considered suitable for science observations and has recently been installed in KECK/NIRC2.

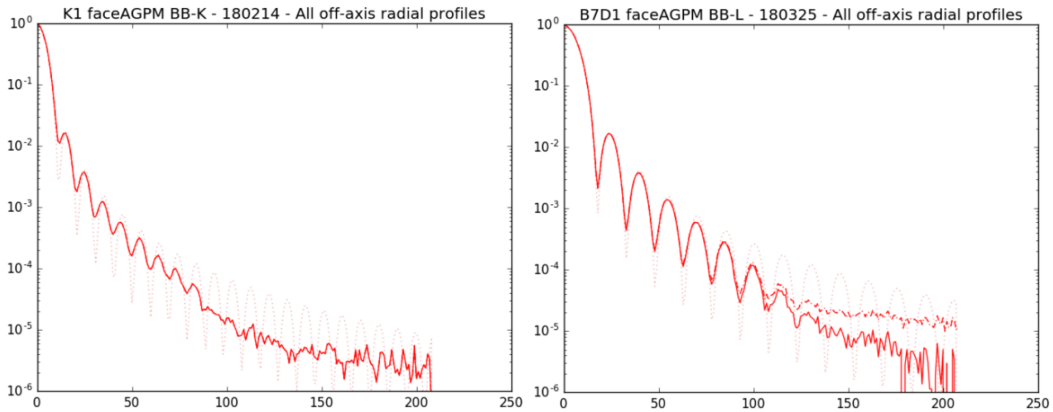

Figure 9.1: Off axis PSF after aberrations minimization. Left : K band. Right : L band.

Observing the off-axis PSF after the minimization routine run by the DM, it appears that aberrations were still affecting the wavefront when compared to L band off-axis PSF (Figure 9.1). The difference becomes obvious when reaching the first dark ring of the Airy pattern. In L band we can reach 2×10^{-3} where it is only 10^{-2} in K band. The K band off-axis PSF is smaller than the L band one (in the L-band we have around 15 pixels per λ/D but only 8 in the K-band). It only partially explains the flux remaining at the first zero of the Airy pattern. The on-axis PSF core appears wider than expected but this behavior was not caused by defocus. In this configuration, the AGPM cannot be properly evaluated since the bench optical quality became the limiting factor of the performance. The solution was to switch back to a previous VODCA layout without DM. This configuration does not allow wavefront control. The low-order aberrations remaining on the bench are more important compared to the layout with the DM operating properly. The results obtained in Section 6.6 proved that the "without-DM" configuration was still showing a good overall optical quality, the rejection ratios measured were only slightly lower than the optimal configuration. We assume that it still meets the requirements for a proper evaluation of H or K band masks.

Except for this, the procedure remains the same regardless of the band. The AGPM performance is assessed using a broad and 3 narrow band filters. AGPM H1, the only H band AGPM tested on VODCA (same conditions) showed really poor performance (<40 in every filter), partially due to the issue stated above but mostly due to the intrinsic quality of the mask.

9.3 Conclusion

In conclusion, despite the excellent optical quality of the bench in L and M bands and its achromatic optical design (between 1.6 and 5 μm), VODCA does not perform at the same level for shorter wavelengths. Pursuing shorter wavelength ranges, the DM appears to not be able to minimize effectively the aberrations in this band. The DM also introduces more aberrations on the bench compared to a layout without DM. Further investigations need to be done on the aberration control to fix this issue. Meanwhile, VODCA can still be used in a sub-optimal state (without DM) to assess K or H band AGPMs if needed. The optical quality of the bench in this layout, while not as good as what we are aiming for, remains correct.

10

BEYOND THE AGPM: CHARGE 4 VORTEX PHASE MASKS

10.1 Introduction to higher topological charges vortex coronagraph

AGPMs induce a 4π continuous helical phase ramp around their axis. The topological charge of a vector vortex coronagraph (VVC) is the number of times the phase accumulates 2π around the axis (see Figure 10.1). AGPMs are subwavelength grating vortex coronagraphs of topological charge 2 (SGVC2). Pursuing higher topological charge vortices is the next major step for VVC. Firstly they are less sensitive to low order optical aberrations, which is a major factor in the achievable rejection ratio. Secondly, their rejection ratios are more robust to partially resolved stars, which might be the case for the next ELT class telescopes. The drawbacks are a larger inner-working angle with higher topological charges (Figure 10.2). These advantages and drawback increase with the topological charge.

10.1.1 From theory to manufacturing

Unlike the SGVC2, which can be easily manufactured thanks to the concentric grating pattern, the same can not be done for the SGVC4 as shown in Fig 10.3. The theory behind the SGVC4 has been described in Delacroix et al. (2014) and will be summarized here.

The theoretical shape has two limitations: (i) it would need an extremely high accuracy of the manufacturing process and (ii) to reach the desired continuous optical axis orientation ω=2θ, the grating period must be locally larger than the subwavelength limit. Tremendous progress has been made with etching and design simulations in the past years, making the SGVC4 manufacturing now feasible. The goal was to find a pattern achievable with the current precision of the manufacturing techniques, while keeping it as close as possible to the theoretical pattern to ensure the best performance of the mask. The main approach consists of discretizing the SGVC4 pattern in segments to remain in the SG condition locally. A higher number of segments will get closer to the theoretical pattern.

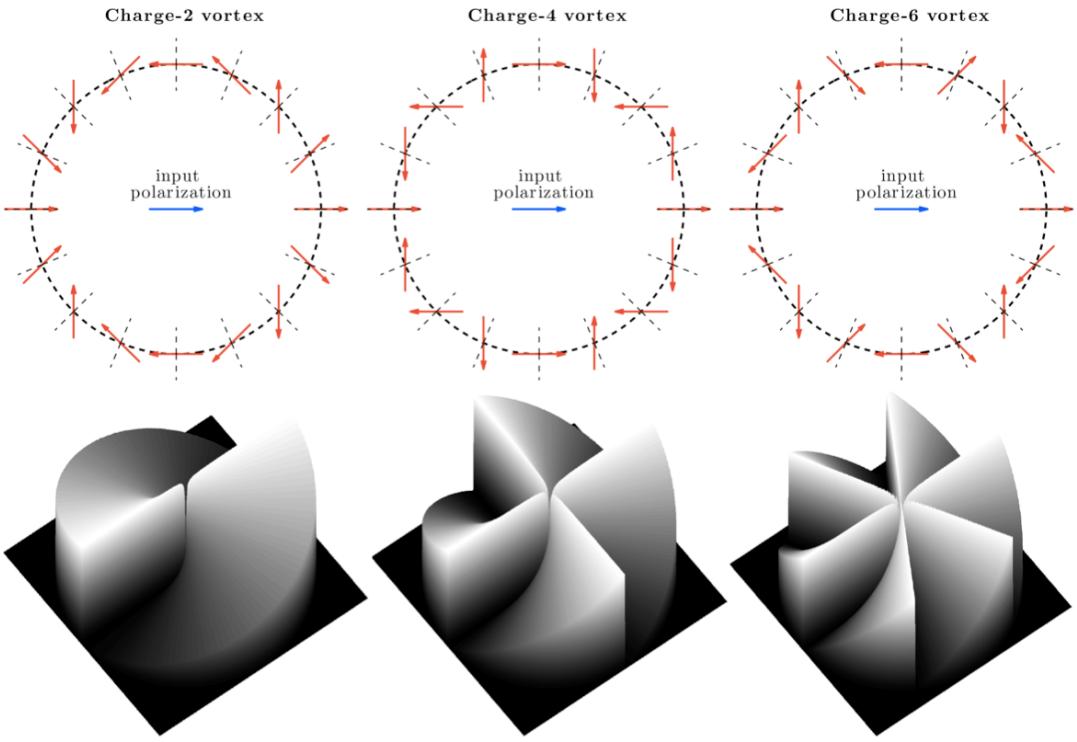

Figure 10.1: The VVC azimuthal phase ramp for charge 2, 4 and 6 VVC.

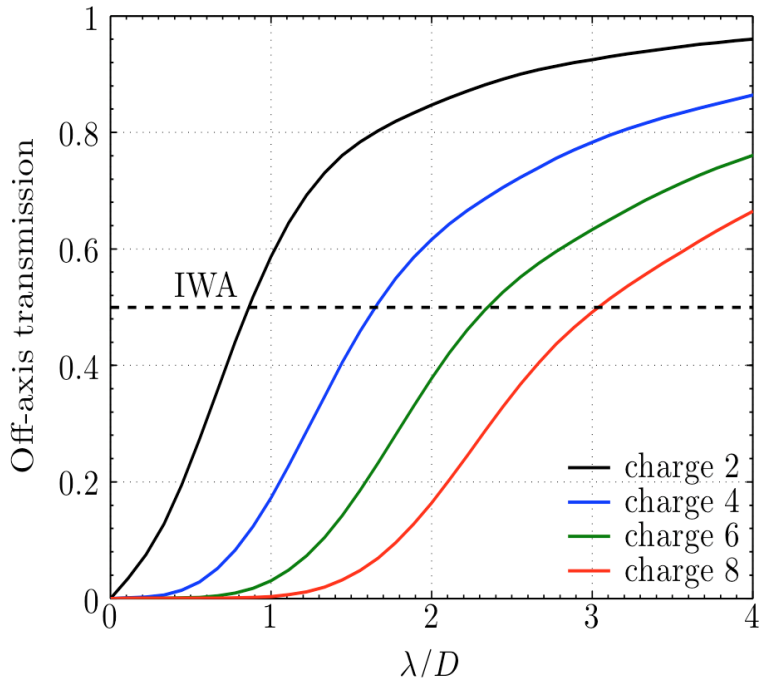

Figure 10.2: Evolution of the inner working angle (IWA) for higher topological charge VVCs.

In each segment, the pattern is approximated with straight or curved lines. A hybrid solution combines both (see Figure 10.4). In the straight lines optimization, due to the discretisation, the phase ramp is not perfectly continuous. Improving

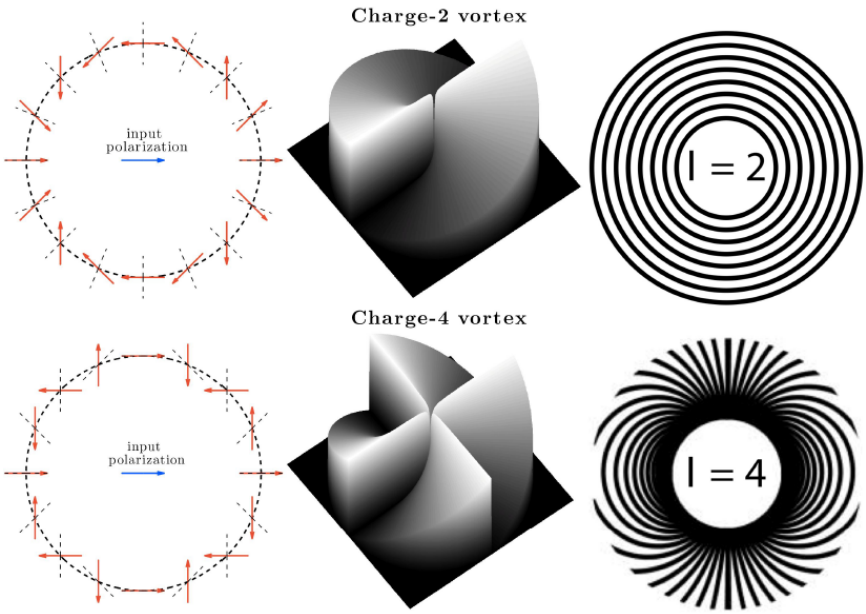

Figure 10.3: Working principle of a vector vortex coronagraph (VVC) of topological charge l=2 (top) and l=4 (bottom). Left: Illustration of a rotating half-wave plate (HWP). The optical axis orientation ω is represented with dashed lines, and it rotates about the center as ω=$\theta l/2$, where θ is the azimuthal coordinate. The HWP effect is to rotate the input polarization (central arrow) by -2α where α is the angle between the incoming polarization direction and the optical axis orientation ω. Middle: The VVC azimuthal phase ramp obtained equals $2\pi l$. Right: Binary grating geometry with constant line width. Only a charge-2 vector vortex coronagraph possesses the required circular symmetry for use with subwavelength gratings (SGVC2 or AGPM), which permits achromatization. For any other charge $l \neq 2$, the grating period is locally larger than the subwavelength limit. From Delacroix et al. (2014).

the continuity implies a large number of segments (N) at the cost of more transition zones between segments. A constant discretisation ($2\pi/N$) creates an unnecessary large number of segments and portions along the x-axis. The optimization through curved lines (where the period can vary) solves the issue along the x-axis but has issues along the y-axis. The hybrid solution combines the straight lines pattern close to the y-axis and the curved lines pattern close to the x-axis.

Recently, three charge 4 vortex phase masks have been etched for the first time. The first one uses discretisation in a 8-segment pattern, and the two others a 32-segment pattern (Figure 10.5).

10.2 Performance in terms of rejection ratio

In this section we present the rejection ratio in L band of the three charge 4 vortex phase masks (Table 10.1). Only SGVC4-S32B reaches acceptable rejection ratio (>600). SGVC4-32A, although having the same pattern, shows significantly lower rejection ratio. It is not possible to conclude on the 8-segment pattern since only one mask has been produced and the poor rejection ratio can be due to manufacturing

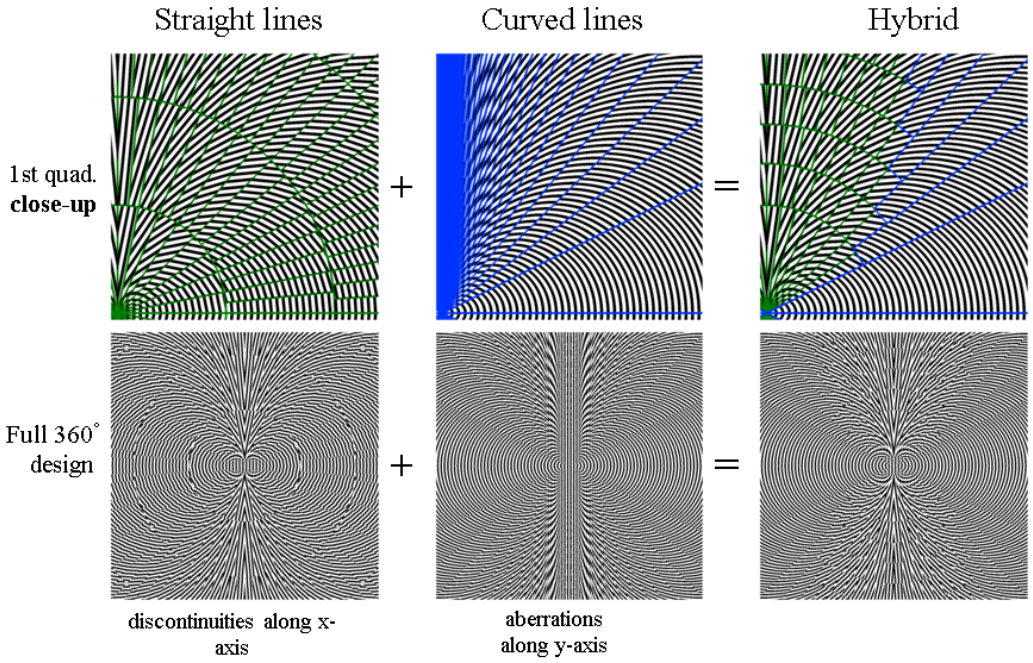

Figure 10.4: Optimized design of the charge-4 VVC using straight lines, curved lines, and an hybrid solution.

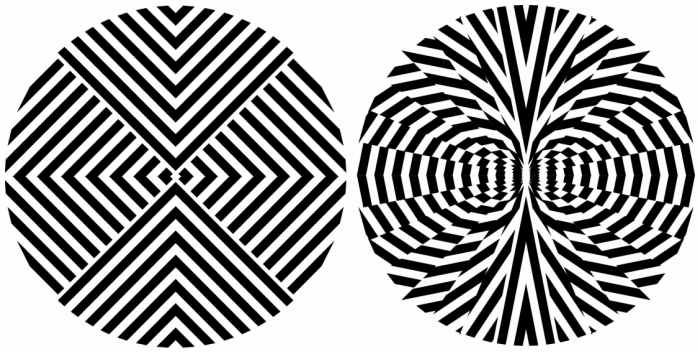

Figure 10.5: Grating designs for the 8 segments (left) and 32 segments masks (right) showing the first 10 periods. Only these two patterns have been successfully etched. From Catalán et al. (2018).

errors. The first SGVC4 performance measured are promising and confirm the validity of the 32-segment straight lines pattern. However, more SGVC4 with various designs, yet to be tested (curved lines and hybrid), will have to be manufactured to conclude on the optimal pattern.

Table 10.1: Rejection ratio of the three SGVC4 manufactured.

	L-BBF	L-NBF1	L-NBF2	L-NBF3
SGVC4-S08	99	75	111	165
SGVC4-S32A	59	57	61	52
SGVC4-S32B	606	962	630	289

The structure of charge 4 vortex phase masks affects their behavior in terms of centering. For charge 2, a drop in intensity clearly identifies the center of the mask. In the case of an 8-segment SGVC4, the transmission between segments features a π phase-shift and therefore leads to a drop in intensity. The first issue is that the transition between segments can be mistaken with the center. The second issue is, when getting closer to the center, the segments merge. It makes the centering routine not reliable anymore. The centering has to be done manually and can result in misalignment. The 32-segment masks proved to be easier to align (because the plane shift is smaller between segments, which leads to only partial attenuation of the star) even though the centering is still manual. Not using the centering routine makes the error budget on each measurement larger. It has not been fully investigated yet. A new automatic centering routine will need to be developed for higher topological charges.

10.3 Influence of aberrations

Theory predicts that charge 4 vortex phase masks are more robust to low order aberrations (tip/tilt and focus). Following the same protocol as described in Section 7.1, the SGVC4-S32B was evaluated. The goal was to compare its behavior with a charge 2 vortex phase mask and to assess how much improvement will provide a charge 4 vortex phase mask. The preliminary tests showed unexpected results, the rejection ratios being stable or even increasing with the introduced aberrations (see figure 10.6). The reason is that the light leaks not only in the center of the PSF but also in considerable amount in the first annulus. Extending the integrated region from a radius of $\lambda/(2D)$ to $2.23\lambda/D$ (from the center of the PSF until the second annulus) allow us to take into account this phenomenon.

We compute the AGPM null depth in the same conditions (integration up to the second annulus), see Figure 10.8. Using this method, we can demonstrate that the SGVC4 is significantly less sensitive than the SGVC2 to the low order aberrations tip and focus than the higher order aberrations such as coma and astigmatism (see Figure 10.7). These results confirm the theoretical results about the SGVC4 behavior relative to aberrations.

10.4 Transmission map

10.4.1 LabVIEW routine

Edges between the different segments and defects in the manufacturing process of such small features affect the transmission of the mask. It is considerably less noticeable in the case of the 32-segments judging by the first rejection ratio evaluations performed. We designed a LabVIEW routine to scan and evaluate the transmission point by point in a 340 μm-box around the center of the mask. It was applied to SGVC4-32B, the only SGVC4 with a correct performance. The area of interest around the center was more densely evaluated since it is where the charge 4 VVC pattern has the smallest features. The pattern being symmetrical, we focused on one quarter of the mask. The routine was intended to minimize the hysteresis inherent to the piezo-actuators by using the center of the mask (lowest transmission) as a reference point. From this, we scanned along one axis over a distance of 1.7 mm. It roughly corresponds to an angular separation of $2\lambda/D$.

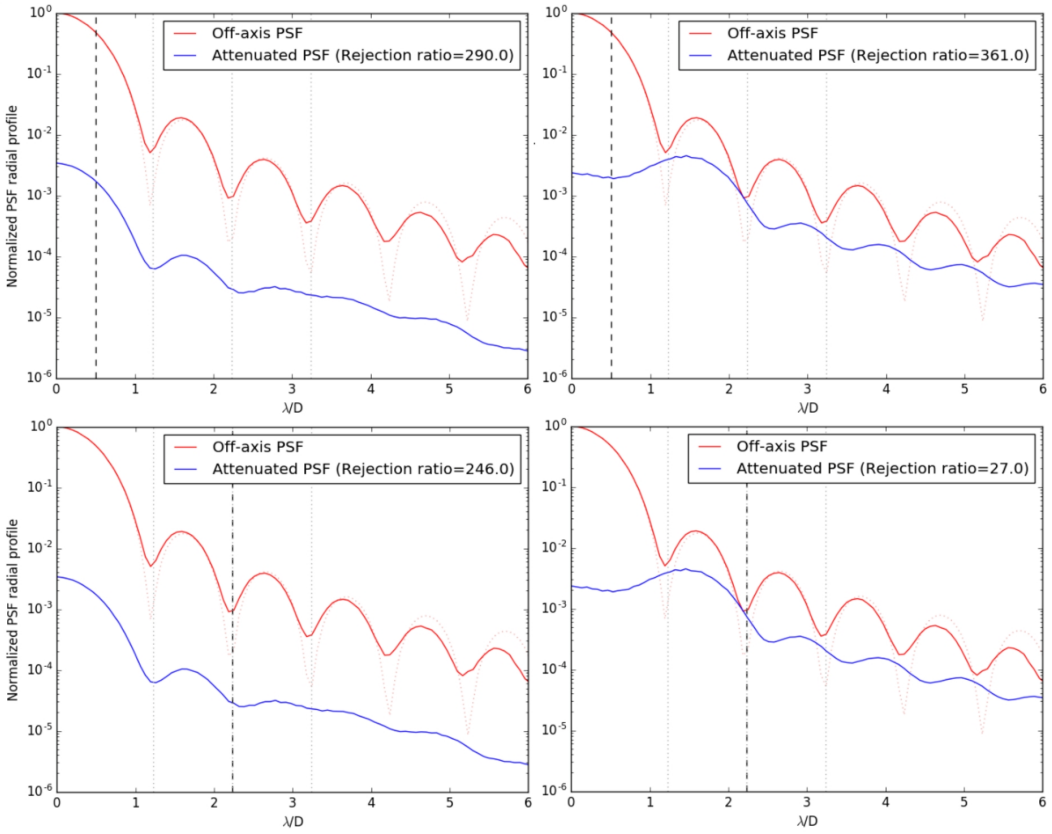

Figure 10.6: Influence of the integration zone on the measured rejection ratio. The rejection ratio is computed by integrating the flux from the center ($0\lambda/D$) to the dashed line (at $0.5\lambda/D$ for the figures on the left, $2.23\lambda/D$ on the right).
Top: Rejection ratio evaluated on the core of the psf. Left: low astigmatism. Right: strong astigmatism.
Bottom: Rejection ratio evaluated until the 2nd annulus. Left: low astigmatism. Right: strong astigmatism.

10.4.2 Results

The structure of the SGVC4 pattern is distinguishable with drops of 20 to 30% at the position of the transition between segments (Figure 10.9). The large number of points implies a time-consuming routine ($\gg$2h) which can lead to additional uncertainties on the measurements due to the time-limit when the bench can be considered stable. The actuators hysteresis influence is particularly visible around the center. Correcting factors need to be estimated and applied to mitigate this issue. As expected, the transition between segments has an effect on the transmission of the mask. This is a drawback compared to SGVC2 which does not have transmission fluctuations (except for the coronagraphic effect). The transition drop is significantly more important for the 8 segments than for the 32 segments. It highlights the role of the discretisation and pattern selection on this behavior. Since only two patterns have been tested so far, we expect that in the future we will be able to find a pattern minimizing the intensity drop at the transition location.

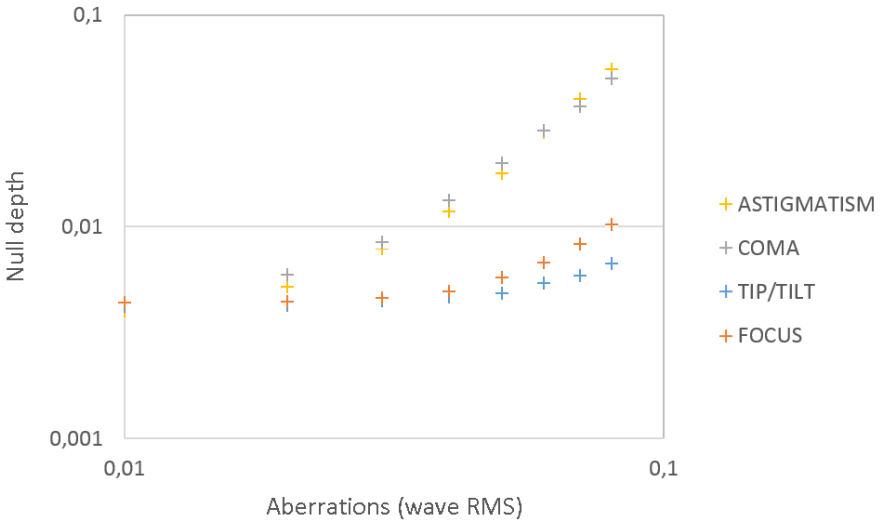

Figure 10.7: Influence of low order aberrations influence on the null depth of a SGVC4.

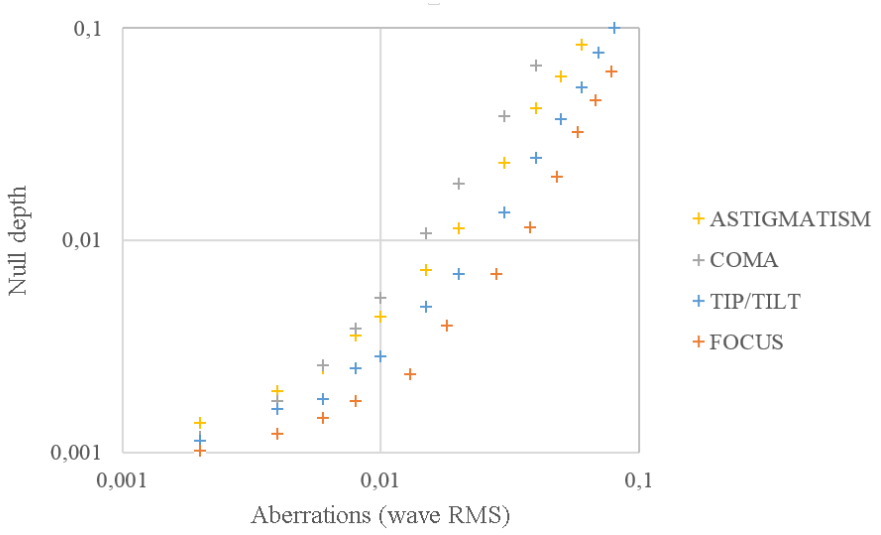

Figure 10.8: Influence of low order aberrations influence on the null depth of a SGVC2.

10.5 Conclusion

SGVC4 manufacturing is still a starting process. The best discretisation of the charge 4 grating pattern is still under discussion and will evolve with the improvement of etching accuracy. To this day, only three SGVC4s have been successfully etched, following two different approaches (8 and 32 segments). Among these, only one showed an acceptable performance. The preliminary results confirm that they are less sensitive to focus and tip/tilt than the AGPM. At this moment and unlike AGPMs, SGVC4s still have an issue of decrease in transmission at the transition between segments. Developing and improving SGVC4s (and higher topological charges) is an essential step for the VORTEX project in the coming years. Low order aberrations

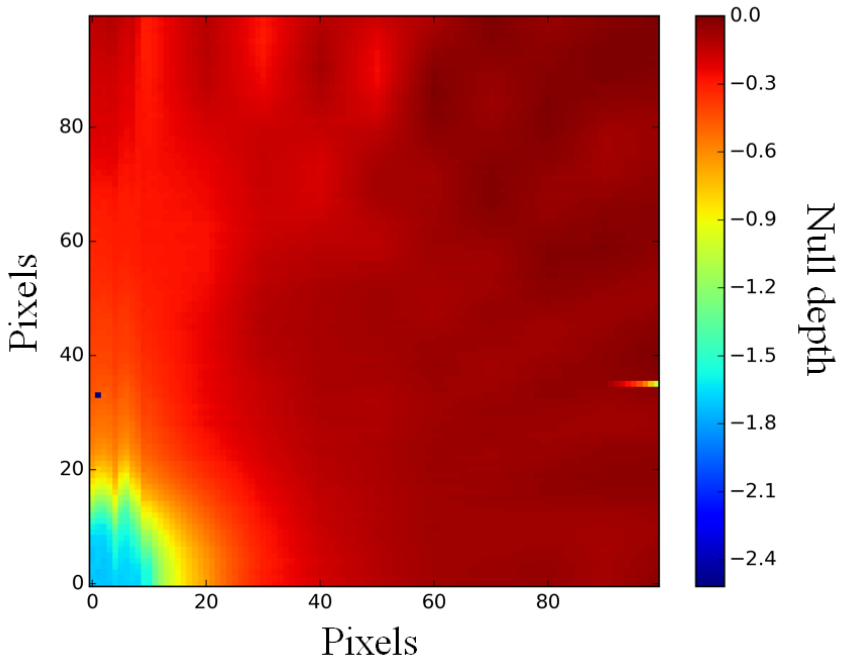

Figure 10.9: Transmission map of SGVC4. The null depth is computed for a 100×100 pixels box. The origin of both axes is defined by the center of the grating pattern (lowest transmission point).

are a common limiting factor for the rejection ratio achieved by AGPMs installed on ground-based telescope instruments. If the inner working angle is not one of the decisive criteria for the intended observations, SGVC4s will be a major improvement. The influence of partially resolved stars on the residual starlight will also be in favor of SGVC4s compared to AGPMs.

PART IV

Conclusion and perspectives

In this dissertation, we have presented the high contrast coronagraphic test bench VODCA (Vortex Optical Demonstrator for Coronagraphic Applications) and the latest results with AGPMs.

In the first part, we described the optical benches (IRCT and YACADIRE) used until 2014 for AGPM performance assessment. Rejection ratios of a few hundreds were measured, sufficient to satisfy the requirements for installation on ground-based telescopes but the measured rejection ratios were below the performance we expected from RCWA simulations. The experimental conditions strongly limited the rejection ratio measurements achievable by the AGPMs.

Accurate measurements of our AGPMs are much needed since they allow us to derive the exact parameters of the subwavelength gratings, and thereby evaluate the quality of the manufacturing process. From these experiences, we established a list of requirements towards designing and operating the first testing facility only dedicated to VVC. Our aim is to simulate the coronagraphic procedure as it happens inside a telescope by introducing a light source comparable to a star in order to assess the quality of the manufactured phase masks. VODCA aims to produce measurements as close as possible to the intrinsic limit of each mask. This limit depends on two factors, the physical dimensions of the subwavelength grating and potential defects in the substrate and grating.

We described extensively VODCA's layout and the operating software. According to the literature, the AGPM sensitivity to aberrations and jitter are the main causes of performance loss (along with non circular aperture). We introduced and discussed on the DM optimization routine and the centering routine as they are major improvements compared to the test-benches previously used. They also improved the repeatability and as a consequence the time efficiency of the measurements. We are confident to produce a single measurement with less than 5% error (that could be further reduced with a larger number of measurements or fine-tuning of the software).

In the second part of this thesis, we described the tests conducted on the AGPMs. With VODCA, we achieved the highest rejection ratios ever measured for AGPMs at L-band. We were able to reach a rejection ratio as high as 3.2×10^3 in a narrow band filter (3425-3525nm) and as high as 2.4×10^3 in the broad L band (3575-4125nm) for AGPM-L11r. These rejection ratios are consistent with the intrinsic, chromatic limits of AGPMs based on RWCA simulations. They prove that (i) our etching techniques have reached a sufficient accuracy to produce AGPMs with the highest possible performance, and (ii) that the VODCA bench provides a sufficiently high optical quality to measure the intrinsic limit of any foreseeable AGPMs. In addition, VODCA provides an essential tool to accurately assess the values of the AGPM grating parameters by combining accurate measurements in several narrow-band filters with RCWA modeling. This new feature, coupled with a continuously improving manufacturing process has led to the successful re-etching of AGPMs to improve their performance (up to the theoretical limit set by chromatism over the whole L-band). Operating with high-performance phase masks highlights the major role played by wavefront quality. We showed that the contrast measured for separation larger than 1.0 λ/D depends critically on the aberration distribution on the bench. In our case, this distribution is mostly affected by the surface control and quality of the deformable mirror. The contrast at smaller separation (evaluated by the rejection ratio) is mostly affected by low-order aberrations. We confirmed that a few tens nm RMS drastically decreases the starlight rejection. The AGPM rejection

ratio is significantly more sensitive to astigmatism while being more resilient to defocus.

Only a few AGPMs have been optimized for shorter wavelengths (H- and K-bands) and tested on VODCA. The aberrations minimization routine could not reproduce the performance achieved in L-band in terms of wavefront control. A VODCA layout without DM has been implemented to perform the H- and K-band AGPM tests. A K-band AGPM measured with a rejection ratio of 400 is the only suitable for science observations. The others did not meet the minimum requirements. If new AGPMs are manufactured in these spectral regions, we still strive to solve the routine issue and produce measurements with a similar quality compared to the L-band.

In the last part of this thesis, we initiated the first measurements of higher topological charge VVCs. Charge 4 SGVC design and manufacturing are making steady progress and the first three masks were recently produced. One of the three, based on the 32-segments discretisation pattern, shows satisfactory performance (>600 in L-band). One of the reasons for pursuing higher topological charge phase masks is the resilience to low order aberrations. We confirmed experimentally that charge 4 SGVCs are considerably less sensitive to defocus and tip/tilt compared to charge 2 VVC. As the Vortex project will be required in the future to master charge 4 and higher VVCs, VODCA will continue to evolve to characterize in every aspects all VVCs in all spectral ranges.

Further developments on VODCA will be focused on two main directions.

(i) Accurate aberration measurements appear to be a crucial aspect of our SGVC performance assessment. Having access to accurate aberration measurements will take the wavefront correction to the next level making it significantly faster and more efficient (considering the limit set by the currently used hardware), and will allow us to characterize more precisely the aberrations influence on our masks behavior. The SGVC behavior has only been described for low order aberrations individually. We aim to experimentally study it when subject to a distribution of various aberrations. In this context, an IR wavefront sensor (IRWFS) will be extremely helpful if introduced in the current VODCA layout. At the same time, we are attempting to implement a Zernike wavefront sensor (ZFWS) on VODCA. A ZFWS consists of a phase mask with a central step which applies a $\pi/2$ phase-shift to the wavefront. It converts the phase aberrations into intensity variations that can be measured in the pupil plane. The preliminary results are promising but further developments need to be done in terms of software integration, Zernike mask alignment, and pupil imaging.

(ii) Until now, we only evaluated our SGVC with a circular and unobstructed aperture since this case allows to reach the highest rejection ratio (perfect case). Unfortunately, large ground-based telescope apertures have central obstructions and spider-arms, some of them are not circular and the size of these features varies from one telescope to another. The diffraction pattern created leads to lower rejection ratios. On VODCA, we want to confirm experimentally how the aperture shape affects the performance. Different entrance pupil shapes and Lyot stops have been designed to reproduce large ground-based telescopes apertures but manufacturing difficulties prevented us from testing them. Various apodizations solutions will also

be tested on VODCA to mitigate the effects of spider arms and central obstructions.

Part V

Appendix

PUBLICATIONS WITH MAJOR CONTRIBUTION

Aïssa Jolivet, Gilles Orban de Xivry, Elsa Huby, Pierre Piron, Ernesto Vargas Catalan, Serge Habraken, Jean Surdej, Mikael Karlsson, and Oliver Absil. L- and M-band annular groove phase mask in lab performance assessment on the vortex optical demonstrator for coronagraphic applications. *Journal of Astronomical Telescopes, Instruments, and Systems*, 5(02):1, April 2019. ISSN 2329-4124. doi:10.1117/1.JATIS.5.2.025001. URL https://www.spiedigitallibrary.org/journals/Journal-of-Astronomical-Telescopes-Instruments-and-Systems/volume-5/issue-02/025001/L--and-M-band-annular-groove-phase-mask-in/10.1117/1.JATIS.5.2.025001.full.

Ernesto Vargas Catalán, Pierre Piron, Aïssa Jolivet, Pontus Forsberg, Christian Delacroix, Elsa Huby, Olivier Absil, Ismo Vartiainen, Markku Kuittinen, and Mikael Karlsson. Subwavelength diamond gratings for vortex coronagraphy: towards an annular groove phase mask for shorter wavelengths and topological charge 4 designs. *Optical Materials Express*, 8(7):1976–1987, July 2018. ISSN 2159-3930. doi:10.1364/OME.8.001976. URL https://www.osapublishing.org/ome/abstract.cfm?uri=ome-8-7-1976.

E. Vargas Catalán, E. Huby, P. Forsberg, A. Jolivet, P. Baudoz, B. Carlomagno, C. Delacroix, S. Habraken, D. Mawet, J. Surdej, O. Absil, and M. Karlsson. Optimizing the subwavelength grating of L -band annular groove phase masks for high coronagraphic performance. *Astronomy & Astrophysics*, 595:A127, November 2016. ISSN 0004-6361, 1432-0746. doi:10.1051/0004-6361/201628739. URL http://www.aanda.org/10.1051/0004-6361/201628739.

A. Jolivet, P. Piron, E. Huby, O. Absil, C. Delacroix, D. Mawet, J. Surdej, and S. Habraken. The VORTEX coronagraphic test bench. page 91515P, Montréal, Quebec, Canada, July 2014. doi:10.1117/12.2055791. URL http://proceedings.spiedigitallibrary.org/proceeding.aspx?doi=10.1117/12.2055791.

Gilles Orban de Xivry, Olivier Absil, Elsa Huby, and Aïssa Jolivet. Post-coronagraphic PSF sharpening with the vortex coronagraph. In *Proceedings of the Adaptive Optics for Extremely Large Telescopes 5*. Instituto de Astrofisica de Canarias (IAC), 2017. doi:10.26698/AO4ELT5.0066. URL http://www.iac.es/congreso/AO4ELT5/pages/proceeding.php?id=66.

PUBLICATIONS WITH MINOR CONTRIBUTION

M. Reggiani, V. Christiaens, O. Absil, D. Mawet, E. Huby, E. Choquet, C. A. Gomez Gonzalez, G. Ruane, B. Femenia, E. Serabyn, K. Matthews, M. Barraza, B. Carlomagno, D. Defrère, C. Delacroix, S. Habraken, A. Jolivet, M. Karlsson, G. Orban de Xivry, P. Piron, J. Surdej, E. Vargas Catalan, and O. Wertz. Discovery of a point-like source and a third spiral arm in the transition disk around the Herbig Ae star MWC 758. *Astronomy & Astrophysics*, 611:A74, March 2018. ISSN 0004-6361, 1432-0746. doi:10.1051/0004-6361/201732016. URL https://www.aanda.org/articles/aa/abs/2018/03/aa32016-17/aa32016-17.html.

E. Serabyn, E. Huby, K. Matthews, D. Mawet, O. Absil, B. Femenia, P. Wizinowich, M. Karlsson, M. Bottom, R. Campbell, B. Carlomagno, D. Defrère, C. Delacroix, P. Forsberg, C. Gomez Gonzalez, S. Habraken, A. Jolivet, K. Liewer, S. Lilley, P. Piron, M. Reggiani, J. Surdej, H. Tran, E. Vargas Catalán, and O. Wertz. THE W. M. KECK OBSERVATORY INFRARED VORTEX CORONAGRAPH AND A FIRST IMAGE OF HIP 79124 B. *The Astronomical Journal*, 153(1):43, January 2017. ISSN 1538-3881. doi:10.3847/1538-3881/153/1/43. URL http://stacks.iop.org/1538-3881/153/i=1/a=43?key=crossref.3440bf8688a5fc91a6bdc5c64decdc88.

Dimitri Mawet, Élodie Choquet, Olivier Absil, Elsa Huby, Michael Bottom, Eugene Serabyn, Bruno Femenia, Jérémy Lebreton, Keith Matthews, Carlos A. Gomez Gonzalez, Olivier Wertz, Brunella Carlomagno, Valentin Christiaens, Denis Defrère, Christian Delacroix, Pontus Forsberg, Serge Habraken, Aissa Jolivet, Mikael Karlsson, Julien Milli, Christophe Pinte, Pierre Piron, Maddalena Reggiani, Jean Surdej, and Ernesto Vargas Catalan. CHARACTERIZATION OF THE INNER DISK AROUND HD 141569 A FROM KECK/NIRC2 L-BAND VORTEX CORONAGRAPHY. *The Astronomical Journal*, 153(1):44, January 2017. ISSN 1538-3881. doi:10.3847/1538-3881/153/1/44. URL http://stacks.iop.org/1538-3881/153/i=1/a=44?key=crossref.b924c4383198a6d0970c44119645424a.

Bruno Femenía Castellá, Eugene Serabyn, Dimitri Mawet, Olivier Absil, Peter Wizinowich, Keith Matthews, Elsa Huby, Michael Bottom, Randy Campbell, Dwight Chan, Brunella Carlomagno, Sylvain Cetre, Denis Defrère, Christian Delacroix, Carlos Gomez Gonzalez, Aïssa Jolivet, Mikael Karlsson, Kyle Lanclos, Scott Lilley, Steven Milner, Henry Ngo, Maddalena Reggiani, Julia Simmons, Hien Tran, Ernesto Vargas Catalan, and Olivier Wertz. Commissioning and first light results of an L'-band vortex coronagraph with the Keck II adaptive optics NIRC2 science instrument. In *Adaptive Optics Systems V*, volume 9909, page 990922. International Society for Optics and Photonics, July 2016. doi:10.1117/12.2233228. URL https://www.spiedigitallibrary.org/conference-proceedings-of-spie/9909/

990922/Commissioning-and-first-light-results-of-an-L-band-vortex/10.1117/12.2233228.short.

Olivier Absil, Dimitri Mawet, Mikael Karlsson, Brunella Carlomagno, Valentin Christiaens, Denis Defrère, Christian Delacroix, Bruno Femenía Castella, Pontus Forsberg, Julien Girard, Carlos A. Gómez González, Serge Habraken, Philip M. Hinz, Elsa Huby, Aïssa Jolivet, Keith Matthews, Julien Milli, Gilles Orban de Xivry, Eric Pantin, Pierre Piron, Maddalena Reggiani, Garreth J. Ruane, Gene Serabyn, Jean Surdej, Konrad R. W. Tristram, Ernesto Vargas Catalán, Olivier Wertz, and Peter Wizinowich. Three years of harvest with the vector vortex coronagraph in the thermal infrared. In *Ground-based and Airborne Instrumentation for Astronomy VI*, volume 9908, page 99080Q. International Society for Optics and Photonics, August 2016. doi:10.1117/12.2233289. URL https://www.spiedigitallibrary.org/conference-proceedings-of-spie/9908/99080Q/Three-years-of-harvest-with-the-vector-vortex-coronagraph-in/10.1117/12.2233289.short.

Olivier Absil, Dimitri Mawet, Christian Delacroix, Pontus Forsberg, Mikael Karlsson, Serge Habraken, Jean Surdej, Pierre-Antoine Absil, Brunella Carlomagno, Valentin Christiaens, Denis Defrère, Carlos Gomez Gonzalez, Elsa Huby, Aïssa Jolivet, Julien Milli, Pierre Piron, Ernesto Vargas Catalan, and Marc Van Droogenbroeck. The VORTEX project: first results and perspectives. In *Adaptive Optics Systems IV*, volume 9148, page 91480M. International Society for Optics and Photonics, July 2014. doi:10.1117/12.2055702. URL https://www.spiedigitallibrary.org/conference-proceedings-of-spie/9148/91480M/The-VORTEX-project-first-results-and-perspectives/10.1117/12.2055702.short.

Brunella Carlomagno, Christian Delacroix, Olivier Absil, Pontus Forsberg, Serge Habraken, Aïssa Jolivet, Mikael Karlsson, Dimitri Mawet, Pierre Piron, Jean Surdej, and Ernesto Vargas Catalan. Mid-IR AGPMs for ELT applications. In *Ground-based and Airborne Instrumentation for Astronomy V*, volume 9147, page 914799. International Society for Optics and Photonics, July 2014. doi:10.1117/12.2056280. URL https://www.spiedigitallibrary.org/conference-proceedings-of-spie/9147/914799/Mid-IR-AGPMs-for-ELT-applications/10.1117/12.2056280.short.

D. Defrere, O. Absil, D. Mawet, K. Michael, S. Habraken, J. Surdej, P.-A. Absil, B. Carlomagno, V. Christiaens, C. Delacroix, J. Girard, P. Forsberg, C. Gomez Gonzalez, P. Hinz nd E. Huby, A. Jolivet, J. Milli, E. Pantin, P. Piron, E. Serabyn, M. Van Droogenbroeck, E. Vargas, and O. Wertz. Direct exoplanet imaging with small-angle Vortex coronagraphs. In *Proceedings of the Pathways Towards Habitable Planets Conference*, pages 1–20, Bern, Switzerland, July 2015. URL http://hdl.handle.net/2268/205177.

BIBLIOGRAPHY

Olivier Absil, Dimitri Mawet, Christian Delacroix, Pontus Forsberg, Mikael Karlsson, Serge Habraken, Jean Surdej, Pierre-Antoine Absil, Brunella Carlomagno, Valentin Christiaens, Denis Defrère, Carlos Gomez Gonzalez, Elsa Huby, Aïssa Jolivet, Julien Milli, Pierre Piron, Ernesto Vargas Catalan, and Marc Van Droogenbroeck. The VORTEX project: first results and perspectives. In *Adaptive Optics Systems IV*, volume 9148, page 91480M. International Society for Optics and Photonics, July 2014. doi:10.1117/12.2055702. URL https://www.spiedigitallibrary.org/conference-proceedings-of-spie/9148/91480M/The-VORTEX-project-first-results-and-perspectives/10.1117/12.2055702.short.

Olivier Absil, Dimitri Mawet, Mikael Karlsson, Brunella Carlomagno, Valentin Christiaens, Denis Defrère, Christian Delacroix, Bruno Femenía Castella, Pontus Forsberg, Julien Girard, Carlos A. Gómez González, Serge Habraken, Philip M. Hinz, Elsa Huby, Aïssa Jolivet, Keith Matthews, Julien Milli, Gilles Orban de Xivry, Eric Pantin, Pierre Piron, Maddalena Reggiani, Garreth J. Ruane, Gene Serabyn, Jean Surdej, Konrad R. W. Tristram, Ernesto Vargas Catalán, Olivier Wertz, and Peter Wizinowich. Three years of harvest with the vector vortex coronagraph in the thermal infrared. page 99080Q, Edinburgh, United Kingdom, August 2016. doi:10.1117/12.2233289. URL http://proceedings.spiedigitallibrary.org/proceeding.aspx?doi=10.1117/12.2233289.

A. Boccaletti, P. Riaud, P. Baudoz, J. Baudrand, D. Rouan, D. Gratadour, F. Lacombe, and A.-M. Lagrange. The Four-Quadrant Phase Mask Coronagraph. IV. First Light at the Very Large Telescope. *Publications of the Astronomical Society of the Pacific*, 116 (825):1061–1071, November 2004. ISSN 0004-6280, 1538-3873. doi:10.1086/425735. URL http://iopscience.iop.org/article/10.1086/425735.

Ernesto Vargas Catalán, Pierre Piron, Aïssa Jolivet, Pontus Forsberg, Christian Delacroix, Elsa Huby, Olivier Absil, Ismo Vartiainen, Markku Kuittinen, and Mikael Karlsson. Subwavelength diamond gratings for vortex coronagraphy: towards an annular groove phase mask for shorter wavelengths and topological charge 4 designs. *Optical Materials Express*, 8(7):1976, July 2018. ISSN 2159-3930. doi:10.1364/OME.8.001976. URL https://www.osapublishing.org/abstract.cfm?URI=ome-8-7-1976.

Johanan L. Codona and Roger Angel. Imaging Extrasolar Planets by Stellar Halo Suppression in Separately Corrected Color Bands. *The Astrophysical Journal*, 604 (2):L117–L120, April 2004. ISSN 0004-637X, 1538-4357. doi:10.1086/383569. URL http://stacks.iop.org/1538-4357/604/i=2/a=L117.

Richard Dekany, Jennifer Roberts, Rick Burruss, Antonin Bouchez, Tuan Truong, Christoph Baranec, Stephen Guiwits, David Hale, John Angione, Thang Trinh, Jeffry Zolkower, J. Christopher Shelton, Dean Palmer, John Henning, Ernest Croner, Mitchell Troy, Dan McKenna, Jonathan Tesch, Sergi Hildebrandt, and Jennifer Milburn. PALM-3000: EXOPLANET ADAPTIVE OPTICS FOR THE 5 m HALE TELESCOPE. *The Astrophysical Journal*, 776(2):130, October 2013. ISSN 0004-637X, 1538-4357. doi:10.1088/0004-637X/776/2/130. URL http://stacks.iop.org/0004-637X/776/i=2/a=130?key=crossref.6cdf82f375a71c9c2c63a25f2d294a25.

C. Delacroix, P. Forsberg, M. Karlsson, D. Mawet, C. Lenaerts, S. Habraken, C. Hanot, J. Surdej, A. Boccaletti, and J. Baudrand. Annular groove phase mask coronagraph in diamond for mid-IR wavelengths: manufacturing assessment and performance analysis. page 77314W, San Diego, California, USA, July 2010. doi:10.1117/12.858278. URL http://proceedings.spiedigitallibrary.org/proceeding.aspx?doi=10.1117/12.858278.

C. Delacroix, O. Absil, P. Forsberg, D. Mawet, V. Christiaens, M. Karlsson, A. Boccaletti, P. Baudoz, M. Kuittinen, I. Vartiainen, J. Surdej, and S. Habraken. Laboratory demonstration of a mid-infrared AGPM vector vortex coronagraph. *Astronomy & Astrophysics*, 553:A98, May 2013. ISSN 0004-6361, 1432-0746. doi:10.1051/0004-6361/201321126. URL http://www.aanda.org/10.1051/0004-6361/201321126.

Christian Delacroix. *Exoplanet imaging with mid-infrared vector vortex coronagraphs: design, manufacture, validation and first light of the annular groove phase mask*. PhD thesis, Universite de Liege, The address of the publisher, June 2013. https://orbi.uliege.be/handle/2268/150630.

Christian Delacroix, Pontus Forsberg, Mikael Karlsson, Dimitri Mawet, Olivier Absil, Charles Hanot, Jean Surdej, and Serge Habraken. Design, manufacturing, and performance analysis of mid-infrared achromatic half-wave plates with diamond subwavelength gratings. *Applied Optics*, 51(24):5897, August 2012. ISSN 1559-128X, 2155-3165. doi:10.1364/AO.51.005897. URL https://www.osapublishing.org/abstract.cfm?URI=ao-51-24-5897.

Christian Delacroix, Olivier Absil, Brunella Carlomagno, Pierre Piron, Pontus Forsberg, Mikael Karlsson, Dimitri Mawet, Serge Habraken, and Jean Surdej. Development of a subwavelength grating vortex coronagraph of topological charge 4 (SGVC4). page 91478Y, Montréal, Quebec, Canada, July 2014. doi:10.1117/12.2055798. URL http://proceedings.spiedigitallibrary.org/proceeding.aspx?doi=10.1117/12.2055798.

L. Drake Deming and Sara Seager. Illusion and reality in the atmospheres of exoplanets: Illusion and Reality for Exoplanets. *Journal of Geophysical Research: Planets*, 122(1):53–75, January 2017. ISSN 21699097. doi:10.1002/2016JE005155. URL http://doi.wiley.com/10.1002/2016JE005155.

Gregory Foo, David M. Palacios, and Grover A. Swartzlander. Optical vortex coronagraph. *Optics Letters*, 30(24):3308, December 2005. ISSN 0146-9592, 1539-4794. doi:10.1364/OL.30.003308. URL https://www.osapublishing.org/abstract.cfm?URI=ol-30-24-3308.

Pontus Forsberg and Mikael Karlsson. High aspect ratio optical gratings in diamond. *Diamond and Related Materials*, 34:19–24, April 2013. ISSN 09259635. doi:10.1016/j.diamond.2013.01.009. URL https://linkinghub.elsevier.com/retrieve/pii/S0925963513000198.

Carlos Alberto Gomez Gonzalez, Olivier Wertz, Olivier Absil, Valentin Christiaens, Denis Defrère, Dimitri Mawet, Julien Milli, Pierre-Antoine Absil, Marc Van Droogenbroeck, Faustine Cantalloube, Philip M. Hinz, Andrew J. Skemer, Mikael Karlsson, and Jean Surdej. VIP : Vortex Image Processing Package for High-contrast Direct Imaging. *The Astronomical Journal*, 154(1):7, June 2017. ISSN 1538-3881. doi:10.3847/1538-3881/aa73d7. URL http://stacks.iop.org/1538-3881/154/i=1/a=7?key=crossref.f935c4cecf1d1177e95108ad4c831a0c.

O. Guyon, E. A. Pluzhnik, M. J. Kuchner, B. Collins, and S. T. Ridgway. Theoretical Limits on Extrasolar Terrestrial Planet Detection with Coronagraphs. *The Astrophysical Journal Supplement Series*, 167(1):81–99, November 2006. ISSN 0067-0049, 1538-4365. doi:10.1086/507630. URL http://stacks.iop.org/0067-0049/167/i=1/a=81.

Olivier Guyon, Claude Roddier, J. Elon Graves, François Roddier, Salvador Cuevas, Carlos Espejo, Salustio Gonzalez, Andrea Martinez, Gianfranco Bisiacchi, and Valeri Vuntesmeri. The Nulling Stellar Coronagraph: Laboratory Tests and Performance Evaluation. *Publications of the Astronomical Society of the Pacific*, 111(764): 1322–1331, October 1999. ISSN 0004-6280, 1538-3873. doi:10.1086/316445. URL http://iopscience.iop.org/article/10.1086/316445.

Olivier Guyon, Frantz Martinache, Ruslan Belikov, and Remi Soummer. HIGH PERFORMANCE PIAA CORONAGRAPHY WITH COMPLEX AMPLITUDE FOCAL PLANE MASKS. *The Astrophysical Journal Supplement Series*, 190 (2):220–232, October 2010. ISSN 0067-0049, 1538-4365. doi:10.1088/0067-0049/190/2/220. URL http://stacks.iop.org/0067-0049/190/i=2/a=220?key=crossref.5356e7dcfc22a545a669868ac94e95de.

E. Huby, P. Baudoz, D. Mawet, and O. Absil. Post-coronagraphic tip-tilt sensing for vortex phase masks: The QACITS technique. *Astronomy & Astrophysics*, 584:A74, December 2015. ISSN 0004-6361, 1432-0746. doi:10.1051/0004-6361/201527102. URL http://www.aanda.org/10.1051/0004-6361/201527102.

Hauke Hussmann, Gaël Choblet, Valéry Lainey, Dennis L. Matson, Christophe Sotin, Gabriel Tobie, and Tim Van Hoolst. Implications of Rotation, Orbital States, Energy Sources, and Heat Transport for Internal Processes in Icy Satellites. *Space Science Reviews*, 153(1-4):317–348, June 2010. ISSN 0038-6308, 1572-9672. doi:10.1007/s11214-010-9636-0. URL http://link.springer.com/10.1007/s11214-010-9636-0.

Charles Jenkins. Optical vortex coronagraphs on ground-based telescopes: Optical vortex coronagraphs. *Monthly Notices of the Royal Astronomical Society*, 384(2):515–524, January 2008. ISSN 00358711, 13652966. doi:10.1111/j.1365-2966.2007.12744.x. URL https://academic.oup.com/mnras/article-lookup/doi/10.1111/j.1365-2966.2007.12744.x.

A. Jolivet, P. Piron, E. Huby, O. Absil, C. Delacroix, D. Mawet, J. Surdej, and S. Habraken. The VORTEX coronagraphic test bench. page 91515P, Montréal,

Quebec, Canada, July 2014. doi:10.1117/12.2055791. URL http://proceedings.spiedigitallibrary.org/proceeding.aspx?doi=10.1117/12.2055791.

Aïssa Jolivet, Gilles Orban de Xivry, Elsa Huby, Pierre Piron, Ernesto Vargas Catalan, Serge Habraken, Jean Surdej, Mikael Karlsson, and Oliver Absil. L- and M-band annular groove phase mask in lab performance assessment on the vortex optical demonstrator for coronagraphic applications. *Journal of Astronomical Telescopes, Instruments, and Systems*, 5(02):1, April 2019. ISSN 2329-4124. doi:10.1117/1.JATIS.5.2.025001. URL https://www.spiedigitallibrary.org/journals/Journal-of-Astronomical-Telescopes-Instruments-and-Systems/volume-5/issue-02/025001/L--and-M-band-annular-groove-phase-mask-in/10.1117/1.JATIS.5.2.025001.full.

Mikael Karlsson and F. Nikolajeff. Diamond micro-optics: microlenses and antireflection structured surfaces for the infrared spectral region. *Optics Express*, 11 (5):502, March 2003. ISSN 1094-4087. doi:10.1364/OE.11.000502. URL https://www.osapublishing.org/oe/abstract.cfm?uri=oe-11-5-502.

N. Jeremy Kasdin, Robert J. Vanderbei, Michael G. Littman, Michael Carr, and David N. Spergel. The shaped pupil coronagraph for planet finding coronagraphy: optimization, sensitivity, and laboratory testing. page 1312, USA, October 2004. doi:10.1117/12.552273. URL http://proceedings.spiedigitallibrary.org/proceeding.aspx?doi=10.1117/12.552273.

Hisao Kikuta, Yasushi Ohira, and Koichi Iwata. Achromatic quarter-wave plates using the dispersion of form birefringence. *Applied Optics*, 36(7):1566, March 1997. ISSN 0003-6935, 1539-4522. doi:10.1364/AO.36.001566. URL https://www.osapublishing.org/abstract.cfm?URI=ao-36-7-1566.

David M. Kipping and Emily Sandford. Observational biases for transiting planets. *Monthly Notices of the Royal Astronomical Society*, 463(2):1323–1331, December 2016. ISSN 0035-8711, 1365-2966. doi:10.1093/mnras/stw1926. URL https://academic.oup.com/mnras/article-lookup/doi/10.1093/mnras/stw1926.

Ravi Kumar Kopparapu, Ramses Ramirez, James F. Kasting, Vincent Eymet, Tyler D. Robinson, Suvrath Mahadevan, Ryan C. Terrien, Shawn Domagal-Goldman, Victoria Meadows, and Rohit Deshpande. HABITABLE ZONES AROUND MAIN-SEQUENCE STARS: NEW ESTIMATES. *The Astrophysical Journal*, 765(2):131, February 2013. ISSN 0004-637X, 1538-4357. doi:10.1088/0004-637X/765/2/131. URL http://stacks.iop.org/0004-637X/765/i=2/a=131?key=crossref.2f4b541791428841b8a64638c66c631c.

David Lafreniere, Christian Marois, Rene Doyon, Daniel Nadeau, and Etienne Artigau. A New Algorithm for Point-Spread Function Subtraction in High-Contrast Imaging: A Demonstration with Angular Differential Imaging. *The Astrophysical Journal*, 660(1):770–780, May 2007. ISSN 0004-637X, 1538-4357. doi:10.1086/513180. URL http://stacks.iop.org/0004-637X/660/i=1/a=770.

Bernard Lyot. The Study of the Solar Corona and Prominences without Eclipses (George Darwin Lecture, delivered by M. Bernard Lyot, Assoc.R.A.S., on 1939 May 12). *Monthly Notices of the Royal Astronomical Society*, 99(8):580–594, June 1939. ISSN 0035-8711, 1365-2966. doi:10.1093/mnras/99.8.580. URL https://academic.oup.com/mnras/article-lookup/doi/10.1093/mnras/99.8.580.

B. Macintosh, J. R. Graham, P. Ingraham, Q. Konopacky, C. Marois, M. Perrin, L. Poyneer, B. Bauman, T. Barman, A. S. Burrows, A. Cardwell, J. Chilcote, R. J. De Rosa, D. Dillon, R. Doyon, J. Dunn, D. Erikson, M. P. Fitzgerald, D. Gavel, S. Goodsell, M. Hartung, P. Hibon, P. Kalas, J. Larkin, J. Maire, F. Marchis, M. S. Marley, J. McBride, M. Millar-Blanchaer, K. Morzinski, A. Norton, B. R. Oppenheimer, D. Palmer, J. Patience, L. Pueyo, F. Rantakyro, N. Sadakuni, L. Saddlemyer, D. Savransky, A. Serio, R. Soummer, A. Sivaramakrishnan, I. Song, S. Thomas, J. K. Wallace, S. Wiktorowicz, and S. Wolff. First light of the Gemini Planet Imager. *Proceedings of the National Academy of Sciences*, 111(35):12661–12666, September 2014. ISSN 0027-8424, 1091-6490. doi:10.1073/pnas.1304215111. URL http://www.pnas.org/cgi/doi/10.1073/pnas.1304215111.

Christian Marois, David Lafreniere, Rene Doyon, Bruce Macintosh, and Daniel Nadeau. Angular Differential Imaging: A Powerful High-Contrast Imaging Technique. *The Astrophysical Journal*, 641(1):556–564, April 2006. ISSN 0004-637X, 1538-4357. doi:10.1086/500401. URL http://stacks.iop.org/0004-637X/641/i=1/a=556.

D. Mawet, P. Riaud, O. Absil, and J. Surdej. Annular Groove Phase Mask Coronagraph. *The Astrophysical Journal*, 633(2):1191–1200, November 2005. ISSN 0004-637X, 1538-4357. doi:10.1086/462409. URL http://stacks.iop.org/0004-637X/633/i=2/a=1191.

Dimitri Mawet. *Subwavelength gratings for extrasolar planetary system imaging and characterization*. PhD thesis, 09 2006.

Dimitri Mawet, Laurent Pueyo, Dwight Moody, John Krist, and Eugene Serabyn. The Vector Vortex Coronagraph: sensitivity to central obscuration, low-order aberrations, chromaticism, and polarization. page 773914, San Diego, California, USA, July 2010. doi:10.1117/12.858240. URL http://proceedings.spiedigitallibrary.org/proceeding.aspx?doi=10.1117/12.858240.

Dimitri Mawet, Naoshi Murakami, Christian Delacroix, Eugene Serabyn, Olivier Absil, Naoshi Baba, Jacques Baudrand, Anthony Boccaletti, Rick Burruss, Russell Chipman, Pontus Forsberg, Serge Habraken, Shoki Hamaguchi, Charles Hanot, Akitoshi Ise, Mikael Karlsson, Brian Kern, John Krist, Andreas Kuhnert, Marie Levine, Kurt Liewer, Stephen McClain, Scott McEldowney, Bertrand Mennesson, Dwight Moody, Hiroshi Murakami, Albert Niessner, Jun Nishikawa, Nada O'Brien, Kazuhiko Oka, Peggy Park, Pierre Piron, Laurent Pueyo, Pierre Riaud, Moritsugu Sakamoto, Motohide Tamura, John Trauger, David Shemo, Jean Surdej, Nelson Tabirian, Wesley Traub, James Wallace, and Kaito Yokochi. Taking the vector vortex coronagraph to the next level for ground- and space-based exoplanet imaging instruments: review of technology developments in the USA, Japan, and Europe. page 815108, San Diego, California, USA, September 2011. doi:10.1117/12.896059. URL http://proceedings.spiedigitallibrary.org/proceeding.aspx?doi=10.1117/12.896059.

Michel Mayor and Didier Queloz. A Jupiter-mass companion to a solar-type star. *Nature*, 378(6555):355–359, November 1995. ISSN 0028-0836, 1476-4687. doi:10.1038/378355a0. URL http://www.nature.com/articles/378355a0.

Julien Milli, David Mouillet, Thierry Fusco, Julien Girard, Elena Masciadri, Eduardo Pena, Jean-Francois Sauvage, Claudia Reyes, Kjetil Dohlen, Jean-Luc Beuzit,

Markus Kasper, Marc Sarazin, and Faustine Cantaloube. Performance of the extreme-AO instrument VLT/SPHERE and dependence on the atmospheric conditions. In *Proceedings of the Adaptive Optics for Extremely Large Telescopes 5*. Instituto de Astrofisica de Canarias (IAC), 2017. doi:10.26698/AO4ELT5.0034. URL http://www.iac.es/congreso/AO4ELT5/pages/proceeding.php?id=34.

M. G. Moharam and T. K. Gaylord. Rigorous coupled-wave analysis of planar-grating diffraction. *Journal of the Optical Society of America*, 71(7):811, jul 1981. doi:10.1364/josa.71.000811. URL https://doi.org/10.1364/josa.71.000811.

Avi Niv, Gabriel Biener, Vladimir Kleiner, and Erez Hasman. Manipulation of the Pancharatnam phase in vectorial vortices. *Optics Express*, 14(10):4208, 2006. ISSN 1094-4087. doi:10.1364/OE.14.004208. URL https://www.osapublishing.org/oe/abstract.cfm?uri=oe-14-10-4208.

Gilles Orban de Xivry, Olivier Absil, Elsa Huby, and Aïssa Jolivet. Post-coronagraphic PSF sharpening with the vortex coronagraph. In *Proceedings of the Adaptive Optics for Extremely Large Telescopes 5*. Instituto de Astrofisica de Canarias (IAC), 2017. doi:10.26698/AO4ELT5.0066. URL http://www.iac.es/congreso/AO4ELT5/pages/proceeding.php?id=66.

S. Pancharatnam. Generalized theory of interference, and its applications: Part I. Coherent pencils. *Proceedings of the Indian Academy of Sciences - Section A*, 44(5): 247–262, November 1956. ISSN 0370-0089. doi:10.1007/BF03046050. URL http://link.springer.com/10.1007/BF03046050.

Erik A. Petigura, Andrew W. Howard, and Geoffrey W. Marcy. Prevalence of Earth-size planets orbiting Sun-like stars. *Proceedings of the National Academy of Sciences*, 110(48):19273–19278, November 2013. ISSN 0027-8424, 1091-6490. doi:10.1073/pnas.1319909110. URL https://www.pnas.org/content/110/48/19273.

René Racine, Gordon A. H. Walker, Daniel Nadeau, René Doyon, and Christian Marois. Speckle Noise and the Detection of Faint Companions. *Publications of the Astronomical Society of the Pacific*, 111(759):587–594, May 1999. ISSN 0004-6280, 1538-3873. doi:10.1086/316367. URL http://iopscience.iop.org/article/10.1086/316367.

P. Riaud, A. Boccaletti, D. Rouan, F. Lemarquis, and A. Labeyrie. The Four-Quadrant Phase-Mask Coronagraph. II. Simulations. *Publications of the Astronomical Society of the Pacific*, 113(787):1145–1154, September 2001. ISSN 0004-6280, 1538-3873. doi:10.1086/323112. URL http://iopscience.iop.org/article/10.1086/323112.

F. Roddier and C. Roddier. Stellar Coronograph with Phase Mask. *Publications of the Astronomical Society of the Pacific*, 109:815, July 1997. ISSN 0004-6280, 1538-3873. doi:10.1086/133949. URL http://iopscience.iop.org/article/10.1086/133949.

D. Rouan, P. Riaud, A. Boccaletti, Y. Clénet, and A. Labeyrie. The Four-Quadrant Phase-Mask Coronagraph. I. Principle. *Publications of the Astronomical Society of the Pacific*, 112(777):1479–1486, November 2000. ISSN 0004-6280, 1538-3873. doi:10.1086/317707. URL http://iopscience.iop.org/article/10.1086/317707.

Daniel Rouan, Jacques Baudrand, Anthony Boccaletti, Pierre Baudoz, Dimitri Mawet, and Pierre Riaud. The Four Quadrant Phase Mask Coronagraph and its avatars. *Comptes Rendus Physique*, 8(3-4):298–311, April 2007. ISSN 16310705. doi:10.1016/j.crhy.2007.05.004. URL https://linkinghub.elsevier.com/retrieve/pii/S1631070507000850.

G Rousset, J C. Fontanella, Pierre Kern, P Gigan, and Francois Rigaut. First diffraction-limited astronomical images with adaptive optics. *Astronomy and Astrophysics*, 230:L29–L32, March 1990.

Garreth Ruane, Neil Zimmerman, Ewan Douglas, Johan Mazoyer, A.J. Eldorado Riggs, Brunella Carlomagno, Elsa Huby, Kevin Fogarty, Emiel Por, Olivier Absil, Pierre Baudoz, Raphaël Galicher, Mathilde Beaulieu, Eric J. Cady, Alexis Carlotti, David Doelman, Olivier Guyon, Sebastiaan Haffert, Jeffrey B. Jewell, Nemanja Jovanovic, Christoph Keller, Matthew A. Kenworthy, Justin Knight, Jonas Kuhn, Kelsey Miller, Mamadou N'Diaye, Laurent Pueyo, Dan Sirbu, Frans Snik, James K. Wallace, Michael Wilby, and Marie Ygouf. Review of high-contrast imaging systems for current and future ground- and space-based telescopes I: coronagraph design methods and optical performance metrics. In Howard A. MacEwen, Makenzie Lystrup, Giovanni G. Fazio, Natalie Batalha, Edward C. Tong, and Nicholas Siegler, editors, *Space Telescopes and Instrumentation 2018: Optical, Infrared, and Millimeter Wave*, page 98, Austin, United States, August 2018. SPIE. ISBN 9781510619494 9781510619500. doi:10.1117/12.2312948. URL https://www.spiedigitallibrary.org/conference-proceedings-of-spie/10698/2312948/Review-of-high-contrast-imaging-systems-for-current-and-future/10.1117/12.2312948.full.

Ananya Sahoo, Olivier Guyon, Christophe S. Clergeon, Nour Skaf, Yosuke Minowa, Julien Lozi, Nemanja Jovanovic, and Frantz Martinache. Subaru Coronagraphic Extreme-AO (SCExAO) wavefront control: current status and ongoing developments. In Dirk Schmidt, Laura Schreiber, and Laird M. Close, editors, *Adaptive Optics Systems VI*, page 187, Austin, United States, July 2018. SPIE. ISBN 9781510619593 9781510619609. doi:10.1117/12.2314333. URL https://www.spiedigitallibrary.org/conference-proceedings-of-spie/10703/2314333/Subaru-Coronagraphic-Extreme-AO-SCExAO-wavefront-control--current-status/10.1117/12.2314333.full.

Edward W. Schwieterman, Nancy Y. Kiang, Mary N. Parenteau, Chester E. Harman, Shiladitya DasSarma, Theresa M. Fisher, Giada N. Arney, Hilairy E. Hartnett, Christopher T. Reinhard, Stephanie L. Olson, Victoria S. Meadows, Charles S. Cockell, Sara I. Walker, John Lee Grenfell, Siddharth Hegde, Sarah Rugheimer, Renyu Hu, and Timothy W. Lyons. Exoplanet Biosignatures: A Review of Remotely Detectable Signs of Life. *Astrobiology*, 18(6):663–708, June 2018. ISSN 1531-1074, 1557-8070. doi:10.1089/ast.2017.1729. URL http://www.liebertpub.com/doi/10.1089/ast.2017.1729.

E. Serabyn, D. Mawet, J. K. Wallace, K. Liewer, J. Trauger, D. Moody, and B. Kern. Recent progress in vector vortex coronagraphy. page 81460L, San Diego, California, USA, September 2011. doi:10.1117/12.895267. URL http://proceedings.spiedigitallibrary.org/proceeding.aspx?doi=10.1117/12.895267.

D. K. Sing, J.-M. Désert, A. Lecavelier des Etangs, G. E. Ballester, A. Vidal-Madjar, V. Parmentier, G. Hebrard, and G. W. Henry. Transit spectrophotometry of the

exoplanet HD 189733b: I. Searching for water but finding haze with HST NICMOS. *Astronomy & Astrophysics*, 505(2):891–899, October 2009. ISSN 0004-6361, 1432-0746. doi:10.1051/0004-6361/200912776. URL http://www.aanda.org/10.1051/0004-6361/200912776.

W. Hayden Smith. Spectral differential imaging detection of planets about nearby stars. *Publications of the Astronomical Society of the Pacific*, 99:1344, December 1987. ISSN 0004-6280, 1538-3873. doi:10.1086/132124. URL http://iopscience.iop.org/article/10.1086/132124.

Frank Sohl, Mathieu Choukroun, Jeffrey Kargel, Jun Kimura, Robert Pappalardo, Steve Vance, and Mikhail Zolotov. Subsurface Water Oceans on Icy Satellites: Chemical Composition and Exchange Processes. *Space Science Reviews*, 153(1-4): 485–510, June 2010. ISSN 0038-6308, 1572-9672. doi:10.1007/s11214-010-9646-y. URL http://link.springer.com/10.1007/s11214-010-9646-y.

R. Soummer, C. Aime, and P. E. Falloon. Stellar coronagraphy with prolate apodized circular apertures. *Astronomy & Astrophysics*, 397(3):1161–1172, January 2003. ISSN 0004-6361, 1432-0746. doi:10.1051/0004-6361:20021573. URL http://www.aanda.org/10.1051/0004-6361:20021573.

Grover A Swartzlander Jr. The optical vortex coronagraph. *Journal of Optics A: Pure and Applied Optics*, 11(9):094022, September 2009. ISSN 1464-4258, 1741-3567. doi:10.1088/1464-4258/11/9/094022. URL http://stacks.iop.org/1464-4258/11/i=9/a=094022?key=crossref.4c22e972ef1a872090fcbd03e4607d10.

The SPECULOOS and TRAPPIST teams, Artem Burdanov, Laetitia Delrez, Michaël Gillon, and Emmanuël Jehin. SPECULOOS Exoplanet Search and Its Prototype on TRAPPIST. In Hans J. Deeg and Juan Antonio Belmonte, editors, *Handbook of Exoplanets*, pages 1007–1023. Springer International Publishing, Cham, 2018. ISBN 9783319553320 9783319553337. doi:10.1007/978-3-319-55333-7_130. URL http://link.springer.com/10.1007/978-3-319-55333-7_130.

Diana Valencia, Dimitar D. Sasselov, and Richard J. O'Connell. Radius and Structure Models of the First Super-Earth Planet. *The Astrophysical Journal*, 656(1):545–551, February 2007. ISSN 0004-637X, 1538-4357. doi:10.1086/509800. URL http://stacks.iop.org/0004-637X/656/i=1/a=545.

Andrew Vanderburg, Peter Plavchan, John Asher Johnson, David R. Ciardi, Jonathan Swift, and Stephen R. Kane. Radial velocity planet detection biases at the stellar rotational period. *Monthly Notices of the Royal Astronomical Society*, 459 (4):3565–3573, July 2016. ISSN 0035-8711, 1365-2966. doi:10.1093/mnras/stw863. URL https://academic.oup.com/mnras/article-lookup/doi/10.1093/mnras/stw863.

E. Vargas Catalán, E. Huby, P. Forsberg, A. Jolivet, P. Baudoz, B. Carlomagno, C. Delacroix, S. Habraken, D. Mawet, J. Surdej, O. Absil, and M. Karlsson. Optimizing the subwavelength grating of *L* -band annular groove phase masks for high coronagraphic performance. *Astronomy & Astrophysics*, 595:A127, November 2016. ISSN 0004-6361, 1432-0746. doi:10.1051/0004-6361/201628739. URL http://www.aanda.org/10.1051/0004-6361/201628739.

Joshua N. Winn. Transits and Occultations. *arXiv:1001.2010 [astro-ph]*, January 2010. URL http://arxiv.org/abs/1001.2010. arXiv: 1001.2010.

A. Wolszczan and D. A. Frail. A planetary system around the millisecond pulsar PSR1257 + 12. *Nature*, 355(6356):145–147, January 1992. ISSN 1476-4687. doi:10.1038/355145a0. URL https://www.nature.com/articles/355145a0.

ACKNOWLEDGEMENTS

Firstly, I would like to thank my advisors Olivier Absil, Serge Habraken and Jean Surdej, I will always be grateful to you for giving me the amazing opportunity to complete this Ph.D thesis. It has been an incredible experience and a pleasure to learn and work by your side.

Thank you Olivier for your support and guidance during all these years, you have always found time for me and perfectly managed this project.

Thank you Serge for having me in Hololab! Your extensive knowledge and experience helped me a lot. You always made sure I worked in the best conditions at the University (and at the CSL).

I would like to express my gratitude to Jean, thank you for your help and constant encouragements during this thesis.

I also thank the members of the jury for accepting to evaluate my work: Denis Grodent, Olivier Absil, Serge Habraken, Mikael Karlsson, Lucas Labadie, Dimitri Mawet, Gilles Orban de Xivry and Jean Surdej.

I want to thank all the Uppsala team, Mikael, Ernesto and Pontus, I really admire your work. Thank you for always warmly welcoming us in Sweden! Thanks to Cedric Lenaerts for the help in CSL. Thanks to everyone involved at the Observatoire de Meudon for offering us the possibility to test our AGPMs.

I would like to thank Sylvia and Angela for being always available and caring, you made my life so much easier with all the administrative matters.

I want to thank all the (past and present) Hololab members, Bernard, Georges, Marc and Pierre .Thank you for creating a friendly work environment and for the refreshing lunch breaks playing cards!

Thank you Elsa, I am really happy that I have shared an office with you for a few years, the badminton sessions after work were a lot of fun! Unfortunately all of our plants didn't survive much longer after you left (probably my fault).

Thank you to all my colleagues, Brunella, Carlos, Maddalena, Bikram, Gilles, Gary and Christian. Thank you for being part of my journey in Liège, thank you for the amazing memories in and outside the lab.

Thanks to all the friends I met here in Liège. Arash, Hamed, Hamid, Eri, Ramona and many others, I am so happy I met you. Thank you Alexandra for being my friend and much more. So many wonderful experiences I will never forget.

Last but not least, I want to thank my parents and sisters for always supporting me, I know you will always be there for me.

The research leading to these results has received funding from the European Research Council Under the European Union's Seventh Framework Program (ERC Grant Agreement n. 337569) and from the French Community of Belgium through an ARC grant for Concerted Research Action.